Assembly mechanisms of CVD graphene investigated by scanning tunnelling microscopy

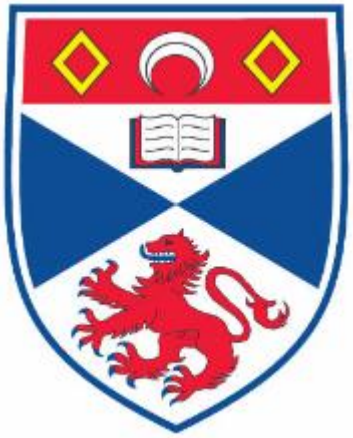

A thesis submitted for the degree of PhD

By

Catherine Bromley

Supervised by Dr. Renald Schaub

School of Chemistry
University of St. Andrews
August 2014

Declaration

1. Candidate's declarations:

I, Catherine Bromley, hereby certify that this thesis, which is approximately 35,000 words in length, has been written by me, and that it is the record of work carried out by me, or principally by myself in collaboration with others as acknowledged, and that it has not been submitted in any previous application for a higher degree.

I was admitted as a research student in September, 2010 and as a candidate for the degree of Doctor of Philosophy in September, 2010; the higher study for which this is a record was carried out in the University of St Andrews between 2010 and 2014.

Date …….. Signature of candidate ……

2. Supervisor's declaration:

I hereby certify that the candidate has fulfilled the conditions of the Resolution and Regulations appropriate for the degree of Doctor of Philosophy in the University of St Andrews and that the candidate is qualified to submit this thesis in application for that degree.

Date ……. Signature of supervisor …….

3. Permission for publication:

In submitting this thesis to the University of St Andrews I understand that I am giving permission for it to be made available for use in accordance with the regulations of the University Library for the time being in force, subject to any copyright vested in the work not being affected thereby. I also understand that the title and the abstract will be published, and that a copy of the work may be made and supplied to any bona fide library or research worker, that my thesis will be electronically accessible for personal or

research use unless exempt by award of an embargo as requested below, and that the library has the right to migrate my thesis into new electronic forms as required to ensure continued access to the thesis. I have obtained any third-party copyright permissions that may be required in order to allow such access and migration, or have requested the appropriate embargo below.

The following is an agreed request by candidate and supervisor regarding the publication of this thesis: embargo on both [all or part of] printed copy and electronic copy for the same fixed period of 2 years on the following ground: publication would preclude future publication.

Date …….. Signature of candidate ……

Signature of supervisor ……..

Abstract

In this thesis, the growth mechanism of graphene on a transition metal support is determined, and the epitaxial relationship investigated. The main technique used is low-temperature scanning tunnelling microscopy (STM), which is introduced in Chapter 2.

Epitaxial graphene synthesised on copper (foil and (110) single crystal), from the dehydrogenation of ethene, is investigated by STM and low energy electron diffraction (LEED) in Chapter 4. Despite the weak epitaxial relationship that exists, LEED uncovers two preferred orientations of the graphene over the copper. Further investigation reveals restructuring of the copper foil from a predominantly (100) orientation to (n10) facets. Structural feedback is found to exist, with the graphene growth inducing and stabilising faceting of the copper surface, and the facets in-turn playing an important role in the graphene growth mechanism. The preferred orientations, which are also seen on the single crystal, are most likely determined during nucleation and early stage growth, where it is expected that the interaction is stronger.

The growth mechanism for the formation of graphene from ethene is studied on a Rh(111) surface in Chapter 5. This is found to consist of two regimes, with the first revolving around the transformation from aliphatic hydrocarbons to aromatic intermediates. This occurs through the decomposition and condensation of ethene, resulting in the formation of one-dimensional polyaromatic hydrocarbons (1D-PAHs). The second regime is characterised by the transition from these 1D-PAHs, to the 2D graphene. The previously produced 1D-PAHs, decompose to form size-selective carbon clusters, with these clusters being the precursors to graphene condensation.

In Chapter 6, the conclusions of Chapter 5 are built upon through investigation into the effect of different hydrocarbon feedstocks on the graphene growth pathway. Benzene, tetracene, and perylene are the feedstocks examined. In all cases 1D-PAHs are formed, which decompose to clusters that subsequently condense to form graphene.

Acknowledgements

Firstly, I would like to thank my supervisor Dr. Renald Schaub for introducing me to the fascinating world of atoms and molecules on surfaces. His support, motivation, and enthusiasm helped me throughout my PhD study. He also taught me valuable skills for debugging and solving problems independently when managing the UHV and STM facilities.

Next, I would like to thank Dr. Marco Caffio for his crash-course in using the STM, which he provided during the first month of my studies. I am also grateful to Prof. Neville Richardson for use of his HREELs and to Dr. Federico Grillo for his assistance in using it. Thanks also go to my fellow members of the Schaub group; Grant Simpson, Michael-John Treanor, and José Garrido Torres for their support and stimulating discussions. I would also like to thank the rest of the surface science group, especially Dr. Steve Francis, for his technical help and useful discussions.

Many thanks must also go to the many people I have collaborated with during the course of my PhD. I would like to thank the researchers at the University of Warwick for including me in their fascinating work with graphene on copper, particularly Dr. Neil Wilson, Dr. Gavin Bell, and Dr. Giovanni Costantini. Thanks must also go to the group of Prof. Ulrich Heiz at Technische Universität München, especially Dr. Friedrich Esch and Michael König. Their fascinating videos acquired using their variable temperature STM helped significantly in understanding my own observations. I am also grateful to Prof. Uzi Landman and Dr. Bowkon Yoon, at Georgia Institute of Technology, for their DFT calculations.

My final, and most loving thanks, go to my family and my partner Nick McVie, for all their love and support during the course of my studies.

Contents

Declaration i

1. Candidate's declarations: i

2. Supervisor's declaration: i

3. Permission for publication: i

Abstract iii

Acknowledgements iv

Contents v

Chapter 1: Introduction 1

1.1 Graphene 1

1.2 Properties of Graphene 2

1.3 Methods of graphene production 4

1.4 Graphene on a transition metal surface 6

1.5 Organisation and focus of this thesis 8

References 9

Chapter 2: Techniques 11

2.1 Surface science 11

2.2 Scanning tunnelling Microscopy (STM) 12

2.3 Low energy electron diffraction (LEED) 15

2.4 High resolution electron energy loss spectroscopy (HREELS) 18

References 19

Chapter 3: Experimental 20

3.1 Instruments and methodology 20

3.1.1 The UHV system 20

3.1.2 The CreaTec low-temperature STM 22

3.1.3 Tip preparation 23
3.1.4 The HREELS system 25
3.2 The Rh(111) crystal 25
3.2.1 Preparation of the Rh(111) surface 25
3.2.2 General features of the Rh(111) surface 27
3.3 The Cu(110) crystal 29
3.3.1 Preparation of the Cu(110) surface 29
3.3.2 General features of the Cu(110) surface 29
References 29
Chapter 4: Growth and morphology of graphene on Cu(110) 31
4.1 Introduction 31
4.1.1 Moiré patterns 33
4.1.2 Aims 41
4.2 Graphene preparation 42
4.3 The epitaxial relationship between graphene and copper 46
4.3.1 Graphene on copper foil 46
4.3.2 Graphene on Cu(110) 48
4.4 Conclusion 55
References 57
Chapter 5: Growth mechanism of graphene from ethene on Rh(111) 59
5.1 Introduction 59
5.1.1 Motivations 59
5.1.2 Previous work from literature 60
5.2 Methodology 61
5.3 Results 62
5.3.1 Overview 62

5.3.2 Ethylidyne 63
5.3.3 One-dimensional polyaromatic hydrocarbons 65
5.3.4 Formation of 1D-PAHs 70
5.3.5 Kinking of the 1D-PAHs 74
5.3.6 $7C_6$ formation 77
5.4 Discussion 83
5.5 Conclusion 87
References 88
Chapter 6: Growth mechanism of graphene from different feedstocks on Rh(111) 90
6.1 Introduction 90
6.1.1 Previous work from literature 91
6.2 Methodology 93
6.3 Results 93
6.3.1 Benzene 93
6.3.2 Tetracene 99
6.3.3 Perylene 105
6.4 Discussion 107
6.5 Conclusion 110
References 112
Chapter 7: Conclusion 113
References 116
List of publications 117
Directly related to current thesis 117
Other publications 118

Chapter 1: Introduction

1.1 Graphene

Graphene is a one atom thick sheet of sp^2 bonded carbon atoms arranged in a honeycomb crystal lattice. The term graphene was first used in 1987 when Mouras used it to describe the single sheets of graphite that make up graphite intercalation compounds.[1] The concept, however, had been around since the late 1940s when Wallace published his theoretical studies on graphite, where the band structure of single layer graphite was discussed as a simplified version of bulk graphite.[2] Yet, the interest in graphene, had been minimal before the early 2000s, as free standing graphene was thought of as a theoretical material, and that a 2D material could not exist. In 2004 Geim and Novoselov proved this wrong when they managed to isolate a single sheet from graphite using micromechanical cleavage[3], and the interest in this 2D material exploded.

The reason it was believed that a 2D material such as graphene could not exist is due to the work of Peierls and Landau.[4] [5] Their theories show that 2D materials should not be able to exist without being destroyed by thermal fluctuations, which would cause the crystal to melt. Indeed, in the past when scientists tried to create atomically thin films, they were unstable and tended to break up or decompose.[6] [7] In hindsight, graphene and other 2D materials which have been produced do not necessarily disprove these theories as their formation is stabilised by the 3D materials they are grown on or are extracted from. Further to this, the graphene is stabilised by a gentle rippling in the third dimension.[8] This gentle rippling increases elastic energy while suppressing thermal vibrations. This minimises the total free energy above a certain temperature.[9]

The 2D structure of graphene is a honeycomb lattice containing two atoms per unit cell, which belong to two sublattices A and B. As shown in the ball and stick model in figure 1.1a, each carbon atom from sublattice A is surrounded by three carbon atoms from sublattice B, and vice versa. The distance between two carbon atoms in the lattice is 1.42 Å, which corresponds to a conjugated C-C bond. The simple hexagonal structure of graphene can be thought of as the building block for many of carbon's other allotropes as shown in figure 1.1b. With the addition of pentagons, graphene can be wrapped up to

give fullerenes, the rolling of graphene into cylinders gives carbon nanotubes, and the stacking of graphene gives graphite.

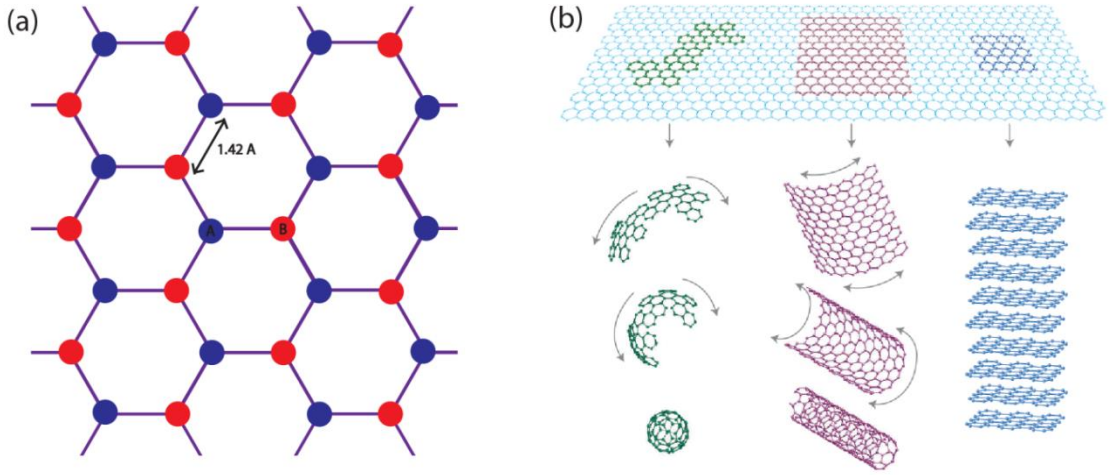

Figure 1.1

(a) shows a ball and stick model of graphene with the blue balls representing the carbon atoms of sublattice A and the red balls the carbon atoms of sublattice B. (b) is a schematic showing how graphene is a template for other allotropes of carbon. From left to right: fullerenes, nanotubes, and graphite. Taken from reference [10].

1.2 Properties of Graphene

In 2010 Geim and Novoselov won the Nobel prize "for groundbreaking experiments regarding the two-dimensional material graphene".[11] These groundbreaking experiments revealed many of the fascinating properties of graphene that make it so interesting. Being one atom thick, graphene is incredibly thin and transparent, and yet is incredibly strong with the intrinsic strength of pristine graphene being 42 $N \cdot m^{-1}$.[12] This is about six times stronger than steel, and the strongest material ever tested, making it the new bench mark for strength.

Perhaps the most interesting of graphene's properties are its electronic ones. Graphene is a ballistic conductor of electricity which arises from the fact that graphene is a semimetal. A semimetal has a small overlap between its conduction and valance bands, meaning there is no band gap so no energy is required to transfer electrons to the conduction band, which is required for a material to pass a current. No energy is required due to the bonding present in graphene. The carbon atoms in the hexagonal lattice of graphene are sp^2 hybridised. The 2s orbital and two of the three 2p orbitals (the ones

which lie along the plane of graphene) form σ bonds between the carbon atom and its neighbours. Three of the four valence electrons are involved in this sp^2 bonding. The fourth electron is in the remaining 2p orbital, which lies perpendicular to the graphene. This 2p orbital overlaps with the 2p orbital on the adjacent C atoms to form π (valence) and π* (conduction) bands. These electrons can flow freely across the whole of graphene through the π network with almost no scattering. Huge electron mobility values have been reported for graphene, even in the region of 200,000 $cm^2V^{-1}s^{-1}$ for suspended graphene.[13]

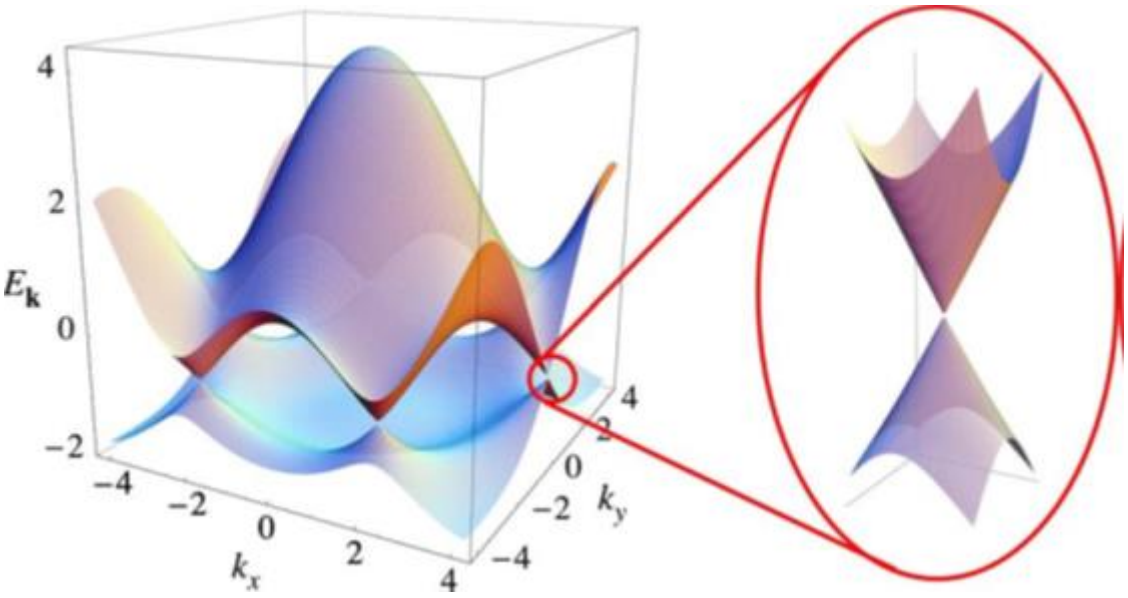

Figure 1.2

The electronic structure of graphene which has been calculated using the tight-binding approximation. The zoom-in shows the conduction and valance bands touching at the Dirac point. Taken from reference [14].

As mentioned previously, graphene is made up of two equivalent sublattices, A and B. The quantum mechanical hopping which occurs between these two sublattices results in the unusual electronic structure which is shown in figure 1.2, and was calculated using the tight binding method. The occurrence of this quantum mechanical hopping results in the formation of two energy bands, which are conical about the Fermi energy with the vertices touching exactly at the Fermi level.[15] It is at the edge of the Brillouin zone that these vertices touch near the Dirac points K and K'.[16] A linear dispersion of the electron energy exists at these Dirac points. This is very different to that of metals and

semiconductors, which is approximately parabolic. The electrons' linear dispersion relationship can be described by the equation $E=\hbar k v_F$, where the Fermi velocity v_F is a constant of about 10^6 $m \cdot s^{-1}$, which is equivalent to a 300^{th} of the speed of light (c). Since the physics of quantum electrodynamics for massless fermions can be described by the equation $E=\hbar kc$, many of the unusual properties of quantum electrodynamics can be seen in graphene but at lower speeds (300 times lower). This has allowed physical phenomena such as the Klein paradox[17] and the half-integer quantum Hall effect[18] to be observed.

As previously mentioned, pure, monolayer graphene has no band gap, but the band gap can be tuned by doping, or by the stacking of two graphene sheets to give bilayer graphene.[14] With bilayer graphene, the application of an electric field creates a band gap by breaking the inversion symmetry. This method was demonstrated by a group of physicists at University of California at Berkeley to create a tuneable band gap up to 250 meV.[19] Another way to break the inversion symmetry, and open up a band gap, is to deposit molecules on the surface of just one of the graphene sheets.[20] [21] Doping can also be used to tune the band gap in monolayer graphene, and this is done by replacing some of the carbon atoms in the lattice with other elements such as nitrogen[22] [23] or boron.[24] This opens up the band gap through the formation of p- or n-type doping.

Graphene also has a high thermal conductivity as phonons, the particles which conduct heat, can travel ballistically across its surface. The thermal conductivity of graphene has recently been measured as about 5000 $W \cdot m^{-1}K^{-1}$ at near-room temperature.[25]

1.3 Methods of graphene production

There are many methods of graphene production with differences in quality, ease of production, and scalability. The method that was used to first isolate graphene, micromechanical cleavage, is also known as the scotch tape method. This is a very crude method which involves putting a graphite flake onto plastic adhesive tape, folding the tape over the graphite flake, pulling the tape apart which cleaves the flake in two, and repeating until just a single layer is left. Graphene produced by this method is very high quality and is widely used in research. It is, however, unlikely to find any uses

commercially as only small flakes (in the order of a micron) can be produced and not on a large scale.

A method by which graphene flakes can be produced on a large scale, is by liquid phase exfoliation of graphite. This method involves exposing graphite to a solvent which can efficiently disperse the graphene such as N-methylpyrrolidone (NMP) or dimethyl sulfoxide (DMSO).[26] Sonication is used to aid the splitting of the graphite into individual platelets, with a prolonged treatment and the use of centrifugation giving a suspension which contains mainly monolayer flakes. A similar process using graphite oxide[27] [28] [29] is also possible with the addition of a reduction step at the end to remove the oxygen. Because of the already scalable nature of liquid phase exfoliation, it is expected that within a few years this method will be used commercially for applications such as conductive paints/inks and barrier coatings. [30]

Another method is the epitaxial growth of graphene directly onto a surface, which can produce large sheets of graphene. But the graphene flakes are not as high quality as those produced by micromechanical cleavage, as the sheet is made up of lots of small grains joined together. This method can be split into two categories: the heating of SiC; and the growth on transition metal surfaces. The first method, heating of SiC, involves the heating of SiC crystal to high temperatures to desorb silicon from the surface and leave a layer of carbon, in the form of graphene. This has the advantage of being produced directly onto an insulating surface. This is required for many applications, but the thickness of the carbon layer can be difficult to control, and often results in few layer graphene, rather than monolayer.[31]

Graphitic layers on metal surfaces were investigated as far back as the 1970s,[32] [33] [34] but since the isolation of graphene this has become an extensively studied area. Graphene can be grown on a metal surface by segregation of carbon from the bulk, or by the more widely used method of chemical vapour deposition (CVD) of small hydrocarbons. An advantage of this method is that the growth of the graphene is self-limiting, as the metal surface, which catalyses the dehydrogenation of the hydrocarbons, becomes blocked by the graphene, preventing multilayer growth. The main drawback of this method is that the graphene grown by this method would require transfer from the

metal to an insulating substrate for many applications. This increases the number of steps in the process, but it has been shown to be possible to transfer large sheets of graphene from a copper foil to an insulating support.[35]

Other methods of producing graphene include: splitting of carbon nanotubes;[36] pyrolysis of sodium ethoxide;[37] and reduction of carbon dioxide.[38]

1.4 Graphene on a transition metal surface

Graphene on a transition metal surface is different to freestanding graphene, due to the chemical interactions at the interface. The chemical interactions between the graphitic π/π^* and the metal d bands can alter the electronic and physical structure of graphene. For most commercial applications, the graphene would be transferred from the metal substrate to an insulating surface, but understanding the epitaxial relationship that exists between graphene and the metal it is grown on is still of interest for a number of reasons. Firstly, in many graphene based electronic devices, a metal-graphene interface would exist due to contact to metal electrodes.[39] This could have a strong influence on the performance of the device, so a comprehensive understanding is important. Secondly, it could be used as a model for coke formation on metal surfaces. Many of the transition metals which graphene is grown on are used in catalysis. Over time these catalysts can become deactivated, due to carbon deposits which can take the form of graphene.[40] A greater understanding of the interfacial interactions may help find ways to prevent coking. Another reason to study the epitaxial relationship is that it could be used to help understand how graphene grows on the transition metal, which could improve the growth method and quality of the graphene. Further to this it could improve the methods used to transfer the graphene to an insulating substrate for the commercial applications.

Graphene is most often grown on hexagonal metal surfaces as these have the same symmetry as the graphene. For these hexagonal surfaces, there are two types of possible superstructure. The type of superstructure present depends on the lattice mismatch which exists between the graphene and the metal surface. If there is just a small mismatch, around 1%, then a simple 1×1 relationship exists. This is typically seen for 3d metals like Nickel, as is shown in the STM image in figure 1.3a, with the graphene

appearing flat and uncorrugated. The second type occurs when a larger mismatch is present, around 10%, which typically occurs for 4d and 5d metals. Some STM images of this type of superstructure are shown in figure 1.3b. They have a periodicity of about 3 nm and are rich in contrast. The rich contrast is due to the graphene rings being positioned differently over the surface metal atoms, with a mixture of attractive and repulsive chemical interactions resulting in a corrugated effect.

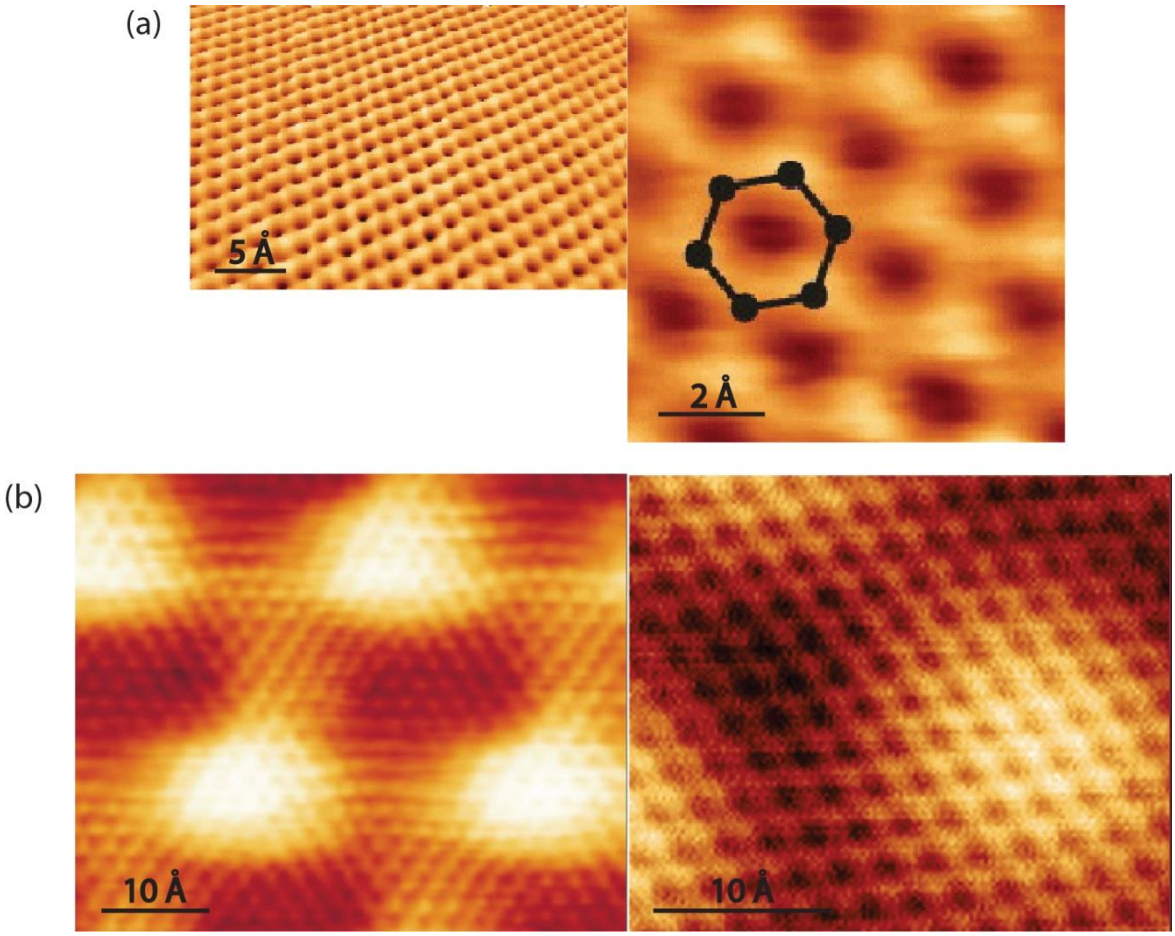

Figure 1.3

STM images of graphene grown epitaxially on transition metal surfaces. (a) shows two images of graphene on Ni(111) where the graphene appears flat. Taken from reference [41] (b) shows images of graphene on Ru(0001) (left) and Ir(111) (right) where the graphene is corrugated which can be seen from the rich contrast. Taken from references [42] and [43] respectively.

The majority of the effect on electronic structure comes not from the rippling, but how strongly the metal interacts with the graphene as a whole.[44] A metal surface which reacts strongly with the graphene such as Ni(111), has a significant hybridisation of the graphene π and nickel 3d states which results in the destruction of the Dirac cones.[45] [46]

Conversely, a weakly interacting interface, such as that of graphene and Cu(111), has little hybridisation and the Dirac cones remain in the electronic structure.[46] Understanding the strength of the interaction for different metal surfaces is important. For instance, this could obviously have a huge effect on metal contacts in graphene based electronic devices, with some metals having a large negative effect on the electronic properties.

1.5 Organisation and focus of this thesis

The organisation of the work presented in this thesis is as follows. Chapter 2 deals with the techniques used in the study. The main technique used and discussed is scanning tunnelling microscopy (STM). But discussions of the other techniques used, low energy electron diffraction (LEED) and high resolution electron energy loss spectroscopy (HREELS), will also be presented. The discussions will include a background on the history and development of the techniques, as well as the principles behind how they work. Chapter 3 describes the experimental set up of the UHV system and explains how the STM tips are prepared and the metal crystals are cleaned.

This thesis focuses on the growth mechanism of graphene on a transition metal surface, and the epitaxial relationship that exists. Graphene on a copper surface is the focus of Chapter 4. Copper is an important metal in the CVD growth of graphene. The reasons for this will be discussed and the epitaxial relationship between graphene and the copper will be explored. Investigating the epitaxial relationship will provide useful information for, among other things, the removal of graphene from a transition metal surface, and the effect of metal contacts on the graphene in electronic applications.

The growth mechanism of graphene is the focus of Chapters 5 and 6. Understanding the growth mechanism is important as it could help improve graphene growth techniques. Graphene on a transition metal can also be used as a model for catalyst coking, so an understanding of the formation could be used to prevent this. Chapter 5 will present the growth mechanism of graphene from ethene on Rh(111), and Chapter 6 will then expand on this, by detailing the growth of graphene from a variety of hydrocarbon sources. It is expected that the mechanism will be similar on different transition metals, so despite

rhodium not being a usual choice for graphene growth, it should still be relevant. From the perspective of catalyst coking, rhodium is more relevant. In 2012, over 80% of world production of rhodium was used in catalytic converters.[47] It is also used in industrial processes such as the Monsanto process and the steam reforming of natural gas. Over time, the rhodium catalyst becomes deactivated by the build-up of carbon deposits, so an insight into this process would be useful. Finally, Chapter 7 will present the concluding remarks.

References

[1] S. Mouras, A. Hamwi, D. Djurado and J. C. Cousseins, *Revue de chimie minérale* **1987**, *24*, 572-582.
[2] P. R. Wallace, *Physical Review* **1947**, *71*, 622-634.
[3] K. S. Novoselov, A. K. Geim, S. V. Morozov, D. Jiang, Y. Zhang, S. V. Dubonos, I. V. Grigorieva and A. A. Firsov, *Science* **2004**, *306*, 666-669.
[4] R. Pierels, *Annales de l'institut Henri Poincaré* **1935**, *5*, 177-222.
[5] L. D. Landau, *Physikalische Zeitschrift der Sowjetunion* **1937**, *11*, 26-35.
[6] J. A. Venables, G. D. T. Spiller and M. Hanbucken, *Reports on Progress in Physics* **1984**, *47*, 399.
[7] J. W. Evans, P. A. Thiel and M. C. Bartelt, *Surface Science Reports* **2006**, *61*, 1-128.
[8] J. C. Meyer, A. K. Geim, M. I. Katsnelson, K. S. Novoselov, T. J. Booth and S. Roth, *Nature* **2007**, *446*, 60-63.
[9] D. R. Nelson, T. Piran and S. Weinberg, *Statistical Mechanics of Membranes and Surfaces*, World Scientific, Singapore, **2004**.
[10] A. K. Geim and K. Novoselov, *Nature materials* **2007**, *6*, 183-191.
[11] Nobelprize.org in *The Nobel Prize in Physics 2010*, *Vol. 2014* Nobel Media AB 2013, **2013**.
[12] C. Lee, X. Wei, J. W. Kysar and J. Hone, *Science* **2008**, *321*, 385-388.
[13] K. I. Bolotin, K. J. Sikes, Z. Jiang, M. Klima, G. Fudenberg, J. Hone, P. Kim and H. L. Stormer, *Solid State Communications* **2008**, *146*, 351-355.
[14] A. H. Castro Neto, F. Guinea, N. M. R. Peres, K. S. Novoselov and A. K. Geim, *Reviews of Modern Physics* **2009**, *81*, 109.
[15] J. C. Slonczewski and P. R. Weiss, *Physical Review* **1958**, *109*, 272-279.
[16] K. S. Novoselov, S. V. Morozov, T. M. G. Mohinddin, L. A. Ponomarenko, D. C. Elias, R. Yang, I. I. Barbolina, P. Blake, T. J. Booth, D. Jiang, J. Giesbers, E. W. Hill and A. K. Geim, *Physica Status Solidi B-Basic Solid State Physics* **2007**, *244*, 4106-4111.
[17] M. I. Katsnelson, K. S. Novoselov and A. K. Geim, *Nature Physics* **2006**, *2*, 620-625.
[18] K. S. Novoselov, A. K. Geim, S. V. Morozov, D. Jiang, M. I. Katsnelson, I. V. Grigorieva, S. V. Dubonos and A. A. Firsov, *Nature* **2005**, *438*, 197-200.
[19] Y. Zhang, T.-T. Tang, C. Girit, Z. Hao, M. C. Martin, A. Zettl, M. F. Crommie, Y. R. Shen and F. Wang, *Nature* **2009**, *459*, 820-823.
[20] W. Zhang, C.-T. Lin, K.-K. Liu, T. Tite, C.-Y. Su, C.-H. Chang, Y.-H. Lee, C.-W. Chu, K.-H. Wei, J.-L. Kuo and L.-J. Li, *ACS Nano* **2011**, *5*, 7517-7524.
[21] W. J. Yu, L. Liao, S. H. Chae, Y. H. Lee and X. Duan, *Nano Letters* **2011**, *11*, 4759-4763.
[22] D. Usachov, O. Vilkov, A. Grueneis, D. Haberer, A. Fedorov, V. K. Adamchuk, A. B. Preobrajenski, P. Dudin, A. Barinov, M. Oehzelt, C. Laubschat and D. V. Vyalikh, *Nano Letters* **2011**, *11*, 5401-5407.

[23] L. Zhao, R. He, K. T. Rim, T. Schiros, K. S. Kim, H. Zhou, C. Gutiérrez, S. P. Chockalingam, C. J. Arguello, L. Pálová, D. Nordlund, M. S. Hybertsen, D. R. Reichman, T. F. Heinz, P. Kim, A. Pinczuk, G. W. Flynn and A. N. Pasupathy, *Science* **2011**, *333*, 999-1003.
[24] T. B. Martins, R. H. Miwa, A. J. R. da Silva and A. Fazzio, *Physical Review Letters* **2007**, *98*, 196803.
[25] A. A. Balandin, S. Ghosh, W. Bao, I. Calizo, D. Teweldebrhan, F. Miao and C. N. Lau, *Nano Letters* **2008**, *8*, 902-907.
[26] C.-J. Shih, S. Lin, M. S. Strano and D. Blankschtein, *Journal of the American Chemical Society* **2010**, *132*, 14638-14648.
[27] S. Stankovich, D. A. Dikin, R. D. Piner, K. A. Kohlhaas, A. Kleinhammes, Y. Jia, Y. Wu, S. T. Nguyen and R. S. Ruoff, *Carbon* **2007**, *45*, 1558-1565.
[28] H. A. Becerril, J. Mao, Z. Liu, R. M. Stoltenberg, Z. Bao and Y. Chen, *ACS Nano* **2008**, *2*, 463-470.
[29] G. Eda, G. Fanchini and M. Chhowalla, *Nature Nanotechnology* **2008**, *3*, 270-274.
[30] K. S. Novoselov, V. I. Fal'ko, L. Colombo, P. R. Gellert, M. G. Schwab and K. Kim, *Nature* **2012**, *490*, 192-200.
[31] C. Riedl, C. Coletti and U. Starke, *Journal of Physics D-Applied Physics* **2010**, *43*.
[32] D. G. Castner, B. A. Sexton and G. A. Somorjai, *Surface Science* **1978**, *71*, 519-540.
[33] J. C. Shelton, H. R. Patil and J. M. Blakely, *Surface Science* **1974**, *43*, 493-520.
[34] L. C. Isett and J. M. Blakely, *Surface Science* **1976**, *58*, 397-414.
[35] S. Bae, H. Kim, Y. Lee, X. Xu, J.-S. Park, Y. Zheng, J. Balakrishnan, T. Lei, H. Ri Kim, Y. I. Song, Y.-J. Kim, K. S. Kim, B. Ozyilmaz, J.-H. Ahn, B. H. Hong and S. Iijima, *Nature Nanotechnology* **2010**, *5*, 574-578.
[36] D. V. Kosynkin, A. L. Higginbotham, A. Sinitskii, J. R. Lomeda, A. Dimiev, B. K. Price and J. M. Tour, *Nature* **2009**, *458*, 872-U875.
[37] M. Choucair, P. Thordarson and J. A. Stride, *Nature Nanotechnology* **2009**, *4*, 30-33.
[38] A. Chakrabarti, J. Lu, J. C. Skrabutenas, T. Xu, Z. Xiao, J. A. Maguire and N. S. Hosmane, *Journal of Materials Chemistry* **2011**, *21*, 9491-9493.
[39] G. Giovannetti, P. A. Khomyakov, G. Brocks, V. M. Karpan, J. van den Brink and P. J. Kelly, *Physical Review Letters* **2008**, *101*.
[40] J. A. Moulijn, A. E. van Diepen and F. Kapteijn, *Applied Catalysis A: General* **2001**, *212*, 3-16.
[41] Y. S. Dedkov and M. Fonin, *New Journal of Physics* **2010**, *12*.
[42] S. Marchini, S. Günther and J. Wintterlin, *Physical Review B* **2007**, *76*, 075429.
[43] S. K. Hamalainen, M. P. Boneschanscher, P. H. Jacobse, I. Swart, K. Pussi, W. Moritz, J. Lahtinen, P. Liljeroth and J. Sainio, *Physical Review B* **2013**, *88*.
[44] V. Lee, C. Park, C. Jaye, D. A. Fischer, Q. Yu, W. Wu, Z. Liu, J. Bao, S.-S. Pei, C. Smith, P. Lysaght and S. Banerjee, *The Journal of Physical Chemistry Letters* **2010**, *1*, 1247-1253.
[45] G. Bertoni, L. Calmels, A. Altibelli and V. Serin, *Physical Review B* **2005**, *71*, 075402.
[46] P. A. Khomyakov, G. Giovannetti, P. C. Rusu, G. Brocks, J. van den Brink and P. J. Kelly, *Physical Review B* **2009**, *79*, 195425.
[47] P. J. Loferski in *Platinum group metals*, *Vol . 1* (Ed. U. S. G. Survey), **2012**.

Chapter 2: Techniques

2.1 Surface science

Surface science is the study of the chemical and physical phenomena which occur at the interface of two phases. It is important in fields such as molecular electronics, coatings, and heterogeneous catalysis. The importance of surface science has been recognised since the beginning of the 20th century, but it was only when ultra-high vacuum (UHV) became widely available in the 1960s that the research really took off.[1] UHV is classified as a vacuum of better than 1×10^{-9} mbar and is important in surface science as it keeps the composition of the surface reasonably constant, over the course of an experiment. For a full monolayer of a species to cover the surface, one langmuir of exposure is required, which is 1×10^{-6} mbars for one second, assuming a sticking coefficient of one. One langmuir is the minimum dose per unit time to achieve full coverage, with the sticking coefficient depending on the molecule and the reactivity of the surface. The composition of the surface can be kept reasonably constant for over a week, with pumps capable of reducing the pressure to the region of 10^{-11} mbar, along with further reduction by cooling of the instrument and sample using liquid helium (cryo-pumping).

For the study of graphene on metal surfaces in this thesis, various surface science techniques were used. The main technique used was scanning tunnelling microscopy (STM) which allows localised imaging of the surface on a molecular, and sometimes even atomic, level. Low energy electron diffraction (LEED) was also used which is an averaging technique for sampling relatively large areas of the surface, giving information about surface symmetry and the packing of adsorbates. The final technique used was high resolution electron energy loss spectroscopy (HREELS). This technique probes the vibrational modes of the adsorbates on the surface to give information about the bonding present. Also, due to the selection rules, information can be obtained on the orientation of the adsorbates.

2.2 Scanning tunnelling Microscopy (STM)

The STM was invented in 1981 by Binnig and Rohrer at the IBM research laboratory in Zurich.[2] [3] In 1986 they were awarded half of the Nobel Prize in physics "for their design of the scanning tunnelling microscope".[4] The other half went to Ernst Ruska "for his fundamental work in electron optics, and for the design of the first electron microscope".[4] The invention of both these microscopes was a huge step forward, as they allowed a much greater resolution than an optical microscope, and enabled the imaging of individual molecules and atoms. The resolution of an optical microscope is limited by the diffraction limit which is related to the wavelength of light with the highest resolution possible in the region of 100s of nanometres. The STM achieves high resolution, by not directly imaging the surface, but by probing it with an atomically sharp tip using the concept of quantum tunnelling.

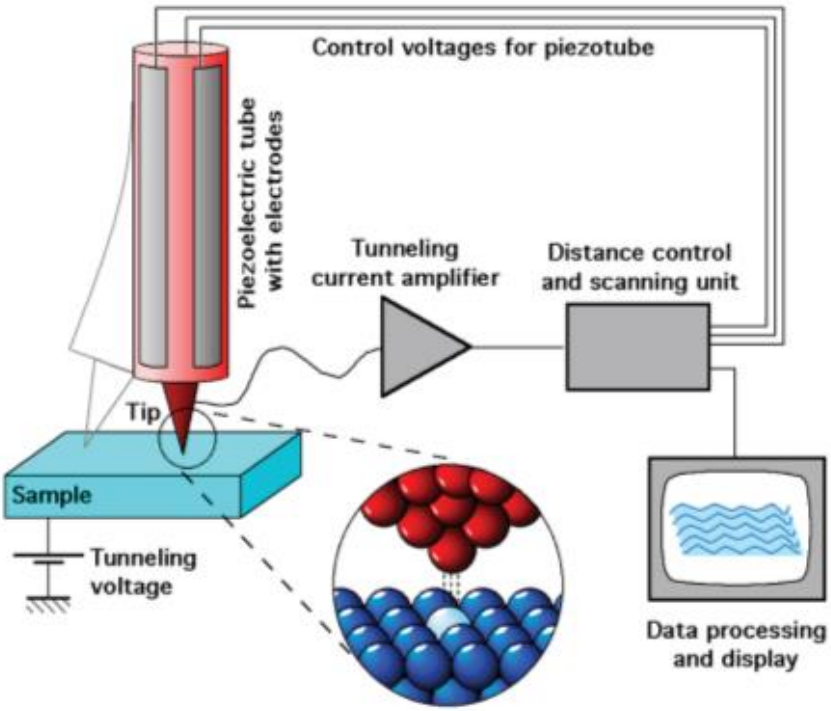

Figure 2.1

Schematic of an STM. Taken from Michael Schmid, TU Wien.

A schematic of an STM is shown in figure 2.1. Piezo-electric actuators are used to bring the atomically sharp tip close to the surface. A voltage is applied to either the tip or the

sample to create a bias, and when the tip is close to the surface, in the region of a few ångstroms, electrons can tunnel through the vacuum between the tip and sample creating a current. The tip is scanned over the surface, and variations in surface height and electron density change the current. In the more commonly used constant current mode, a feedback loop regulates the tip position by using piezoelectric tubes to change the height of the tip above the surface, to maintain a constant current. The changes in height are recorded by computer software to produce a topographic image which is a convolution of geometric and electronic effects. In constant height mode, no feedback loop is present as the height of the tip does not change as it scans over the surface, with the changes in current recorded to produce an image. Due to the absence of a feedback loop, constant height images can be acquired faster, but one has to ensure that the surface is relatively flat, otherwise a risk of crashing the tip during scanning exists.

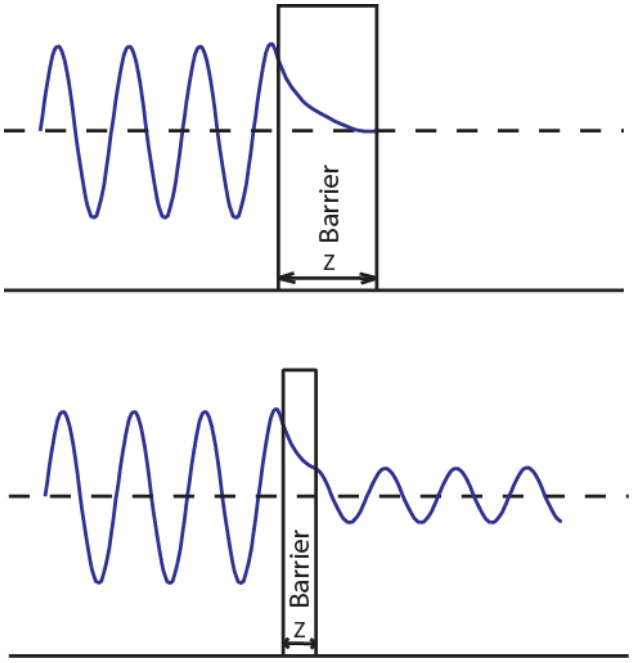

Figure 2.2

Two examples of an electron approaching a barrier. In the top example, the barrier is too thick and the wave decays to zero before exiting the barrier; but in the second example, the wave can tunnel through to the other side of the barrier.

Quantum tunnelling, which is the basis for STM, has been known to physicists since the introduction of quantum mechanics in the 1920s.[5] Quantum tunnelling is the process by which a particle, such as an electron, tunnels through a potential energy barrier that

according to classical physics it should not be able to do. Classically, if the electron energy is less than the barrier height it will be reflected. In quantum mechanics however, there is a small probability that the electron will not be reflected, but will be transmitted through the barrier by the process of tunnelling. Electrons have wavelike properties, and tunnelling is a consequence of this wavelike nature. The electron waves do not end abruptly at the wall but decay exponentially within the potential barrier. In figure 2.2 are two examples of an electron wave approaching a barrier. In the first example, the barrier is too thick for the wave to penetrate through to the second region, and it decays to zero before it reaches the other side of the barrier. In the second example, the wave has not decayed to zero by the time it has reached the other side, so there is a small probability that the electron will be found on the other side of the barrier. In STM the tunnelling current (*I*) is the probability of the electron crossing the barrier, and can be described by the following equation

$$I \approx c \cdot e^{-2k_1 z}$$

where *c* is a constant, *z* is the width of the barrier and

$$k_1 = \sqrt{2m(E - V_0)/\hbar^2}$$

where *m* is the mass of the electron, *E* is the energy of the electron, and V_0 is the height of the barrier.

These equations show that a very small change in the tip-sample separation results in a relatively large change in current due to the exponential relationship. This has led to the STM being so successful, as it allows changes that are less than a fraction of the atomic height to be detected.

Figure 2.3 shows a schematic for the tip-sample tunnelling that occurs in STM. For tunnelling to occur, the electrons must exist in a filled state in the negatively charged sample (or tip), at the same energy where unfilled states occur in the positively charged tip (or sample). Therefore, only electrons with energies between the Fermi levels of the sample and tip can tunnel. This restriction is the reason that the tunnelling current can be related to the density of states in the sample. The higher the density of states the greater the tunnel current. The density of states, along with a possible band gap of the surface

and any molecules or other materials on the surface, can be probed using surface spectroscopy. Surface spectroscopy is done with an STM by placing the tip over a specific position on the sample and measuring the current (*I*), voltage (*V*), or tip-sample distance (*Z*) while altering one or both of the others. One of the simplest spectra to run is an *I/V* curve. This involves holding *Z* constant, while varying *V* and measuring *I* which can give information on the band gap of the sample, if present. By differentiating the *I/V* curve at each voltage, a d*I*/d*V* curve is acquired, which shows the local electronic density of states perpendicular to the surface at the position of the tip.

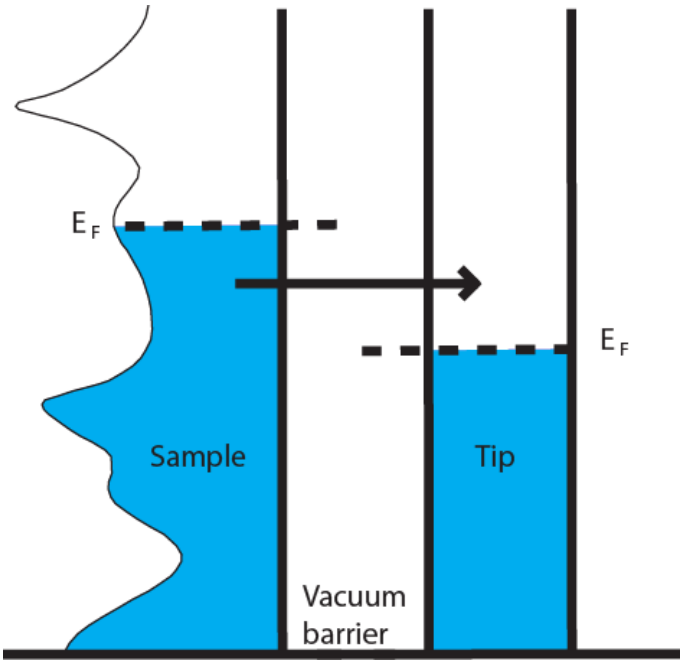

Figure 2.3

Schematic of tip-sample tunnelling with a negative bias applied to the sample. This effectively raises the Fermi level of the sample with respect to that of the tip. This allows the filled states (shown in blue) of the sample to tunnel into the empty states of the tip.

2.3 Low energy electron diffraction (LEED)

LEED was invented in 1927 by Clinton Davisson[6] [7] who went on to win the Nobel Prize in 1937 jointly with George Paget Thomson "for their experimental discovery of the diffraction of electrons by crystals".[8] LEED is a technique to study surfaces and gain information on the size, symmetry, and rotational alignment of an adsorbate unit cell with respect to the unit cell of the surface. LEED uses a beam of electrons with a well-defined energy, normally in the region of 20-200 eV, which is aimed (usually in a normal

incidence) at the sample with the scattered electrons generating a diffraction pattern on the fluorescent screen. It is the elastically-scattered electrons that contribute to the diffraction pattern with the secondary electrons removed by energy-filtering grids placed in front of the screen.

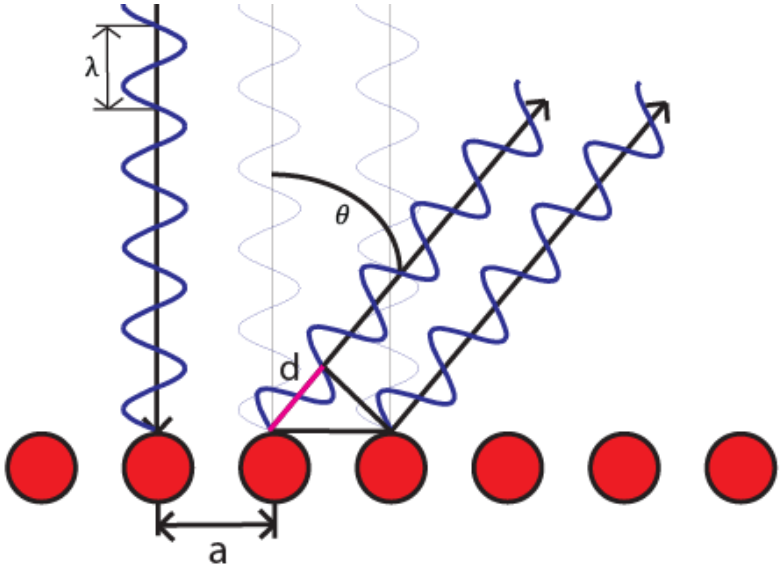

Figure 2.4

Schematic of electron diffraction on a row of atoms.

Figure 2.4 is a schematic showing electron diffraction on a row of atoms. λ is the De Broglie wavelength of an electron and can be described by the equation

$$\lambda = \frac{h}{\sqrt{2mE}}$$

where *h* is Planck's constant, *m* is the mass of the electron, and *E* is the kinetic energy. The electron beam impinges the atoms with normal incidence, and the waves are scattered by regions of high localised electron density, i.e. the atoms, at an angle ϑ. *a* is the interatomic spacing and d is the "path difference" in the distance the electron has to travel to the detector which is $a \cdot \sin\vartheta$. For constructive interference to occur at the detector, the path difference must be equal to an integral number of wavelengths.

Therefore

$$n\lambda = a \cdot sin\vartheta$$

where *n* is an integer. This relation is the well-known Bragg condition for diffraction.

The observed LEED pattern is a scaled representation of the reciprocal lattice of the surface which can be used to extract the real space symmetry and dimensions of the surface unit cell. Figure 2.5 shows a model of a surface with adsorbates in a c(4×2) configuration and the corresponding LEED pattern. In order to calculate the ordering of the adsorbates on the surface from the LEED pattern, the reciprocal vectors need to be examined. For the substrate in the figure, these are $\mathbf{a_1}^*$ and $\mathbf{a_2}^*$, with their real space counterparts being $\mathbf{a_1}$ and $\mathbf{a_2}$, respectively. $\mathbf{a_1}^*$ is perpendicular to $\mathbf{a_2}$ and $\mathbf{a_2}^*$ is perpendicular to $\mathbf{a_1}$. For the adsorbates, the reciprocal vectors are $\mathbf{b_1}^*$ and $\mathbf{b_2}^*$ which have the same relationship to their real space counterparts, $\mathbf{b_1}$ and $\mathbf{b_2}$, as for the substrate. The relationship between the lengths of $\mathbf{a_1}$ and $\mathbf{a_1}^*$, or similarly for $\mathbf{a_2}$ and $\mathbf{a_2}^*$, is $|\mathbf{a_1}| = 1/(|\mathbf{a_1}^*|\cos(A))$, where A is the angle between the vectors $\mathbf{a_1}$ and $\mathbf{a_1}^*$. If the angle is zero a simple reciprocal relationship exists since cos(0)=1.

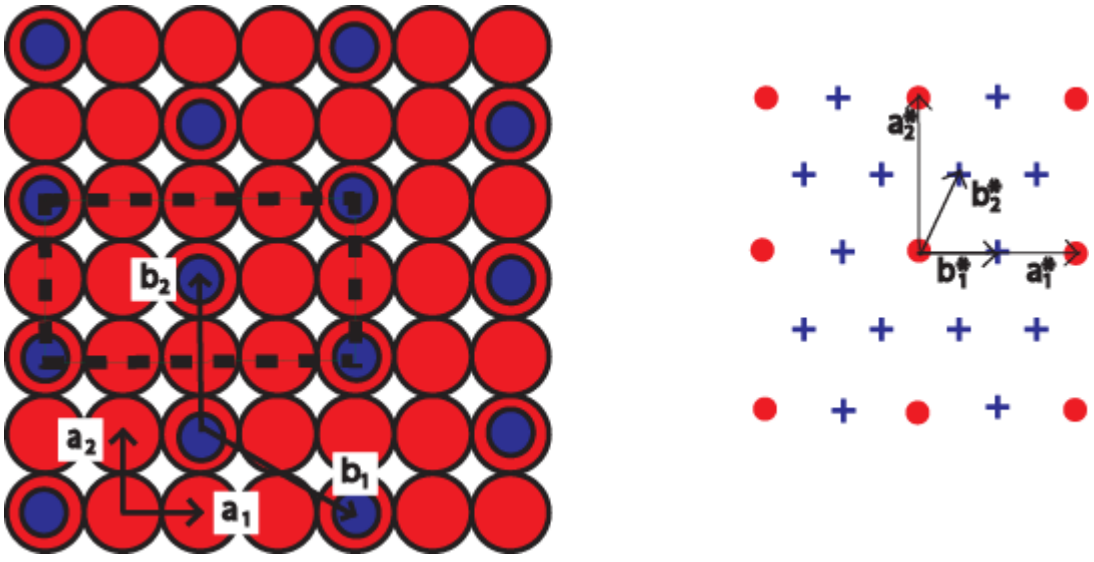

Figure 2.5

On the left is a model of a (100) surface with adsorbates (blue) arranged in a c(4×2) configuration. On the right is a model of the corresponding LEED pattern.

2.4 High resolution electron energy loss spectroscopy (HREELS)

Electron energy loss spectroscopy (EELS) was developed in the 1940s by James Hillier and R.F. Baker.[9] There are several types of EELS techniques which all involve exposing a sample to a beam of monoenergetic electrons, with some electrons undergoing inelastic scattering, which can give information about the surface and any molecules on it. HREELS shows the vibrational modes present on the surface by looking at small energy losses between 10^{-3} and 1 eV.

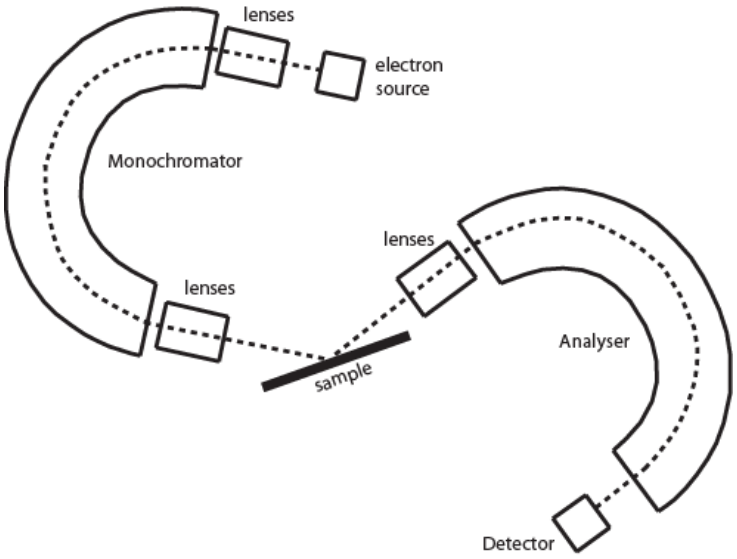

Figure 2.6 Schematic of a HREELS setup.

Figure 2.6 shows a schematic of a HREELS setup. The electrons travel from the source, which is often a tungsten cathode, through a series of lenses which focus the beam into an electron monochromator. The monochromator reduces the energy of the passing electrons, and only allows electrons to pass which have the chosen initial energy (typically 5-10 eV). These electrons are focused onto the sample, where some electrons lose energy due to the vibrational modes of the molecules on the surface. These electrons, along with the elastically scattered electrons, go into the analyser. Most of the electrons are elastically scattered, giving rise to a large elastic peak. To the left of this peak, on the low kinetic energy side, is a gently sloping background, with the peaks from electrons which have been inelastically scattered due to the vibration modes of the molecules. The vibrational modes which can be observed depend on the selection rules

and whether specular or off-specular mode is used. In specular mode, the incident angle is the same as the reflection angle, with only the vibrations which give rise to a dipole change normal to the surface being observed. In off-specular mode, where the incident angle is different to the reflection angle, all vibrational modes can be observed, but they are all relatively weak compared to the specular mode.

References

[1] D. P. Woodruff and T. A. Delchar, *Modern techniques of surface science*, Cambridge University Press, Cambridge, **1994**, p. 586.
[2] G. Binnig, H. Rohrer, C. Gerber and E. Weibel, *Applied Physics Letters* **1982**, *40*, 178-180.
[3] G. Binnig, H. Rohrer, C. Gerber and E. Weibel, *Physical Review Letters* **1982**, *49*, 57-61.
[4] in *"The Nobel Prize in Physics 1986". Nobelprize.org. Nobel Media AB 2013. Web. 25 Feb 2014.* <*http://www.nobelprize.org/nobel_prizes/physics/laureates/1986/*>
[5] R. H. Fowler and L. Nordheim, *Proceedings of the Royal Society of London* **1928**, *A119*, 173-181.
[6] C. Davisson and L. H. Germer, *Nature* **1927**, *119*, 558-560.
[7] C. Davisson and L. H. Germer, *Physical Review* **1927**, *30*, 705-740.
[8] in *"The Nobel Prize in Physics 1937". Nobelprize.org. Nobel Media AB 2013. Web. 26 Feb 2014.* <*http://www.nobelprize.org/nobel_prizes/physics/laureates/1937/*>
[9] J. Hillier and R. F. Baker, *Journal of Applied Physics* **1944**, *15*, 663-675.

Chapter 3: Experimental

3.1 Instruments and methodology

3.1.1 The UHV system

The UHV system (figure 3.1a) is on a concrete block to reduce vibrations by isolating it from the rest of the building. To further reduce vibrations, the whole system can be lifted using Newport dampers. The chamber is built from stainless steel, which is typical for UHV systems, with a base pressure in the 10^{-11} mbar range. There are four chambers separated by UHV gate-valves; the load lock (LL) chamber, the turbo stage (turbo) chamber, the preparation (prep) chamber, and the STM chamber. The LL is used for fast entry of new samples and tips. Once the new sample is in the LL, the valve is opened to the turbo chamber to reduce the pressure. The turbo chamber is pumped by a 240 $L \cdot s^{-1}$ turbo-molecular pump, which is backed by a smaller turbo-molecular pump (60 $L \cdot s^{-1}$) and an oil-free diaphragm pump. Once a suitable pressure has been reached in the LL, the sample can be transferred to the prep chamber, using the transfer arm. In the prep chamber there is a "garage" which has space to store four samples and six tips. In the prep chamber, the sample is held on a manipulator, which has a differentially pumped rotary feedthrough that is pumped regularly by a turbo-molecular drag pumping station. This pumping station has a 60 $l \cdot s^{-1}$ turbo-molecular pump, backed by a diaphragm pump. The majority of sample preparation is done in the prep chamber, but the LL can be used if organic molecules with a relatively high vapour pressure need to be deposited.

The prep chamber is pumped on by an ion pump with an integrated titanium sublimation booster pump. For processes such as sputtering, the ion pump is sealed off and the chamber is pumped on using the turbo stage. Sputtering is normally performed with Ar^+ ions using a Specs ion source IQE, with the argon entering the chamber through a piezo leak valve from the gas-line. The argon gas-line is separated from the other gas-lines as it is used more often and needs to be frequently topped up, so this ensures cleanliness.

After sputtering, the sample is usually annealed to high temperatures using connections between the manipulator and sample holder to pass the current. There are further connections, allowing the temperature to be measured using a Type K (chromel – alumel)

thermocouple. Once several sputter anneal cycles have been performed, the cleanliness of the sample can be examined using LEED and auger electron spectroscopy (AES). The Specs ErLEED is mounted on a DN 150 CF flange, with reverse view optics, allowing the diffraction pattern to be observed at the position of the flange. The 4-grid LEED optics can also be used as an electron analyser, allowing the recording of AES.

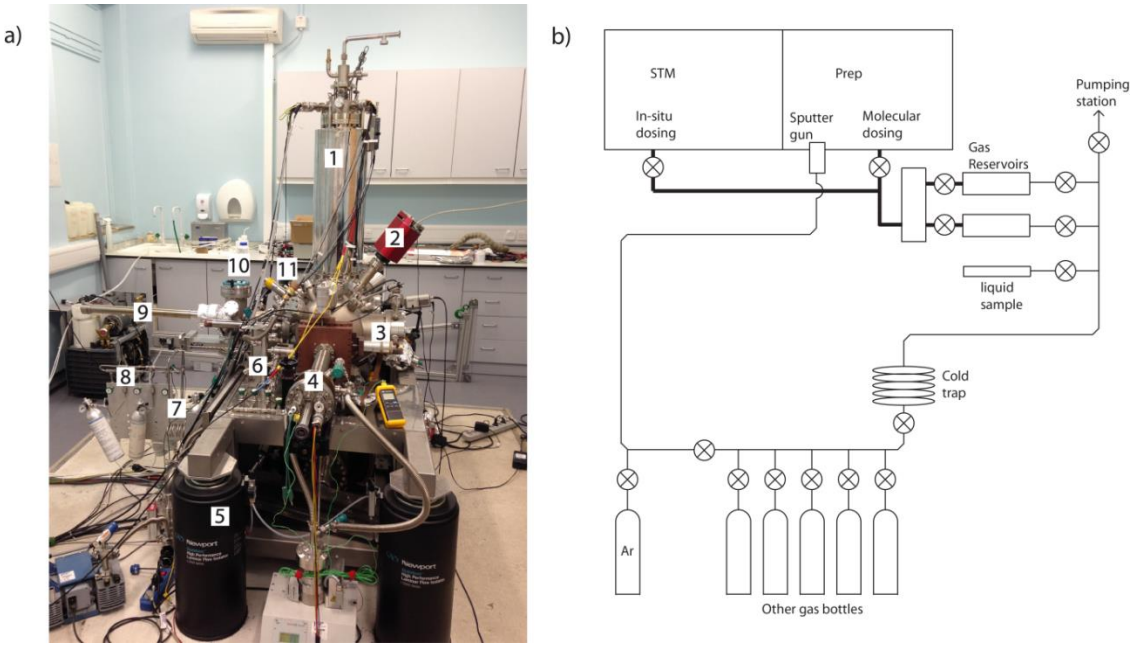

Figure 3.1
(a) Overview of the UHV system. (1) LN_2/LHe bath cryostat; (2) mass spec.; (3) LEED/AES; (4) manipulator; (5) Newport dampers; (6) gas reservoirs; (7) cold trap; (8) gas bottles; (9) transfer arm; (10) LL; (11) sputter gun. (b) Schematic of the gas-line system.

After preparing a clean surface, molecules can be deposited on it using the gas line or an evaporator. Figure 3.1b shows a schematic of the gas line system. The gas line system has space for six bottles, including the argon, which is separated from the rest by a valve as described previously. The gas line system is connected to the same pump used for the rotary feedthrough of the manipulator, and has two gas-reservoirs and space to connect liquid samples to be vaporised into the system. The gas-reservoirs have a size of about 15 cm^3 and have a leak valve, with fine control of the pressure of gas exposed to the prep or STM chamber. For further purification of gases, there is a cold trap that can be used which is cooled by liquid nitrogen. To check the purity of the gases during deposition, a Pfeiffer QMG 220 Prisma Plus compact mass spectrometer is attached to the prep chamber.

For solid adsorbates, a molecular evaporator is used (figure 3.2). The molecules are stored in a glass vial, with a tantalum wire coiled round for heating the molecules to their sublimation temperature. The temperature is monitored using a Type K thermocouple attached to the glass vial. If the sample is not cooled for deposition, then the sample is cooled afterwards through the manipulator using liquid nitrogen (or helium), followed by transfer to the STM chamber for scanning.

Figure 3.2

Organic molecule evaporator.

3.1.2 The CreaTec low-temperature STM

The STM chamber is pumped on using an identical ion pump to that in the prep chamber. Pressures can be further improved by cooling the cryostats. It is estimated that the local pressure in the sample stage of the STM is probably in the 10^{-15} mbar range due to this. There is an outer cryostat of 15 L and an inner cryostat with a volume of 4 L. The outer cryostat is cooled using liquid nitrogen (LN_2), and the inner cryostat can be cooled using either LN_2 or liquid helium (LHe), depending on the requirements for the experiment. The STM hangs free from the inner cryostat, and is surrounded by radiation shields. The STM is a slightly modified Besocke-beetle-type.[1] A schematic of this design is shown in figure 3.3 alongside an image of the STM. The tip points downwards towards the sample, and is

attached to the main piezo by a magnet. The main piezo is attached to the ramp which rests on three outer piezos. All four piezos have electrodes allowing precise in-plane movement, but only the main piezo has an electrode enabling it to extend and retract. This is used during scanning to alter the height of the tip using the feedback loop, and also during the automated approach sequence. Before the automated approach sequence can be started, the tip needs to be optically close to the surface, and this is done using the outer piezos, which move it down using a rotation of the ramp around a central axis. For the automated approach sequence, the main piezo fully retracts the tip, and the outer piezos rotate the ramp step-by-step. At each step, the tip extends fully using the main piezo, and checks for a tunnelling current at a set-point defined by the user. If this tunnelling current is not detected, then the tip is retracted, and the ramp is rotated another step. When the tunnelling current is detected between tip and sample, the approach sequence stops, and measurements can begin.

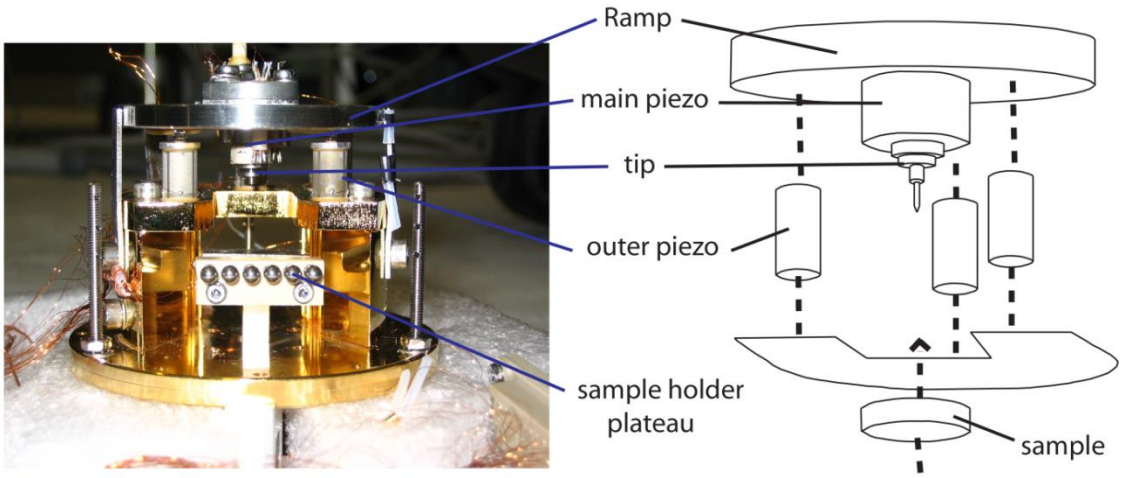

Figure 3.3

Picture of the CreaTec STM alongside a schematic of the design.

3.1.3 Tip preparation

In order to acquire high quality STM images, an atomically sharp tip is required. For our experiments the tip is made from either W or Pt/Ir. W is most often used, as it is fairly easy to produce a very sharp tip by electrochemical etching. The device used for the etching is shown in figure 3.4. The W wire is placed into the tip holder and held over a Ta loop with a bubble film of NaOH (~25 wt%). The vertical position of the tip holder is then

adjusted, so that the required length for the tip is above the loop, with the remaining length passing through the loop. A positive bias is applied to the W wire, and a negative bias to the Ta loop, with the etching occurring at the point where the wire passes through the NaOH. The reaction taking place is shown below

$Tip\ (anode)$: $W + 8OH^- \rightarrow WO_4^{2-} + 4H_2O + 6e^-$

$Loop\ (cathode)$: $6H_2O + 6e^- \rightarrow 3H_2 + 6OH^-$

$$\boldsymbol{W + 2H_2O + 2OH^- \rightarrow WO_4^{2-} + 3H_2}$$

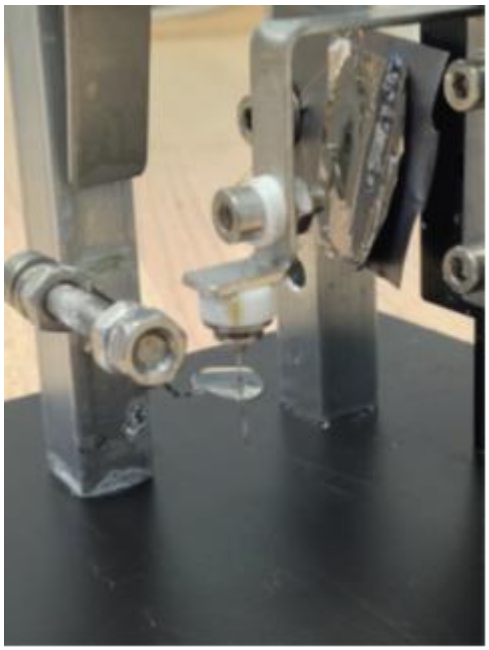

Figure 3.4

Device used for electrochemically etching the W tips.

The section of the wire being etched becomes gradually thinner, until the end drops off leaving a sharp tip in the tip holder. The tip is then rinsed with deionised water and ethanol and kept for a limited time in a beaker of ethanol (so as to minimize oxidation with ambient atmosphere), until the tips are ready to be transferred into the LL.

The other material used for the tips, Pt/Ir, is more chemically inert than the W and so is usually used for spectroscopic measurements. The W is more easily oxidised and this can complicate the electronic spectra. The Pt/Ir tip is produced by mechanical cutting of the

Pt/Ir wire (80%/20%). This is less controllable than the electrochemical etching, but a sharp tip can usually be prepared, if the wire is cut in the direction almost parallel to its axis while the wire is pulled tight. Like for the W tips, the Pt/Ir tip is rinsed and stored in ethanol till it is transferred into UHV. The tips can be further cleaned in the prep chamber by Ar^+ sputtering, and annealing by electron bombardment using a filament mounted on the garage. However, experience has found this to be unnecessary. A tip is transferred to the STM using the fork tool, which is stored on the garage and can be picked up by the manipulator.

Once in the STM, the tip is further sharpened by voltage pulses and small, controlled tip crashes into the surface of the sample. There is no set method for sharpening the tip, and it tends to be a repeated trial and error method. Usually, it starts off with small voltage pulses, and if scanning shows no improvement then higher voltages are used or small tip crashes into the surface. With experience, it becomes easier to identify how good the tip is and quicker to get it to the right state.

3.1.4 The HREELS system

HREELS experiments were carried out in a separate UHV system. It consists of a LL, prep chamber and analysis chamber. The prep chamber is equipped with an ion gun for sputtering the sample, and means to heat the sample through the manipulator. There is a gas line, with argon for the sputtering, and space for other gas bottles, that may be needed for sample preparation. The same molecular evaporator was used in both UHV systems, to keep deposition fluxes consistent in both setups. The prep chamber is also equipped with a LEED. The analysis chamber houses the Ibach EELS double pass spectrometer. The monochromator can be rotated to change the angle to the analyser, and the instrument is cooled using liquid nitrogen.

3.2 The Rh(111) crystal

3.2.1 Preparation of the Rh(111) surface

The study of graphene growth in this thesis will be investigated on a Rh(111) surface. For the STM measurements a top-hat shaped single crystal of Rh(111) (5 mm × 3 mm) was purchased from MaTeck, and was mounted on the CreaTec sample holder (figure 3.5).

The sample is completely isolated from the sample holder using ceramics. The sample sits on top of a button heater oven, and is clamped in place using a star-shaped Mo clamp. The oven has two Cu wires for heating, and there are two thermocouple wires, that are in contact with the sample (type K). These wires are soldered to the metal contacts on the sample holder, which attach to the contacts on the manipulator when the sample is held. These contacts are made from tantalum, not alumel and chromel. Therefore, it is important that the sample holder is kept at RT during annealing to minimise temperature-reading errors. This is done by counter cooling the manipulator during annealing using liquid nitrogen. Despite this, it is expected that an error of ±50 K exists during annealing.

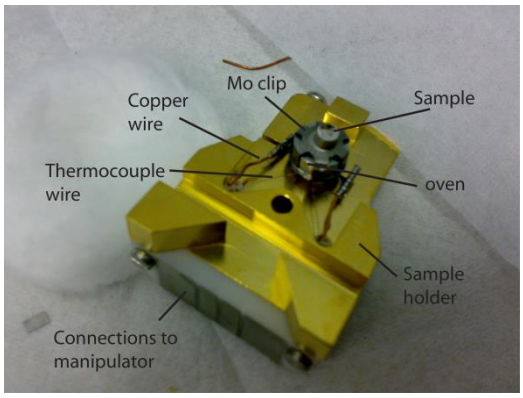

Figure 3.5

The CreaTec sample holder with mounted sample.

For the HREELS measurements a different single crystal of Rh(111) is used. This sample is wafer shaped (8 mm × 8 mm × 1 mm) and was also purchased from MaTeck. In this case, the sample is heated by electron bombardment on the back side of the holder. For both samples, the cleaning methods were the same and involved cycles of sputtering and annealing. Sputtering was done with Ar^+ (1×10^{-6} mbar) with an energy of 1.5 keV for 10 mins, with an emission current of 10 mA and the current on the sample measured at 1 µA. Then the sample was annealed in oxygen (1×10^{-6} mbar) for 5 minutes at a temperature of 700°C. After this the oxygen was removed from the system, with the sample continuing to heat for a further 15 minutes, while the vacuum recovered.

Between experiments the sample needed just a couple of cycles to clean, but if the sample had been out of the UHV it required more cycles.

3.2.2 General features of the Rh(111) surface

Rh(111) has a hexagonal symmetry with an interatomic distance of 2.69 Å. The single crystal is known to have a face-centred cubic (fcc) structure giving ABC-type stacking of the rhodium layers. In figure 3.6 is an STM image with atomic resolution over the step edges on the bare rhodium surface alongside a model. From the model it can be seen that the two hollow sites are inequivalent with one having a second layer atom beneath, and one a third layer atom. These two hollow sites are called fcc (third layer atom beneath) and hcp (second layer atom beneath).

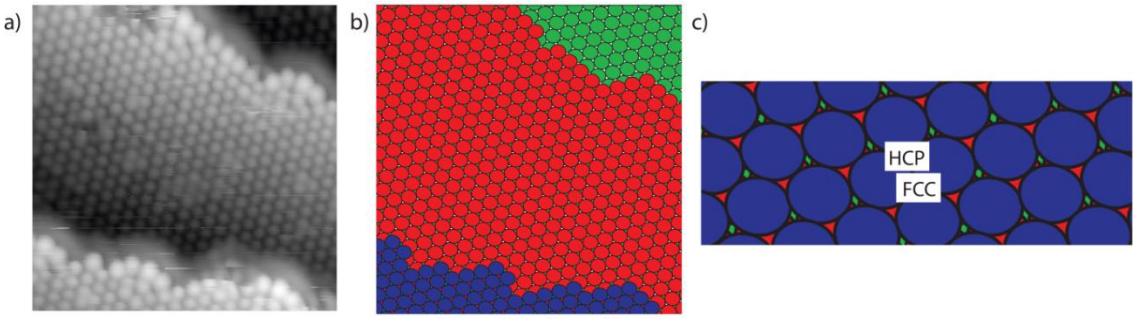

Figure 3.6

(a) is an STM image of the bare Rh(111) surface with atomic resolution over two step edges. (b) is a model of the STM image in (a) with a zoom in shown in (c) which indicates the difference between the hcp and fcc sites.

The Rh(111) crystal is prone to dislocations. Some dislocations occur below the surface, and these result in the surface appearing bumpy. A bumpy surface can also be due to argon bubbling. During sputtering, some of the high energy argon ions are impacted into the bulk of the crystal and are not brought to the surface during the anneal cycle. A bumpy surface makes it tricky to analyse the image, as it can be difficult to observe all adsorbates at once since the background cannot be levelled (figure 3.7a). This, however, can be overcome with image processing but can be time consuming. A second type of dislocation is a step dislocation (figure 3.7b). This distorts the local rhodium lattice and decreases the coordination of the atoms, like at step edges. These tend to be more reactive, and there is often a higher density of molecules at these defects. In figure 3.7c is another type of defect seen on the Rh(111) surface; a triangular vacancy defect. This is

where the top layer of atoms is missing in the shape of a triangle in the middle of a terrace. This is thought to be due to incomplete healing of the surface during annealing.

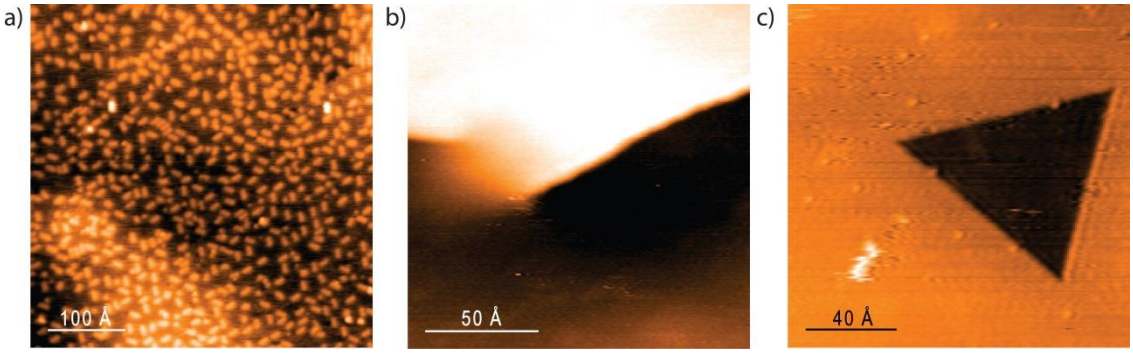

Figure 3.7

Examples of common structural imperfections present for the rhodium crystal. (a) is an STM image of tetracene on Rh(111) which has a bumpy surface due to lattice dislocations below the surface. The STM image in (b) is of a step dislocation and (c) is a triangular vacancy defect.

Rhodium is part of the group VIIIb transition metals which are fairly reactive unlike nearby gold and silver. It is, therefore, important to limit its exposure to pollutants as much as possible. The mass spec shows that the residual gas in the prep chamber mainly comprises of H_2, H_2O, and CO. CO is known to bind strongly to the rhodium surface[2] and H_2 readily adsorbs dissociatively on it.[3] Because of this it is important to transfer the sample from the prep chamber to the STM as quickly as possible after sample preparation. Surface pollution also comes from the crystal itself. This is mainly in the form of dissolved carbon which is common in many transition metals. Its concentration is very low but it segregates to the surface upon annealing. Repeated cycles of sputtering and annealing can remove it from the top portion of the bulk, near the surface. To help remove the carbon from the surface, oxygen is used during annealing. Rhodium is a good oxidation catalyst so the removal of carbon can be achieved by oxidation to CO or CO_2, with both species desorbing at the annealing temperatures.[4]

3.3 The Cu(110) crystal

3.3.1 Preparation of the Cu(110) surface

The study of the epitaxial relationship between graphene and copper in this thesis will be investigated on a Cu(110) surface. For this a top-hat shaped single crystal from MaTeck, similar to the Rh(111) crystal was used. It was mounted in a similar way to the rhodium crystal and was cleaned using cycles of sputtering and annealing. Sputtering was done with Ar^+ (1×10^{-6} mbar) with an energy of 1.5 keV for 10 mins, with an emission current of 10 mA and the current on the sample measured at 1 μA. The sample was then annealed at a temperature of 500°C for 15 minutes.

3.3.2 General features of the Cu(110) surface

Cu(110) has a fcc structure with rectangular surface symmetry. The surface consists of rows of atoms with an interatomic distance of 2.56 Å. The interatomic distance of atoms in adjacent rows is 3.62 Å. The (110) surface is a lot more open than the (111) with the second layer of atoms exposed. Unlike the rhodium surface, the copper is not prone to dislocations. It does, however, still have problems with pollution, particularly from CO. On the copper surface, as is the case on other metal surfaces, the CO appears as either a protrusion or indentation, depending on the adsorption site (and tunnel parameters). When adsorbed on a top-site (directly on top of a surface atom) it appears as a protrusion. But when adsorbed on a short-bridge site (between two atoms in a row) it appears as a depression, or, with a sharp tip, a “sombrero”.

References

[1] K. Besocke, *Surface Science* **1987**, *181*, 145-153.
[2] A. Dekoster and R. A. Vansanten, *Surface Science* **1990**, *233*, 366-380.
[3] J. T. Yates Jr, P. A. Thiel and W. H. Weinberg, *Surface Science* **1979**, *84*, 427-439.
[4] S. N. Mikhailov, L. C. A. Vandenoetelaar, H. H. Brongersma and R. A. Vansanten, *Catalysis Letters* **1994**, *27*, 79-90.
[5] J. C. Shelton, H. R. Patil and J. M. Blakely, *Surface Science* **1974**, *43*, 493-520.
[6] X. Li, W. Cai, L. Colombo and R. S. Ruoff, *Nano Letters* **2009**, *9*, 4268-4272.
[7] E. C. Neyts, A. C. T. van Duin and A. Bogaerts, *Nanoscale* **2013**, *5*, 7250-7255.
[8] F. Schwierz, *Nat Nano* **2010**, *5*, 487-496.
[9] R. Cheng, J. Bai, L. Liao, H. Zhou, Y. Chen, L. Liu, Y.-C. Lin, S. Jiang, Y. Huang and X. Duan, *Proceedings of the National Academy of Sciences* **2012**.
[10] Z. Guo, R. Dong, P. S. Chakraborty, N. Lourenco, J. Palmer, Y. Hu, M. Ruan, J. Hankinson, J. Kunc, J. D. Cressler, C. Berger and W. A. de Heer, *Nano Letters* **2013**, *13*, 942-947.

[11] S.-J. Han, A. V. Garcia, O. Satoshi, K. A. Jenkins and W. Haensch, *Nature Communications* **2014**, *5,*3086.
[12] R. R. Nair, P. Blake, A. N. Grigorenko, K. S. Novoselov, T. J. Booth, T. Stauber, N. M. R. Peres and A. K. Geim, *Science* **2008**, *320*, 1308.
[13] A. Reina, H. Son, L. Jiao, B. Fan, M. S. Dresselhaus, Z. Liu and J. Kong, *Journal of Physical Chemistry C* **2008**, *112*, 17741-17744.
[14] X. Liang, B. A. Sperling, I. Calizo, G. Cheng, C. A. Hacker, Q. Zhang, Y. Obeng, K. Yan, H. Peng, Q. Li, X. Zhu, H. Yuan, A. R. H. Walker, Z. Liu, L.-m. Peng and C. A. Richter, *ACS Nano* **2011**, *5*, 9144-9153.
[15] V. Geringer, D. Subramaniam, A. K. Michel, B. Szafranek, D. Schall, A. Georgi, T. Mashoff, D. Neumaier, M. Liebmann and M. Morgenstern, *Applied Physics Letters* **2010**, *96*, 82114.
[16] Y. Ren, C. Zhu, W. Cai, H. Li, Y. Hao, Y. Wu, S. Chen, Q. Wu, R. D. Piner and R. S. Ruoff, *Nano* **2012**, *7,* 1150001.
[17] X. Li, W. Cai, I. Jung, J. An, D. Yang, A. Velamakanni, R. Piner, L. Colombo and R. S. Ruoff in *Synthesis, Characterization, and Properties of Large-Area Graphene Films*, *Vol. 19* Eds.: Y. Obeng, S. DeGendt, P. Srinivasan, D. Misra, H. Iwai, Z. Karim, D. W. Hess and H. Grebel), **2009**, pp. 41-52.
[18] S. Bae, H. Kim, Y. Lee, X. Xu, J.-S. Park, Y. Zheng, J. Balakrishnan, T. Lei, H. Ri Kim, Y. I. Song, Y.-J. Kim, K. S. Kim, B. Ozyilmaz, J.-H. Ahn, B. H. Hong and S. Iijima, *Nat Nano* **2010**, *5*, 574-578.
[19] J. Kang, S. Hwang, J. H. Kim, M. H. Kim, J. Ryu, S. J. Seo, B. H. Hong, M. K. Kim and J. B. Choi, *ACS Nano* **2012**, *6*, 5360-5365.
[20] J. Perdereau, J. P. Biberian and G. E. Rhead, *Journal of Physics F-Metal Physics* **1974**, *4*, 798-806.
[21] C. Woll, S. Chiang, R. J. Wilson and P. H. Lippel, *Physical Review B* **1989**, *39*, 7988-7991.
[22] E. Gabrielyan, 2007, arXiv:physics/0703098.
[23] B. Wang, M. Caffio, C. Bromley, H. Fruchtl and R. Schaub, *Acs Nano* **2010**, *4*, 5773-5782.
[24] L. Gao, J. R. Guest and N. P. Guisinger, *Nano Letters* **2010**, *10*, 3512-3516.
[25] A. L. Walter, S. Nie, A. Bostwick, K. S. Kim, L. Moreschini, Y. J. Chang, D. Innocenti, K. Horn, K. F. McCarty and E. Rotenberg, *Physical Review B* **2011**, *84*, 195443.
[26] L. Zhao, K. T. Rim, H. Zhou, R. He, T. F. Heinz, A. Pinczuk, G. W. Flynn and A. N. Pasupathy, *Solid State Communications* **2011**, *151*, 509-513.
[27] H. I. Rasool, E. B. Song, M. Mecklenburg, B. C. Regan, K. L. Wang, B. H. Weiller and J. K. Gimzewski, *Journal of the American Chemical Society* **2011**, *133*, 12536-12543.
[28] P. M. Ajayan and B. I. Yakobson, *Nat Mater* **2011**, *10*, 415-417.
[29] G. H. Han, F. Guenes, J. J. Bae, E. S. Kim, S. J. Chae, H.-J. Shin, J.-Y. Choi, D. Pribat and Y. H. Lee, *Nano Letters* **2011**, *11*, 4144-4148.
[30] J. Gao, J. Yip, J. Zhao, B. I. Yakobson and F. Ding, *Journal of the American Chemical Society* **2011**, *133*, 5009-5015.
[31] N. Wilson, A. Marsden, M. Saghir, C. Bromley, R. Schaub, G. Costantini, T. White, C. Partridge, A. Barinov, P. Dudin, A. Sanchez, J. Mudd, M. Walker and G. Bell, *Nano Research* **2013**, *6*, 99-112.
[32] M. Ishihara, Y. Koga, J. Kim, K. Tsugawa and M. Hasegawa, *Materials Letters* **2011**, *65*, 2864-2867.
[33] J. M. Wofford, S. Nie, K. F. McCarty, N. C. Bartelt and O. D. Dubon, *Nano Letters* **2010**, *10*, 4890-4896.
[34] G. Giovannetti, P. A. Khomyakov, G. Brocks, V. M. Karpan, J. van den Brink and P. J. Kelly, *Physical Review Letters* **2008**, *101,* 26803.
[35] P. A. Khomyakov, G. Giovannetti, P. C. Rusu, G. Brocks, J. van den Brink and P. J. Kelly, *Physical Review B* **2009**, *79*, 195425.

Chapter 4: Growth and morphology of graphene on Cu(110)

4.1 Introduction

As discussed in section 1.3, the epitaxial growth of graphene on a transition metal surface is a promising method for producing large sheets of graphene. This is done by chemical vapour deposition (CVD) of small hydrocarbons such as methane or ethene. There are two processes that can occur for the graphene formation, which depend on the metal substrate. The first is a surface adsorption process, and the second involves dissolution followed by segregation and precipitation. The surface adsorption process occurs for metals with a low solubility of carbon. By this process the transition metal surface catalyses the dehydrogenation of the hydrocarbons to leave a single monolayer of graphene on the surface. The second process occurs for metals with a high solubility of carbon, and is a 3-step process which was explained by the group of Jack Blakely in the 1970s when looking at carbon segregation on Ni(111).[5] First the carbon diffuses into the bulk, then it segregates to the surface forming a monolayer of graphene. This occurs at an intermediate temperature range; for Ni(111) this is around 800-900°C.[5] Below this temperature range precipitation of carbon from the bulk occurs, resulting in the formation of multilayer graphene. These two processes, depending on the carbon solubility of the metal, were further confirmed recently by the use of carbon isotope labelling to prepare graphene on different metal surfaces.[6]

Since it is the precipitation of the carbon at low temperature that causes the multilayer growth, it is thought that rapid cooling could prevent this, but this is yet to be achieved. A recent theoretical study had offered yet another possible solution. This involves a metal crystal which is free from carbon, at least in the subsurface region, and a high influx of carbon during growth. These conditions enable stable carbon structures to be formed before the energy barrier to diffusion into the bulk is overcome.[7] However, for the moment a metal with a low solubility of carbon is the best option for the epitaxial growth of monolayer graphene on a metal surface.

Graphene produced by this method is expected to one day be used commercially for nanoelectronics and as transparent conductive layers, among other things. In the field of

nanoelectronics, graphene looks particularly promising for integrated circuits and transistors. Graphene based transistors are considered one of the leading contenders for post-silicon electronics, and a lot of research is being put into them.[8] One of the main challenges is opening a sizeable band gap without diminishing the electronic properties that make it so desirable in the first place. The quality and performance of these transistors, however, are improving rapidly with a cut-off frequency of 400 GHz[9] recently reported, along with a maximum oscillation frequency of 70 GHz.[10] Graphene based integrated circuits are also becoming more advanced thanks to new methods that prevent deterioration of the graphene quality during back-end-of-line processes. This new method involves reversing the process so that all passive components, together with device gates, are built before the graphene is transferred.[11] This has resulted in an integrated circuit with the components integrated into 0.6 mm^2 area and fabricated onto 200 mm silicon wafers being produced.

Graphene holds even greater potential in the field of transparent conductive layers. Currently this field is dominated by the expensive indium tin oxide (ITO) so a cheaper alternative would be well received. The quality of graphene is improving dramatically with its sheet resistance less than ITO and an optical transparency of 97.7%[12] which is very close to that of ITO. Graphene also has the advantage of being highly flexible which would allow it to be used in novel flexible electronic devices which ITO would be far too rigid for.

For these electronic applications graphene would need to be transferred from the metal surface it was grown on to an insulating support. There are several methods of doing this which involve etching away the metal support. A popular method involves the use of poly(methyl methacrylate) (PMMA).[13] [14] For this method the PMMA is spin coated onto the graphene and the metal is then etched away. The graphene and PMMA are then transferred onto the target substrate, and the PMMA is removed using solvents. This method does however show strong N-type doping due to small amounts of residual PMMA or other solvents that remain on the sample.[15] [16] To overcome this, graphene can be transferred without the PMMA by flattening the graphene/foil stack and floating it on the etchant. After the foil has been removed, the graphene can be either lifted or fished out.[17] [16] To produce large sheets of graphene, a thermal release tape can be

used. In figure 4.1 is a schematic of roll-to-roll transfer of graphene, as described by Bae *et al*, for 30 inch sheets of graphene.[18] This method involves three steps; starting with the attachment of the graphene (on foil) to a thin polymer film coated with a thermal release tape. This is done by gentle pressing between two rollers. The foil is then etched away using a chemical etchant. Then the graphene is transferred from the polymer film, to the target substrate, by applying heat while passing between rollers. One drawback of this method is that the final step can cause high sheet resistance, when used for rigid target substrates. This can be overcome by using a similar method, using a hot press instead of rollers in the final stage which can uniformly distribute the mechanical load on the graphene.[19]

Due to the need of etching away the metal substrate in order to transfer it, a relatively cheap metal foil such as nickel or copper would be the ideal growth substrate. As discussed previously, however, nickel is unsuitable for the growth of monolayer graphene due to its high carbon solubility which results in multilayer growth. On the other hand, copper has very low carbon solubility so has been identified as the ideal growth substrate.

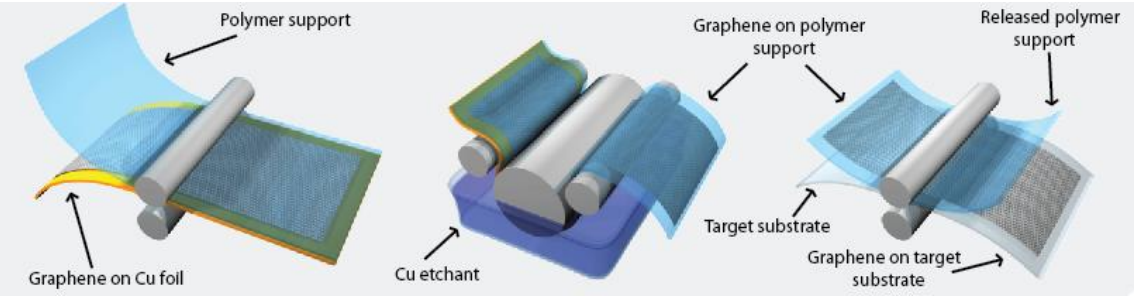

Figure 4.1

Schematic of the transfer of graphene from copper foil to an insulating support as part of the roll-to roll production method. Taken from reference [18]

4.1.1 Moiré patterns

As previously discussed in section 1.4, when there is a large mismatch in lattice constant between graphene and the transition metal surface, a large superstructure exists. This type of superstructure is referred to as a moiré pattern. This is an interference pattern, occurring when two geometrical patterns are superimposed on each other. The term

moiré originates from the textile, moire, which has a rippled appearance. In the textile, this is usually due to a technique used after the material is woven called calendaring. Calendaring involves running the material through rollers with a special ribbing which exerts differential pressure on the fabric resulting in the rippled appearance. In surface science, the moiré pattern is a result of two layers of atoms which differ in their lattice constant, n-fold symmetry, rotation angle, or a mixture of these. The resulting moiré pattern can give information about the hidden second layer of atoms. One of the most well-known example of this is the herringbone reconstruction of Au(111).[20] [21] This results from a slight contraction of the top layer of atoms along the $[1\bar{1}0]$ direction, giving a (22 × √3) reconstruction. A short discussion will be presented below on the derivation and analysis of moiré patterns. This will be used to help understand the experimental data for the epitaxial relationship that exists when graphene is grown on a Cu(110) surface.

Understanding these moiré patterns can be done by overlaying lattices of the two layers of atoms. In figure 4.2a is a simplified example, which uses two sets of overlaid parallel lines with different spacings. The superimposed image has dark bands, with a much larger periodicity than either of the lattices. The dark bands are due to the two sets of lines interleaving and hiding the white background, and the light bands are where the two sets of lines overlap revealing more of the white background. The periodicity of the dark bands (P_D) can be calculated using the equation

$$P_D = \frac{P_1 P_2}{P_1 - P_2} \tag{4.1}$$

Taken from reference[22] where P_1 and P_2 are the periodicities, or line spacings, of the two lattices. So from the equation, it can be seen that as P_D increases, the closer together the values of P_1 and P_2 are.

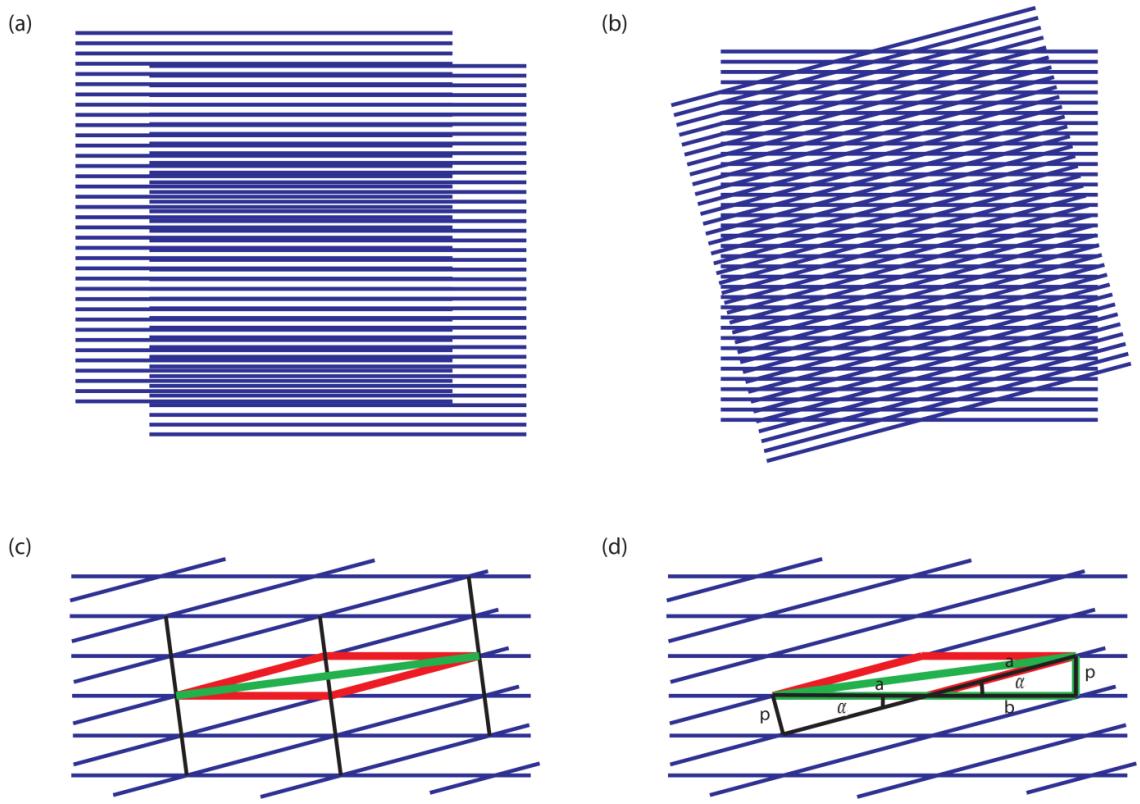

Figure 4.2

Moiré patterns produced by overlaying sets of parallel lines. In (a) the two sets of lines have different line spacing and in (b) the line spacing is the same but a rotation angle of 15° exists. (c) shows the rhombus shaped blank spaces produced by the lattices with the diagonal marked in green which is twice the moiré periodicity T_m. (d) shows the triangles used to calculate the T_m using Pythagoras' theorem.

If instead of having different line spacings, a rotation angle exists between the two lattices, then the light bands of the moiré pattern appear at the points where the two lattices cross. So unlike when the spacing is different a rotation angle exists for the moiré pattern. To calculate the moiré periodicity and the moiré angle the rhombus shaped blank spaces between the lattices need to be considered. Figure 4.2c shows an example of one of these rhombuses with the direction of the moiré lines indicated (as can be seen in figure 4.2b). This figure shows that the periodicity of this moiré pattern is half the length of the long diagonal in the rhombus (shown in green). This length can be calculated using Pythagoras' theorem, the periodicity of the lattices (p), and the rotation angle (α) between them. In figure 4.2d is the rhombus, with the triangle used for the calculation shown in green. To calculate the bottom length of the triangle, a and b need to be calculated from the smaller black triangles. Using Pythagoras' theorem; $a = p/\sin\alpha$

and $b = a\cos\alpha$. Since the length of the hypotenuse of the green triangle is twice the moiré periodicity (P_m) this length will be referred to as $2P_m$. Therefore

$$(2P_m)^2 = p^2 + (a+b)^2$$

$$(2P_m)^2 = p^2 + (a + a\cos\alpha)^2$$

$$(2P_m)^2 = p^2 + a^2(1+\cos\alpha)^2$$

since $a = p/\sin\alpha$

$$(2P_m)^2 = p^2 + \frac{p^2}{\sin^2\alpha}(1+\cos\alpha)^2$$

$$(2P_m)^2 = p^2\left(1 + \frac{(1+\cos\alpha)^2}{\sin^2\alpha}\right)$$

this can be simplified to

$$(2P_m)^2 = 2p^2\left(\frac{1+\cos\alpha}{\sin^2\alpha}\right)$$

so

$$P_m = \frac{p}{2\sin\frac{\alpha}{2}} \qquad 4.2$$

The moiré angle is calculated using the following equation

$$\alpha_m = 90 + \frac{\alpha}{2} \qquad 4.3$$

where α is the angle between the 2 lattices.

If both, a different periodicity and a rotation angle exist, then the moiré pattern becomes even more difficult to describe mathematically. Similar to the overlayed lattices with just a mismatch rotation angle, the moiré pattern is produced by pale stripes at the points where the two lattices cross. Instead of the white spaces being rhombuses they are parallelograms, and these parallelograms cannot always be used to calculate the moiré

periodicity. The example in figure 4.3a can use the parallelogram, but it is the short diagonal that needs to be calculated. This is calculated using Pythagoras' theorem, the periodicities (p_1 and p_2) and the rotation angle between the lattices (α). The angle α is the clockwise rotation that the lattice with periodicity p_1 needs to undergo to align with the lattice with periodicity p_2. This calculation is done using the equation below.

$$P_m = \sqrt{p_2^2 + \left(\frac{p_2}{tan\alpha} - \frac{p_1}{sin\alpha}\right)^2} \quad 4.4$$

Another example, shown in figure 4.3b, has the same rotation angle between the lattices but the periodicity of one of the lattices is smaller. As can be seen in the figure, the moiré periodicity is no longer described by a length of the parallelogram and so a different equation is needed. This equation is

$$P_m = \sqrt{4p_2^2 + \left(\frac{2p_2}{tan\alpha} - \frac{p_1}{sin\alpha}\right)^2} \quad 4.5$$

These are just two examples of equations to find the moiré periodicity, when a mismatch in periodicity and rotation angle exists. Not one equation can be easily found which accurately describes all examples so in section 4.3 the moiré periodicity will be measured directly from models. If the moiré periodicity (P_m) is known, then the moiré angle can be easily calculated using the following equation

$$\alpha_m = sin^{-1}\left(\frac{p}{P_m}\right) \quad 4.6$$

where the angle, α_m, is in relation to the lattice whose periodicity is used in the equation.

When thinking of graphene in terms of its carbon rings, it has 6-fold symmetry, which is the same as the hexagonal transition metal surface it is often grown on. When graphene is grown on the surface it often has its symmetry axes aligned with that of the metal, i.e. with no rotation angle present. As mentioned previously, in section 1.4, when there is a small lattice mismatch (~1%) between graphene and the metal a 1×1 relationship exists. This is because when on the metal there is actually no mismatch as the C-C bond is slightly stretched, or contracted, so that the lattice constants are the same. When there is a large lattice mismatch, this stretching of the C-C bonds to remove the mismatch would

be too great, and hence not possible, so a moiré pattern is formed. Assuming there was no change in the C-C bond length, the periodicity of the moiré pattern could be calculated using the lattice constants and equation 4.1. There is however usually a small change in the C-C bond length and this change is amplified in the variation of the moiré periodicity. So using a technique, such as STM, which allows the moiré pattern to be visualised, makes it possible for the actual lattice constant of graphene on the metal surface to be calculated. To demonstrate this the difference in the moiré superstructure for a small lattice constant increase of graphene (2.46 Å) on a Ru(0001) (2.71 Å) surface will be calculated. Using equation 4.1, the moiré periodicity is (2.71 Å × 2.46 Å)/(2.71 Å - 2.46 Å) = 26.664 Å. If the lattice constant of graphene is then increased by 1%, from 2.46 Å to 2.485 Å then the new moiré periodicity is (2.71 Å × 2.485 Å)/(2.71 Å - 2.485 Å) = 29.92 Å. This is a difference of 12%, making it significantly easier to pick up by imaging techniques, compared to the 1% increase in the graphene lattice constant.

For graphene on a transition metal surface, the moiré pattern results from the different chemical interactions which occur between the carbon atoms of graphene and the metal atoms of the surface. This interaction alters over the length of the moiré pattern, as the position of the graphene rings with respect to the surface atoms changes, until it is in the same position as it started. To think about this, we need to think about the high symmetry orientations of graphene with respect to the surface atoms. These are ring-top, -bridge and -hollow. The name refers to the position of the centre of the graphene ring with respect to the metal atoms below. For ring-top the graphene ring sits directly over the surface atom, for ring-bridge the graphene ring sits so it is bridging between two surface atoms, and for ring-hollow the graphene ring is directly over the hollow site between three surface atoms. For ring-hollow this is further split into ring-fcc and ring-hcp, which differ only in relation to the second layer of metal atoms.

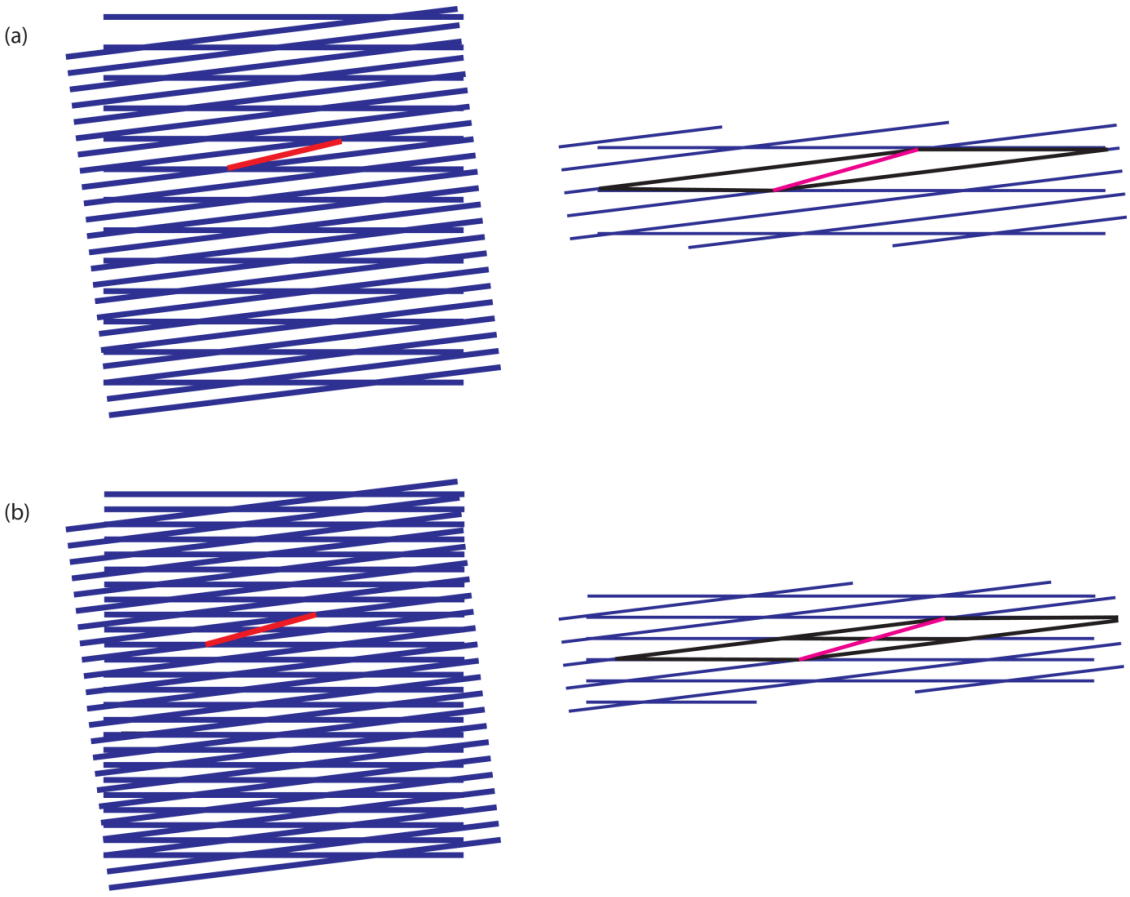

Figure 4.3

Shows on the left moiré patterns where the periodicity of the two sets of lines in the lattice are different and a rotation angle of 5° exists. (a) has a large mismatch in the periodicity and (b) a small mismatch. On the right is a close up look of the parallelograms in the lattice with the length of the moiré periodicity marked in pink.

Figure 4.4 shows an STM image of the moiré pattern that is present for graphene on Rh(111) along with a model showing the position of the graphene rings with respect to the surface.[23] The model shows the occurrence of the high symmetry orientations in the ratio top:hollow:bridge = 1:2:3. This ratio allows the model to be matched to the unit cell indicated on the STM image. It can be seen that in the corner of the unit cell is the ring-top site which has maximum tunnelling contrast implying that graphene sits highest above the surface here. The ring-bridge site, which appears halfway along each edge and in the centre of the unit cell, has minimum tunnelling contrast, implying the graphene is very close to the surface in this position. The ring-hollow sites appear in the centre of the triangles made by the ring-bridge sites, and have intermediate contrast.

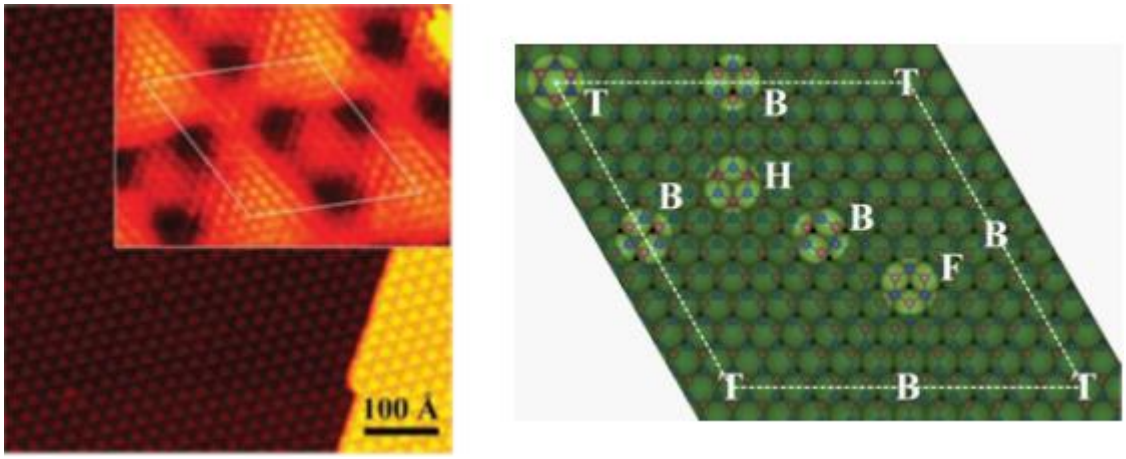

Figure 4.4

On the left is an STM image showing the moiré pattern present for graphene on Rh(111) with the inset showing a close up of the unit cell. On the right is a model detailing the positions of graphene over the surface at different points of the unit cell. Taken from reference[23]

Different moiré patterns, produced due to the lattice constant mismatch of graphene on various hexagonal metal surfaces, have been well studied, but very little has been done for metal surfaces of different symmetries. As mentioned previously, graphene growth on a copper surface is of great interest. For large scale production, the graphene will not be grown on single crystals, but on polycrystalline copper foil which can be made up of a mixture of surfaces, so it is useful to be able to understand the relationship of graphene with all the high symmetry surfaces. Most work has been carried out on Cu(111)[24] [25] [26] due to the similar symmetry to the graphene, and as expected it grows mainly in alignment with the copper surface. Even though copper is a 3d metal it has a larger lattice constant than other 3d metals such as nickel and cobalt but has a comparatively smaller one than the 4d and 5d metals. The mismatch with graphene is around 4%; this is too high to be compensated with by stretching of the C-C bonds. But since it is so much smaller than the roughly 10% mismatch with the 4d and 5d metals, it has a superstructure nearly double the size. Calculation using equation 4.1 gives a moiré periodicity of around 63 Å, which is very close to the superstructure of about 66 Å seen experimentally using STM.[24]

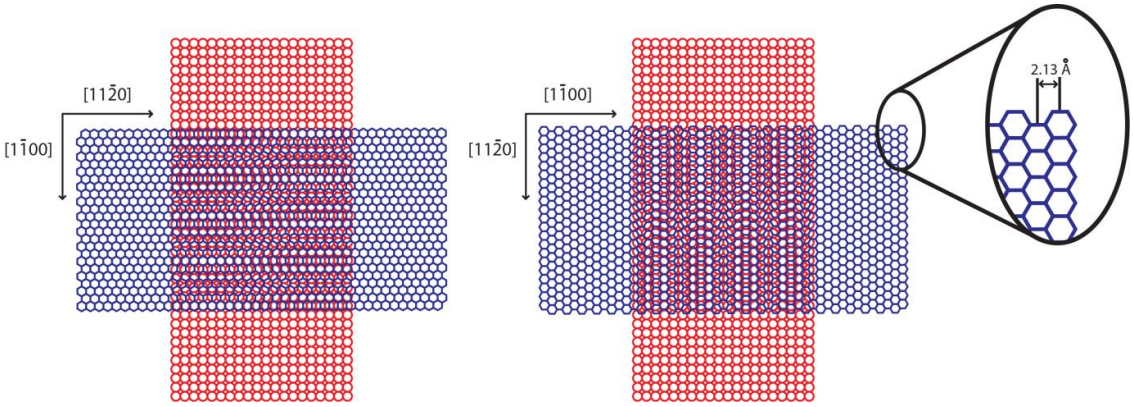

Figure 4.5

Models demonstrating how the two predominant moiré patterns for graphene on Cu(100) are produced. The zoom-in shows the distances between the rows of graphene rings.

The epitaxial relationship between graphene and the non-hexagonal surface Cu(100) has also been studied by several groups.[27] [26] [25] On this surface there are two predominant superstructures. These two superstructures are rotated by 90° with respect to each other, and are aligned to the two high symmetry directions of the copper. The two superstructures are remarkably similar, and occur as there are two symmetry equivalent ways to put the 6-fold graphene on the 4-fold Cu(100). This arrangement gives linear superstructures with a periodicity of about 11 Å (shown in figure 4.5). The reason this superstructure is so much smaller than that seen for Cu(111), despite the same metal lattice constant, is that the moiré periodicity is aligned with the $1\bar{1}00$ axis of the graphene (armchair-type edge) instead of the $1\bar{1}20$ (zigzag) (see figure 4.5). Along this direction the graphene rings are not aligned periodically, but to get from the first column to the second would be a distance of 2.13 Å. If this is plugged into equation 4.1, instead of 2.46 Å, a moiré periodicity of 12.7 Å is calculated, which is closer to the 11 Å seen experimentally.

4.1.2 Aims

In this chapter the work will focus on graphene on a Cu(110) single crystal. To my knowledge, before this work was carried out, there were no previous studies of graphene on this surface that had been reported. Section 4.2 will discuss the growth of graphene on the Cu(110), and the issues that arose when growing it in the UHV system. Section 4.3 is the results section and starts by discussing the work done by collaborators at Warwick

for graphene on copper foil. This work will describe how (n10) faceting is found to occur on the copper foil under the growing graphene. The graphene on Cu(110) will then be used as a model to help explain this and the resulting moiré pattern will be explored.

4.2 Graphene preparation

The preparation of graphene on copper is normally achieved by chemical vapour deposition (CVD) of small hydrocarbons in a tube furnace. This uses a mixture of hydrocarbon and hydrogen at pressures in the region of 500 mTorr to 1 atm and temperatures of around 1000°C. In our UHV system the maximum conditions that could be used are 1×10^{-5} mbar of the hydrocarbon, in this case ethene, at 700°C. CVD under these conditions on the Cu(110) single crystal didn't yield any graphene. Next, temperature programmed growth (TPG) was attempted, which involves depositing the ethene at room temperature then heating up. This was found to be difficult as even when the sample was exposed to 1000 langmuirs of ethene (1×10^{-6} mbar for 17 minutes) at room temperature (RT) the coverage was just 0.04 ML. Reducing the temperature of the sample down to -75°C did not increase the coverage. This shows that the sticking coefficient of ethene on the Cu(110) is, as expected, very low.

Exposure at RT and low temperature resulted in a very low coverage, and heating up the sample desorbed most of it with little sign of graphene on the surface. So in order for the graphene to be grown, thermal cycling was used, in a method similar to that used by Gao *et al.* to grow graphene on Cu(111).[24] For this, the temperature of the sample was cycled up and down between RT and 500-700°C with a background pressure between 1×10^{-6} to 1×10^{-5} mbar of ethene. The graphene coverage was found to be roughly proportional to the number of cycles, with 10 cycles being enough to yield exclusively single domain graphene islands, with sizes in the range of a few 100 nm in diameter.

The effects on graphene quality, on the copper surface, with differing temperatures and pressures were explored. For graphene grown epitaxially, a major cause for reduction in graphene quality is the introduction of domain boundaries. The domain boundaries occur due to the coalescence of graphene flakes and have been shown to scatter electrons on

the atomic scale which dramatically reduces the carrier mobility.[28] Decreasing the density of the graphene nucleation points decreases the number of domain boundaries. A study by a group in Korea found that polished copper films had a much lower density of nucleation points compared to unpolished copper films.[29] The polishing of the surface makes an important difference to the graphene domain size. For a polished sample, the average domain size during the early growth stage was ~140 μm^2, compared to just ~30 μm^2 for the unpolished sample. This indicates that graphene nucleation takes place at step edges and surface defects. Indeed, theoretical studies done by Gao *et al.* showed that nucleation at a step edge has a barrier of 2 eV lower than that on a terrace.[30]

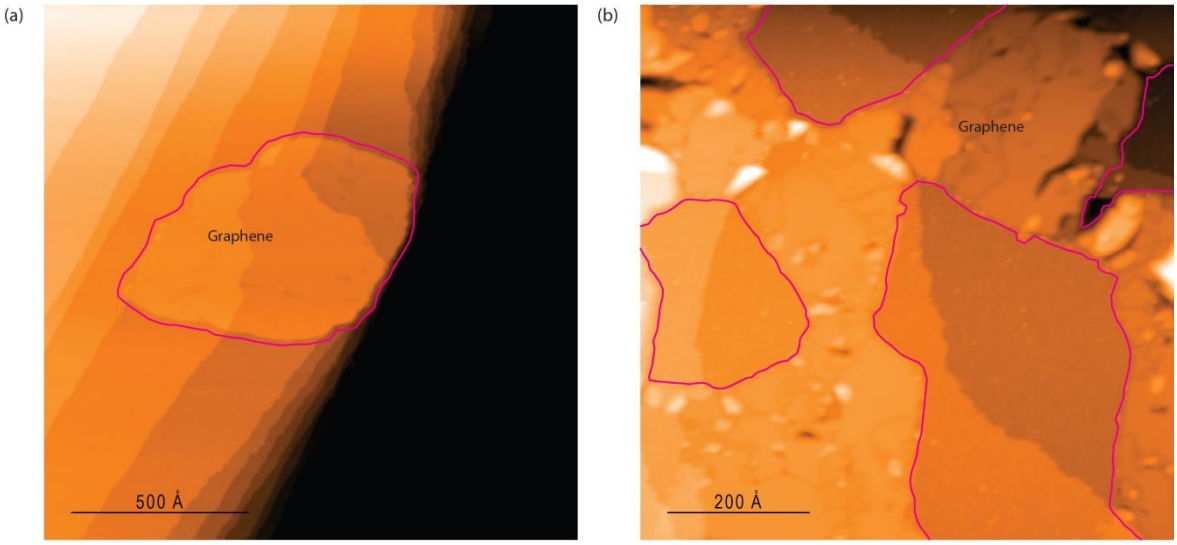

Figure 4.6

STM images of graphene grown with different background pressures of ethene. In (a) 1×10^{-6} mbar and in (b) 1×10^{-5} mbar. The images were acquired with a current of 0.08 nA, and for (a) a voltage of 0.8 V and for (b) 0.4 V. The graphene islands are outlined in pink.

The pressure of hydrocarbon used during growth can have an important effect on surface coverage and graphene quality. Figure 4.6 shows representative STM images of graphene grown on two samples whose preparation was the same apart from the ethene pressure. Both samples were prepared by 5 thermal cycles between RT and 700°C. Figure 4.6a shows graphene prepared with a pressure of 1×10^{-6} mbar of ethene, and a large solitary graphene flake can be seen. When the pressure was increased to 1×10^{-5} mbar, as in figure 4.6b, a greater surface coverage can be seen due to the higher availability of hydrocarbon. This comes at the cost of producing many separate nucleation points,

resulting in a patchwork type quality of the graphene which is made up of multiple grains all stitched together.

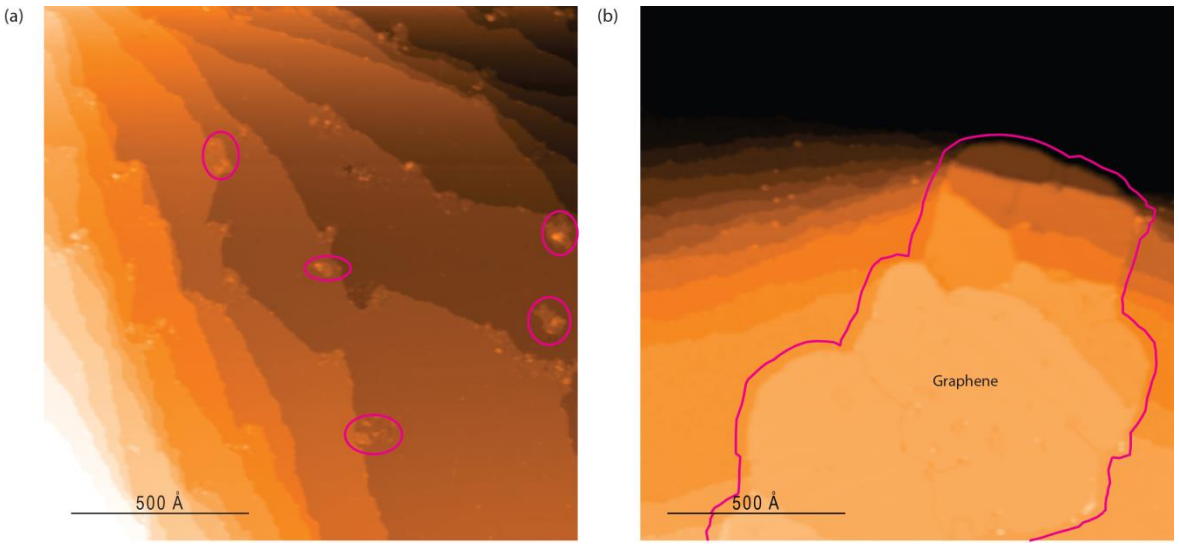

Figure 4.7

STM images of graphene grown with different maximum temperatures in the thermal cycling. In (a) 500°C and in (b) 700°C. Image (a) was acquired with a current of 0.09 nA and a voltage of 1.1 V. (b) was acquired with a current of 0.08 nA and a voltage of 0.8 V. Some of the small graphene nucleation points in (a) are circled in pink and the large graphene island in (b) is outlined in pink.

Another effect on graphene quality is the maximum temperature used during the thermal cycling. In figure 4.7 are examples of graphene grown under similar conditions, with only the maximum temperature differing. In both cases 5 thermal cycles were carried out, with a background pressure of 1×10^{-6} mbar of ethene. In figure 4.7b the maximum temperature was 700°C, and a large graphene flake of hundreds of ångstroms in diameter can be seen. With the maximum temperature lowered to 500°C (figure 4.7a), not only are no large flakes seen, but the surface is fairly bare. All that can be seen are small graphene nucleation points, mainly along the copper step edges. Any other hydrocarbon has either not adsorbed or has desorbed from the surface.

Subsequent annealing of the graphene after growth can improve the quality, by removing pollution and healing defects. In figure 4.8a is a typical image of the sample after graphene growth at a pressure of 1×10^{-5} mbar and a temperature of 600°C. The graphene is unordered and deposits of unidentified pollution can be seen. After subsequent

annealing to 600°C (figure 4.8b) and 650°C (figure 4.8c) excess material is removed, and ordering of the graphene along the step edges can be observed. These experiments show the importance of balance between temperature and pressure during growth, to enable large, good quality graphene flakes to be produced.

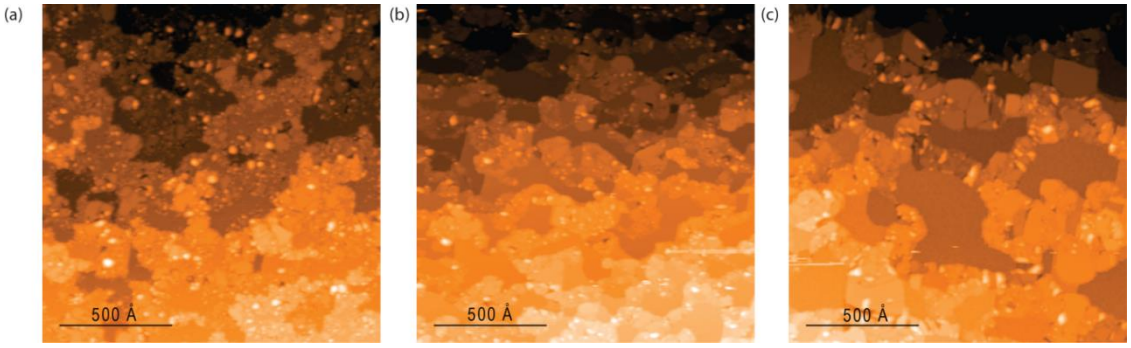

Figure 4.8

STM images after subsequent annealing. (a) was prepared by 5 thermal cycles up to 600°C with an ethene pressure of 1×10^{-5} mbar. (b) was after the sample was annealed for 10 minutes at 600°C and (c) after a further 10 minutes annealing at 650°C. These images were acquired with a current of 0.07 nA and a voltage of 0.7 V for (a-b) and 1.1 V for (c).

The reason that TPG growth does not work and thermal cycling does is unclear. It is possible that a "magic temperature" exists which is reached at one point during the cycle, when the graphene is able to form. This "magic temperature" would occur when there is the correct balance between retention time on the surface, and reactivity of the ethene molecules. The low coverage of ethene seen, even with high exposures, demonstrates the intense competition that exists between the adsorption and desorption of the ethene. As the temperature increases the retention time would decrease, but at one point the molecules might have enough energy to react with another ethene molecule before desorption occurs. It is also possible that a gradual growth occurs. With the ethene adsorbing on to the surface at RT and it mostly desorbing during annealing, but some of it forming small nucleation points on the graphene (which were observed after TPG). When the sample is cooled, more ethene adsorbs onto the surface, with some of it adding to the nucleation points and growing the graphene, with repeated cycles increasing the size of the flakes.

4.3 The epitaxial relationship between graphene and copper

This section, will explore the relationship that exists between graphene and copper. The work was done as part of a collaboration, between the University of St. Andrews and the University of Warwick, and has been published in Nano Research.[31] The first section was done at the University of Warwick and examines the relationship between graphene and polycrystalline copper foil using a variety of techniques. This produces some unexpected results that are explained in section 4.3.2, where graphene on a copper (110) single crystal is studied using STM and LEED. The work in section 4.3.2 was carried out by me at the University of St. Andrews.

4.3.1 Graphene on copper foil

Before any work with graphene began, the orientation of the clean copper foil was determined. This was done using electron backscatter diffraction (EBSD) and showed that the surface was mostly aligned close to the (100) crystallographic plane, with micro-stripes of Cu(111), about 10-50 μm across and making up less than 5% of the total surface area. To grow the graphene, the copper foil was placed in a 1 inch diameter tube furnace and heated to 1000 °C, and annealed for 20 minutes before being exposed to the methane (purity 99.95%). The exposure was for about 10 minutes but varied between 1 and 20 with a typical methane flow rate of 35 sccm. At all times there was a flow rate of 2 sccm of hydrogen (purity 99.999%) at a pressure of 6×10^{-2} mbar with a total pressure in the furnace during growth of 8×10^{-1} mbar.

With reduced growth times, a partial coverage was achieved and a faster growth rate of the graphene on Cu(111) could be observed, as previously reported.[32] Graphene islands could also be seen to cross copper grain boundaries, indicating the weak interaction between graphene and copper which has been discussed previously. After growth of the graphene to full monolayer coverage, atomic force microscopy (AFM) revealed a change in surface morphology. The surface had sharply angled corrugations which indicate interfacial restructuring, to facets of different crystallography. It is known that at the graphene growth temperatures, the copper surface is highly mobile.[33] Therefore, it is assumed that the interfacial restructuring occurs underneath the graphene, and is caused and/or stabilised by the graphene overlayer.

To try and understand the epitaxial relationship and the interfacial restructuring, low energy electron diffraction (LEED) was implemented. Due to the large copper grains (some exceeding 1 cm in lateral dimensions) present on the copper foil, LEED could be carried out on individual grains. Figure 4.9a shows a typical LEED pattern for graphene on the copper foil. In the LEED pattern, a faint ring can be seen round the edge with twelve bright spots. The annotations show that these bright spots are the results of two hexagons, with the size and symmetry of that expected for graphene. This indicated the presence of two preferred orientations of the graphene on copper, but the faint ring indicates that many other orientations (with lesser propensity) also exist, showing that the epitaxial relationship is quite weak. These two preferred orientations are at 16±1° to each other. Two preferred orientations are unexpected due to the 4-fold symmetry of the predominantly 100 type surface, which if a preferred orientation existed should result in four rather than two.

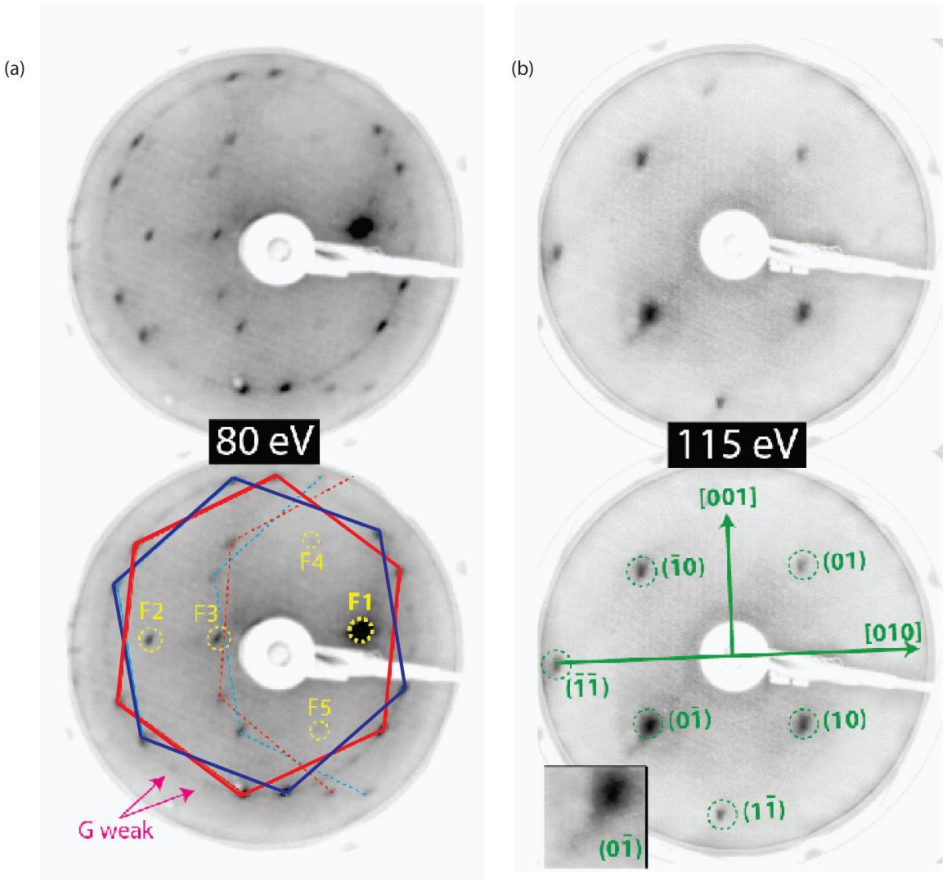

Figure 4.9

(a) is a LEED pattern of graphene on copper foil with the annotated hexagons indicating the diffraction spots of graphene and the spots marked in yellow indicating the facet spots. (b) is a LEED pattern of the copper foil after the graphene has been removed by ion bombardment.

The spots labelled F1-5 in figure 4.9a do not move with changes in beam energy, meaning they are (0,0) spots. They are the result of specular reflections of the beam, due to regions of the surface tilted, with respect to the average surface plane. These spots are quite sharp, implying that the surface tilt angles must also be well-defined, and therefore are likely to be due to faceting. The strongest facet spots, F1-3, are aligned, indicating that this is the dominant symmetry axis, and can be assigned to 210 planes. Figure 4.9b shows the LEED pattern acquired after the graphene had been removed by ion bombardment followed by gentle annealing. The LEED pattern is the expected square diffraction pattern of the 100. Therefore it appears that the growth of the graphene on the predominantly (100) type copper foil results in restructuring of the surface to n10 type facets which can then be removed after the removal of the graphene.

4.3.2 Graphene on Cu(110)

To gain some insight into the n10 type faceting, graphene was grown on a Cu(110) single crystal. To my knowledge, no work had been reported for graphene on Cu(110) before this work was carried out. The graphene was grown by CVD, to half monolayer coverage as seen by STM (data shown later), and a LEED pattern was acquired (figure 4.10). The LEED pattern revealed the expected rectangular diffraction pattern of the Cu(110) alongside two hexagons of diffraction peaks from the graphene. Like on the copper foil, there are two preferred orientations of the graphene over the copper. On the Cu(110) these are at ±5° to the [001] axis (on the copper foil these were at ±8° to the [001] axis).

Two preferred orientations of the graphene on the Cu(110) are not unexpected due to the two-fold symmetry of the (110). The cause of the ±5° rotation of the two preferred orientations is also readily apparent, as coincident LEED peaks are observed for the graphene and Cu(110). The graphene with LEED peaks highlighted in red in figure 4.10 overlap with the $(1\bar{1})$ and the $(\bar{1}1)$ peaks of the copper. The graphene with LEED peaks highlighted in blue overlap with the (11) and $(\bar{1}\bar{1})$ peaks. This demonstrates a common surface periodicity and is an example of mismatch epitaxy. Despite the difference in symmetry between graphene (hexagonal) and the Cu(110) (rectangular), the orientation of the graphene is defined by that of the Cu(110) substrate.

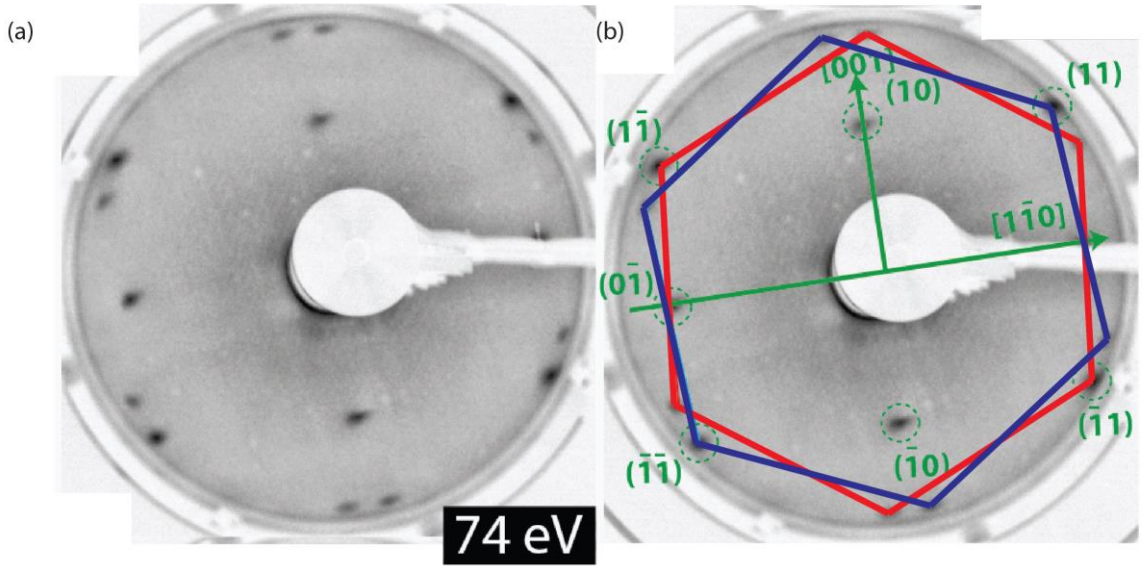

Figure 4.10

(a) shows the LEED pattern for graphene on a Cu(110) single crystal. (b) is the same LEED pattern as (a) with the addition of annotations to indicate the orientations of graphene (red and blue hexagons) and highlight the peaks related to the copper (green annotations).

The epitaxial relationship between graphene and Cu(110) was also studied by examining the moiré patterns observed using STM. Various intricately striped patterns were discerned, with one of the more common ones shown in figure 4.11a. The pattern has regions of light and dark, with stripes running in an almost vertical direction through the image. These stripes are made up of even smaller stripes going diagonally across them. To try and understand this intricate moiré pattern, model lattices were placed over the top. The direction of the Cu(110) rows are known from scanning the bare surface, so this lattice was placed first over the image. It can be seen in figure 4.11b, that the Cu(110) rows fit nicely along the small stripes in the image, with the thin black lines between the bright stripes, being between the copper rows. This indicates that this small striped part of the pattern is most likely due to an electronic effect, with a low contrast occurring due to the low density of electrons directly below the graphene between the copper rows.

As for the graphene, the rings can be seen very faintly in the dark middle region of the image. By taking a fourier transform of the image, isolating the spots related to the graphene and performing an inverse fourier transform, an image with just the graphene on can be created. By doing this, no alterations were made to the size or orientation of

the graphene, and this was just used as an aid to find the correct positioning of the graphene over the image (which can be seen in figure 4.11c). In figure 4.11d, both lattices are positioned over the image, with the [11$\bar{2}$0] direction of the graphene rotated by 5 degrees with respect to the Cu(110) rows, which is the preferred orientation as seen by the LEED. These stripes are the almost vertical stripes running down the image, and the lighter and darker regions of the image are due to the two lattices shifting in and out of alignment along these stripes, which occurs periodically over a distance of ~65 Å. Figure 4.12 shows a large model, where the regions of alignment and misalignment can be observed. Such a large distance with regions which have very good alignment of lattices and regions with a mismatch likely result in a slight rippling of the graphene over the copper.

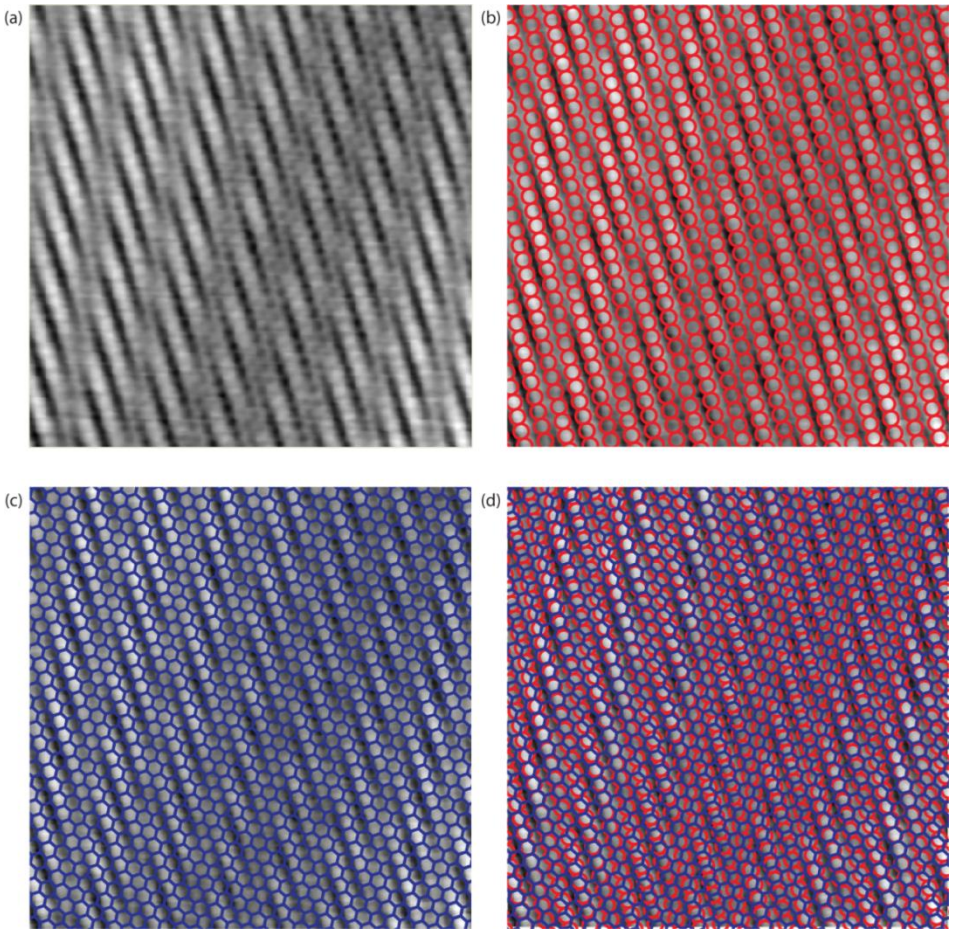

Figure 4.11

(a) is an STM image showing the moiré pattern of graphene on Cu(110) and (b), (c) and (d) are the same image which has been overlayed with model lattices to explain the moiré pattern. The image in (a) was acquired with a current of 0.2 nA and a voltage of 0.5 V.

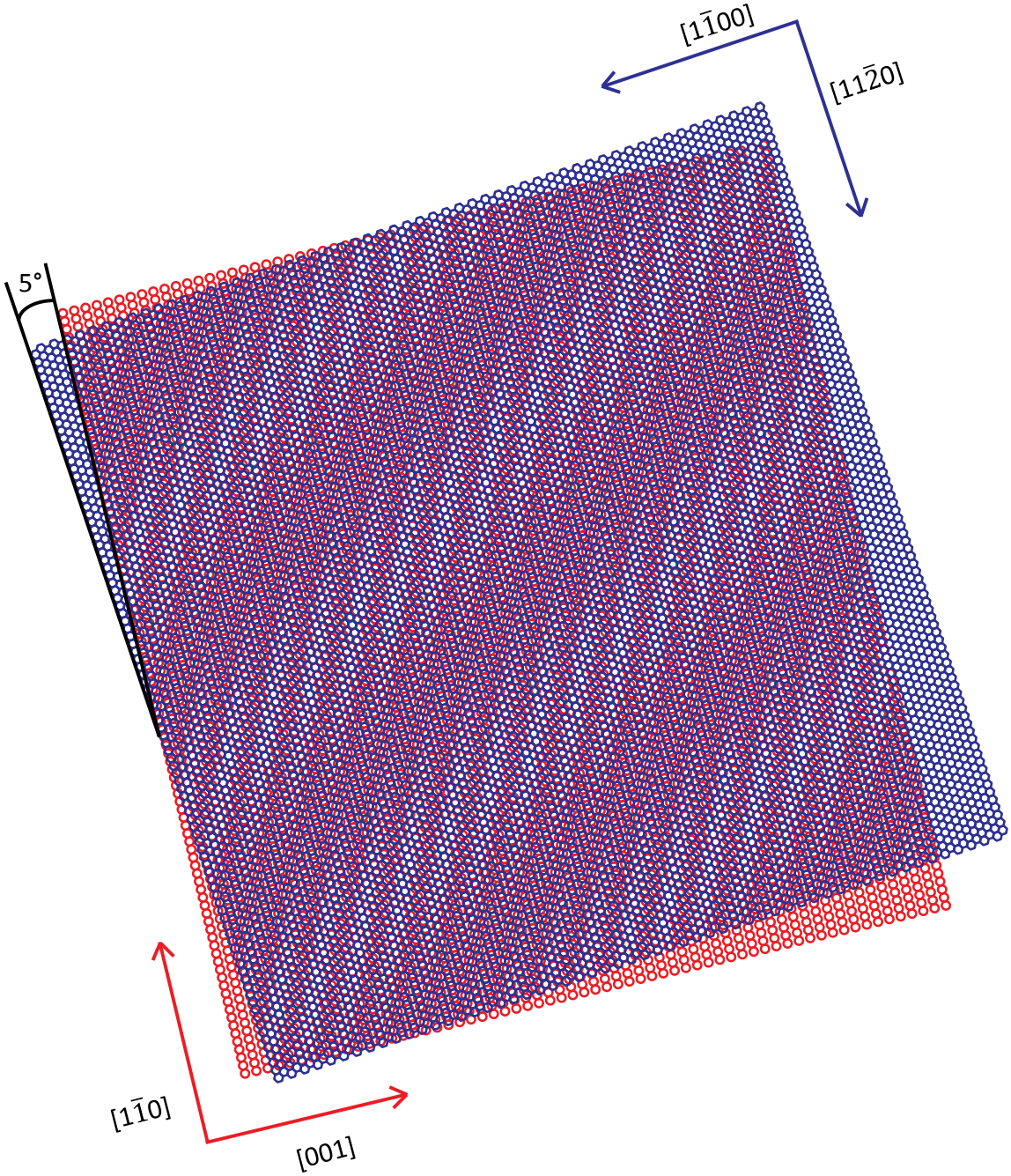

Figure 4.12

Large model showing the full extent of the moiré pattern produced for graphene over Cu(110) with large regions of alignment and misalignment between the lattices.

To further understand why this rotation occurs simple model lattices were analysed. Figure 4.13 shows two simple models of the Cu(110) rows which are spaced by 3.62 Å, overlayed with the lines representing the graphene [11$\bar{2}$0] spaced by 2.13 Å. In figure 4.13a, there is no rotation between the lattices, and every third row of the copper lattice interleaves with the graphene lattice giving a moiré periodicity of 10.86 Å. When a

rotation of 5° exists, like that seen by LEED, a similar sized moiré periodicity exists (11.1 Å) which can be seen in figure 4.13b. Just from this the reason for the preferred orientation is not obvious, but the actual lattices of copper and graphene are more complicated than these simple models. Figure 4.13c and d show more complete models of the graphene on Cu(110) system. It can be seen that when there is no rotation the moiré periodicity is actually twice what the simpler model suggested as the rows drift in and out of alignment periodically and alternating row to row. When a rotation of 5° exists the same drifting in and out of alignment also occurs but alignment remains over a much larger distance and adjacent rows are aligned. This could most likely stabilise early stage growth, and pin the graphene in this rotated orientation over the copper.

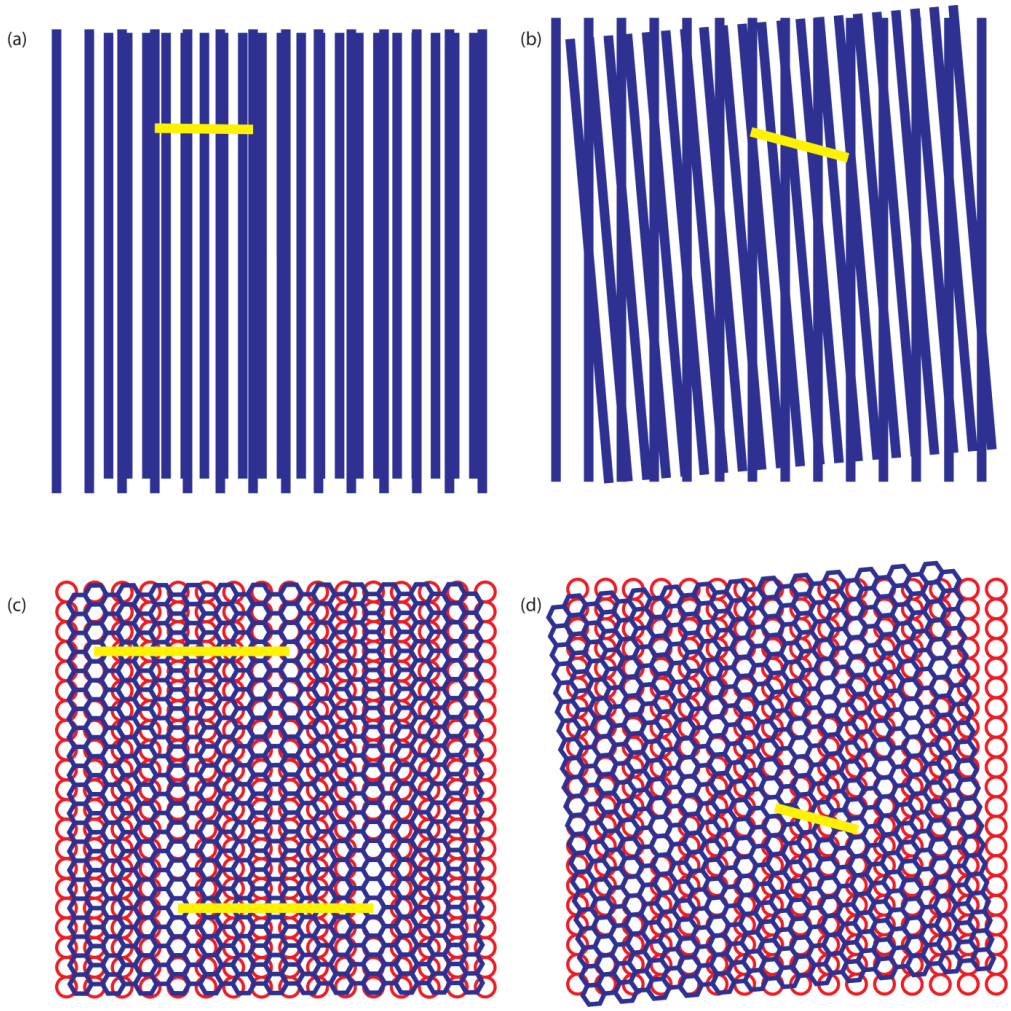

Figure 4.13

(a) and (b) are simple moiré patterns of graphene (2.13 Å) on Cu(110) (3.62Å) with (a) having no rotation between the 2 lattices and (b) having a rotation of 8°. (c) and (d) are more complete moiré patterns of graphene on Cu(110) with (c) having no rotation between the 2 lattices and (d) having a rotation of 8°. The moiré periodicities are marked in yellow.

As discussed in section 4.3.1, the copper foil underneath the graphene restructures to (210) facets, with the graphene rotated by ±8° to the [001] axis. To understand the occurrence of this rotation simple model lattices were analysed, similar to the graphene on Cu(110) system. Figure 4.14 shows two simple models of the Cu(210) rows which are spaced by 5.72 Å, overlayed with the lines representing the graphene [11$\bar{2}$0] spaced by 2.13 Å. In figure 4.14a no rotation exists between the two lattices, and it can be seen that every third row of the copper lattice interleaves with the lattice for the graphene giving a moiré periodicity of 17.2 Å. In figure 4.14b a rotation of 8° exists like that observed by LEED for the graphene on the copper foil. In this case the moiré periodicity is the same as the copper periodicity. This minimising of the moiré periodicity when a rotation angle is applied explains the reason for the preferred orientations of graphene on the (210) faceted copper foil.

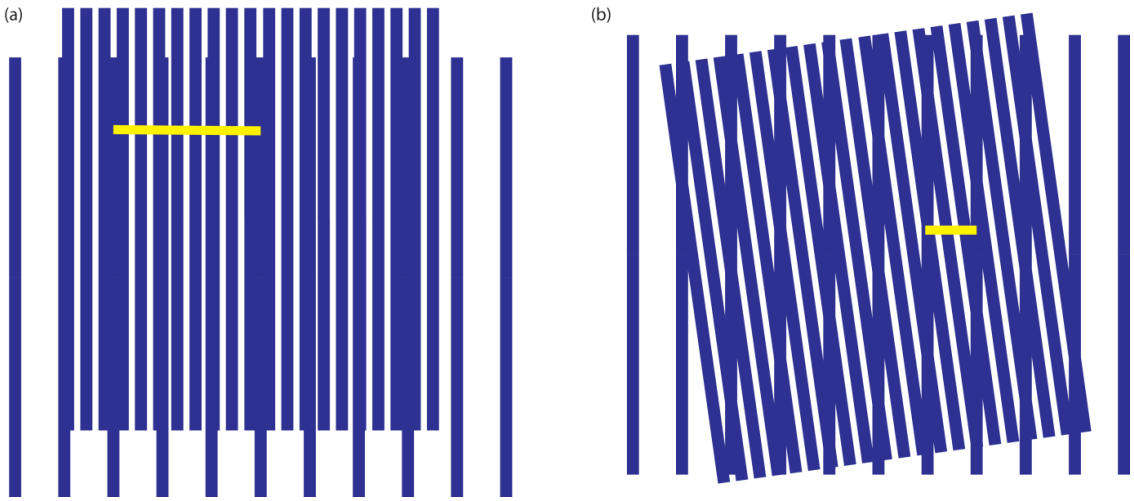

Figure 4.14

Simple moiré patterns of graphene (2.13 Å) on Cu(210) (5.72Å) with the moiré periodicity marked in yellow. (a) has no rotation between the 2 lattices and (b) has a rotation of 8°.

Returning now to the STM images of graphene on Cu(110), there was also evidence of surface restructuring of the copper beneath the graphene. In figure 4.15 is a typical STM image of a graphene flake carpeting across several copper terraces. It can be seen that the step edges of the graphene do not align with that of the copper. Also, line profiles across the graphene, reveal evidence of step edges that are double and even triple the height of others. This is not due to few layer graphene, as the apparent height of the

graphene over the copper is roughly half that of the copper step height, and no increases of half a step in height are observed. It appears that these higher steps are due to double and triple height copper steps, which are not observed on the bare surface. Further evidence of this is the narrowing of the copper terraces as they approach the graphene flake. This shows that at the graphene growth temperatures, where the copper is highly mobile, some form of restructuring of the copper is occurring under the graphene, which is stabilised by the graphene similar to the facets being stabilised on the copper foil.

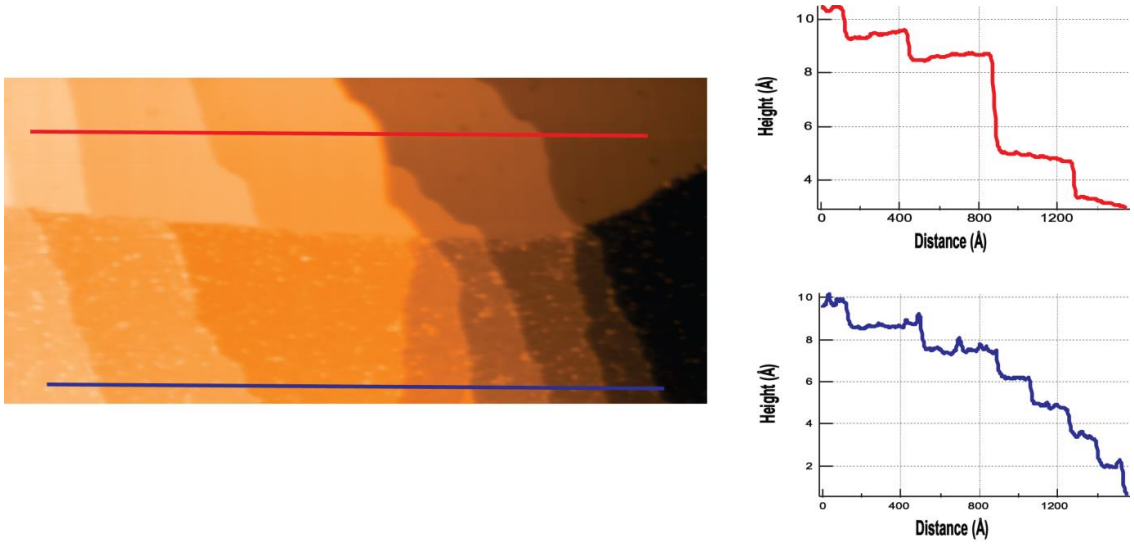

Figure 4.15

On the left is an STM image of a graphene flake (top of image) carpeting across the Cu(110) and on the right are line profiles across the graphene (top) and bare copper (bottom). The image was acquired with a current of 0.1 nA and a voltage of 1.0 V.

The interfacial restructuring, and preferred orientation of the graphene on the copper, suggest a strong interaction between the two. Studies have shown this to be untrue, and in fact a weak interaction exists.[34] [35] Indeed, when micro-spot angle resolved photo-emission spectroscopy (μARPES) was used by our collaborators at Warwick, to investigate the interaction between the graphene and copper foil, it was found to be weak. The graphene π-band could be clearly seen and the expected linear dispersion clearly resolved, with no evidence of an induced gap and only low level doping. This weak interaction between the graphene and copper makes the preferred orientations and surface interfacial restructuring unexpected. One explanation could be that the high fluidity of the copper surface during graphene growth makes the weak interaction

enough for the interfacial restructuring to occur. Another explanation could be that the interfacial interaction is stronger during nucleation and early stage growth which drives the restructuring and pins the graphene in preferred orientations. This would also make sense with the moiré pattern for graphene on Cu(110) where there is large regions of alignment and misalignment of the two lattices. One of these regions will likely have a stronger interaction than the other with the surface, and the early stage growth will pin it in this slightly rotated orientation. As it grows, there will be regions that are not favourably coordinated but it is already pinned, and too large to rotate.

4.4 Conclusion

In conclusion, copper is an important substrate for epitaxial growth of graphene, but growth in a UHV environment is difficult. This is due to the sticking probability of ethene being too low at the growth temperature for the background pressures used. In order to grow the graphene, thermal cycles were used and a balance between pressure and temperature was found to be important in producing large high quality flakes.

It is well known that a weak relationship exists between graphene and copper foil.[34] [35] Collaborators at the University of Warwick also found this to be the case when using μARPES. Despite this, LEED showed that the graphene had two preferred orientations on the copper foil, at ±8° to the [001] axis. There was also evidence of possible surface reconstruction and faceting of the copper foil under the graphene. To try and understand this, I studied epitaxial graphene on a Cu(110) single crystal. Like on the foil, LEED revealed two preferred orientations, this time at ±5° to the [001] axis. The LEED for the Cu(110) helped explain what was going on for the graphene on copper foil. It was found that coincident LEED peaks existed for the graphene and Cu(110). This demonstrated a common surface periodicity between the copper and graphene and is an example of mismatch epitaxy. Despite the difference in symmetry between graphene (hexagonal) and the Cu(110) (rectangular), the orientation of the graphene is defined by that of the Cu(110) substrate. This example of graphene growth on a single crystal substrate demonstrates how non-trivial graphene orientations can be favoured on low-symmetry

surfaces, and reveals the importance of mismatch epitaxy for graphene growth on copper foil.

Despite the copper foil being predominantly (100), after growth of the graphene it restructured to (n10) facets. The slight difference in preferred orientations, seen for the Cu(110) compared to the copper foil, is due to the (n10) facets being (210) and not (110). It seems that on the copper foil, structural feedback exists, with the graphene growth inducing and stabilising faceting of the copper surface and the facets in turn playing an important role in the graphene growth mechanism. There was also evidence of surface reconstruction of the copper single crystal underneath the graphene. With signs of double and triple height copper steps beneath the graphene, and the graphene step edges not always aligning with the adjacent copper step edges.

Despite the preferred orientations of the graphene on the copper, a weak relationship was shown to exist between the two. The highly mobile nature of the copper at the graphene growth temperatures likely assists the faceting. Also, the preferred orientations are most probably determined during nucleation and early stage growth, where it is expected that the interaction is stronger. When looking at the moiré pattern for graphene on the Cu(110), fairly large regions of alignment and misalignment were seen to exist between the lattices. These large regions are produced due to the similar periodicity that exists between the lattices in this orientation. This allows alignment between the lattices over a fairly large region before it gradually drifts out of alignment due to slight differences in the periodicity. It is likely that different strengths of interactions exist for these regions, resulting in a rippling effect. The small rotational misalignment that results in this moiré pattern, and is seen by LEED, probably exists due to the large size of these regions, which enable the graphene to be pinned in this orientation before the regions of weaker interaction are grown.

References

[1] K. Besocke, *Surface Science* **1987**, *181*, 145-153.
[2] A. Dekoster and R. A. Vansanten, *Surface Science* **1990**, *233*, 366-380.
[3] J. T. Yates Jr, P. A. Thiel and W. H. Weinberg, *Surface Science* **1979**, *84*, 427-439.
[4] S. N. Mikhailov, L. C. A. Vandenoetelaar, H. H. Brongersma and R. A. Vansanten, *Catalysis Letters* **1994**, *27*, 79-90.
[5] J. C. Shelton, H. R. Patil and J. M. Blakely, *Surface Science* **1974**, *43*, 493-520.
[6] X. Li, W. Cai, L. Colombo and R. S. Ruoff, *Nano Letters* **2009**, *9*, 4268-4272.
[7] E. C. Neyts, A. C. T. van Duin and A. Bogaerts, *Nanoscale* **2013**, *5*, 7250-7255.
[8] F. Schwierz, *Nature Nanotechnology* **2010**, *5*, 487-496.
[9] R. Cheng, J. Bai, L. Liao, H. Zhou, Y. Chen, L. Liu, Y.-C. Lin, S. Jiang, Y. Huang and X. Duan, *Proceedings of the National Academy of Sciences* **2012**.
[10] Z. Guo, R. Dong, P. S. Chakraborty, N. Lourenco, J. Palmer, Y. Hu, M. Ruan, J. Hankinson, J. Kunc, J. D. Cressler, C. Berger and W. A. de Heer, *Nano Letters* **2013**, *13*, 942-947.
[11] S.-J. Han, A. V. Garcia, O. Satoshi, K. A. Jenkins and W. Haensch, *Nature Communications* **2014**, *5,* 3086-3091.
[12] R. R. Nair, P. Blake, A. N. Grigorenko, K. S. Novoselov, T. J. Booth, T. Stauber, N. M. R. Peres and A. K. Geim, *Science* **2008**, *320*, 1308.
[13] A. Reina, H. Son, L. Jiao, B. Fan, M. S. Dresselhaus, Z. Liu and J. Kong, *Journal of Physical Chemistry C* **2008**, *112*, 17741-17744.
[14] X. Liang, B. A. Sperling, I. Calizo, G. Cheng, C. A. Hacker, Q. Zhang, Y. Obeng, K. Yan, H. Peng, Q. Li, X. Zhu, H. Yuan, A. R. H. Walker, Z. Liu, L.-m. Peng and C. A. Richter, *ACS Nano* **2011**, *5*, 9144-9153.
[15] V. Geringer, D. Subramaniam, A. K. Michel, B. Szafranek, D. Schall, A. Georgi, T. Mashoff, D. Neumaier, M. Liebmann and M. Morgenstern, *Applied Physics Letters* **2010**, *96*, 82114.
[16] Y. Ren, C. Zhu, W. Cai, H. Li, Y. Hao, Y. Wu, S. Chen, Q. Wu, R. D. Piner and R. S. Ruoff, *Nano* **2012**, *7,* 1150001.
[17] X. Li, W. Cai, I. Jung, J. An, D. Yang, A. Velamakanni, R. Piner, L. Colombo and R. S. Ruoff in *Synthesis, Characterization, and Properties of Large-Area Graphene Films*, *Vol. 19*: Y. Obeng, S. DeGendt, P. Srinivasan, D. Misra, H. Iwai, Z. Karim, D. W. Hess and H. Grebel, **2009**, pp. 41-52.
[18] S. Bae, H. Kim, Y. Lee, X. Xu, J.-S. Park, Y. Zheng, J. Balakrishnan, T. Lei, H. Ri Kim, Y. I. Song, Y.-J. Kim, K. S. Kim, B. Ozyilmaz, J.-H. Ahn, B. H. Hong and S. Iijima, *Nature Nanotechnology* **2010**, *5*, 574-578.
[19] J. Kang, S. Hwang, J. H. Kim, M. H. Kim, J. Ryu, S. J. Seo, B. H. Hong, M. K. Kim and J. B. Choi, *ACS Nano* **2012**, *6*, 5360-5365.
[20] J. Perdereau, J. P. Biberian and G. E. Rhead, *Journal of Physics F-Metal Physics* **1974**, *4*, 798-806.
[21] C. Woll, S. Chiang, R. J. Wilson and P. H. Lippel, *Physical Review B* **1989**, *39*, 7988-7991.
[22] E. Gabrielyan, **2007**.
[23] B. Wang, M. Caffio, C. Bromley, H. Fruchtl and R. Schaub, *Acs Nano* **2010**, *4*, 5773-5782.
[24] L. Gao, J. R. Guest and N. P. Guisinger, *Nano Letters* **2010**, *10*, 3512-3516.
[25] A. L. Walter, S. Nie, A. Bostwick, K. S. Kim, L. Moreschini, Y. J. Chang, D. Innocenti, K. Horn, K. F. McCarty and E. Rotenberg, *Physical Review B* **2011**, *84*, 195443.
[26] L. Zhao, K. T. Rim, H. Zhou, R. He, T. F. Heinz, A. Pinczuk, G. W. Flynn and A. N. Pasupathy, *Solid State Communications* **2011**, *151*, 509-513.
[27] H. I. Rasool, E. B. Song, M. Mecklenburg, B. C. Regan, K. L. Wang, B. H. Weiller and J. K. Gimzewski, *Journal of the American Chemical Society* **2011**, *133*, 12536-12543.
[28] P. M. Ajayan and B. I. Yakobson, *Nature Materials* **2011**, *10*, 415-417.
[29] G. H. Han, F. Guenes, J. J. Bae, E. S. Kim, S. J. Chae, H.-J. Shin, J.-Y. Choi, D. Pribat and Y. H. Lee, *Nano Letters* **2011**, *11*, 4144-4148.

[30] J. Gao, J. Yip, J. Zhao, B. I. Yakobson and F. Ding, *Journal of the American Chemical Society* **2011**, *133*, 5009-5015.
[31] N. Wilson, A. Marsden, M. Saghir, C. Bromley, R. Schaub, G. Costantini, T. White, C. Partridge, A. Barinov, P. Dudin, A. Sanchez, J. Mudd, M. Walker and G. Bell, *Nano Research* **2013**, *6*, 99-112.
[32] M. Ishihara, Y. Koga, J. Kim, K. Tsugawa and M. Hasegawa, *Materials Letters* **2011**, *65*, 2864-2867.
[33] J. M. Wofford, S. Nie, K. F. McCarty, N. C. Bartelt and O. D. Dubon, *Nano Letters* **2010**, *10*, 4890-4896.
[34] G. Giovannetti, P. A. Khomyakov, G. Brocks, V. M. Karpan, J. van den Brink and P. J. Kelly, *Physical Review Letters* **2008**, *101,* 26803.
[35] P. A. Khomyakov, G. Giovannetti, P. C. Rusu, G. Brocks, J. van den Brink and P. J. Kelly, *Physical Review B* **2009**, *79*, 195425.

Chapter 5: Growth mechanism of graphene from ethene on Rh(111)

The majority of this work was carried out by myself, at the University of St. Andrews using low temperature scanning tunnelling microscopy (LT-STM) and high resolution electron energy loss spectroscopy (HREELS). This work has been complemented by supporting contributions from Technishe Universität München (TUM) and Georgia Institute of Technology (GTech). At TUM, the group of Ulrich Heiz carried out time-resolved STM measurements using a variable temperature STM. At GTech, Uzi Landman's group performed DFT calculations.

5.1 Introduction

5.1.1 Motivations

CVD of small hydrocarbons on a hot transition metal surface is one of the most promising methods for graphene synthesis, but little is known about the growth mechanism. Current research, on improving quality of the graphene, focuses on how alterations to the growth conditions affect the final product,[1] [2] [3] without understanding the exact details of how the hydrocarbons decompose, to actually form the graphene. Understanding these details is expected to lead to improvements in growth techniques and quality of the graphene. The formation of a carbon overlayer on a metal surface from decomposition of small hydrocarbons is not always a favourable outcome. In the chemical industry, this carbon overlayer can lead to the deactivation of metal catalysts, by the blocking of the active sites. This is known as catalytic coking, and can result in increased operational costs, due to the regeneration or replacement of the poisoned catalyst. It is hoped that information on the growth mechanism could result in methods to prevent it.

The transition metal of choice for CVD of graphene is copper, for reasons discussed in section 4.1, but it is expected that the growth will proceed similarly on all transition

metals. In this investigation a Rh(111) surface was chosen due to its position on the periodic table, in the centre of the platinum group metals. All these metals are of importance in catalysis, particularly in reactions involving C-C bond forming and C-H bond breaking. These are the reactions that take place to transform small hydrocarbons to graphene. STM requires the species to stay on the surface in order to study them. The stronger bonding of carbon to rhodium, compared to copper, helps stabilise the intermediates, making it an easier system to study. Other metals in this group, suffer with competition from desorption and bulk dissolution, particularly metals such as platinum and palladium.[4] [5]

5.1.2 Previous work from literature

The early stages of small hydrocarbon adsorption and decomposition on transition metal surfaces were studied extensively in the 80's and 90's, as a model system for heterogeneous catalysis. Ethene has been observed adsorbing vertically on a variety of metal surfaces, around room temperature, in the form of ethylidyne ($\equiv CCH_3$).[6] [7] [8] In the case of ethene on Rh(111), it adsorbs molecularly onto the surface at 100 K, with its C-C bond parallel to the surface.[9] The first stage of decomposition involves the C-H bond scission to give a vinyl intermediate (CH_2CH). This is known from temperature-programmed static secondary ion mass spectrometry (TPSSIMS) data, which shows that H^+ is already increasing before any CH_3^+ is seen (which rules out hydrogenation to ethyl (CH_3CH_2) or isomerisation to ethylidene (CH_3CH) as the initial step). [10] Theoretical studies have also shown this to be the case.[11] The following step is a further dehydrogenation to vinylidene (CH_2C). This then hydrogenates to ethylidyne ($\equiv CCH_3$) which is a very stable intermediate with all routes to it being exothermic and can be easily observed.[9] [11] [12]

It is less clear what happens precisely on annealing the ethylidyne, but between 300 and 500 K there is a large loss of hydrogen, seen by temperature programmed desorption (TPD). [13] Figure 5.1 shows the TPD spectra acquired by the group of Somorjai which has been modified to show the two distinct regimes present. The first regime is between 300 and 500 K, and consists of three peaks, with the second regime between 500 and 750 K having a fairly flat profile. The first peak seen is around 350 K and accounts for the first hydrogen, which is lost from the ethene to give ethylidyne, desorbing from the surface. After the first regime, only 21-27% of the original hydrogen content remains on the

surface. Hence, the second and third peaks in the first regime most likely account for the loss of two more hydrogens from the ethene, leaving a species with a stoichiometry of C/H ≈ 2/1. HREELS was also carried out and showed peaks at about 2920-3010 cm^{-1} ν(C-H), 475 cm^{-1} ν(C-Rh), 1400 cm^{-1} ν(C-C) and 775-850 cm^{-1} γ(C-H).[9] [14] These TPD and HREELS results led to the proposal that at this temperature there are two surface species present, C_2H and CH.[9] Between 500 and 750 K the remaining hydrogen is lost gradually until only carbon remains on the surface. At this stage the surface is mainly covered in monodispersed carbon clusters of nanometer size.[15] [16] [17] These clusters were identified as 7 fused benzene rings (hereafter labelled $7C_6$), in the form of completely dehydrogenated coronene.[15] These clusters have a height of ~2 Å, whereas the hydrogenated form (coronene), has a height of ~1 Å. Finally, the clusters coalesce at higher temperatures (>750 K) to form epitaxial graphene.

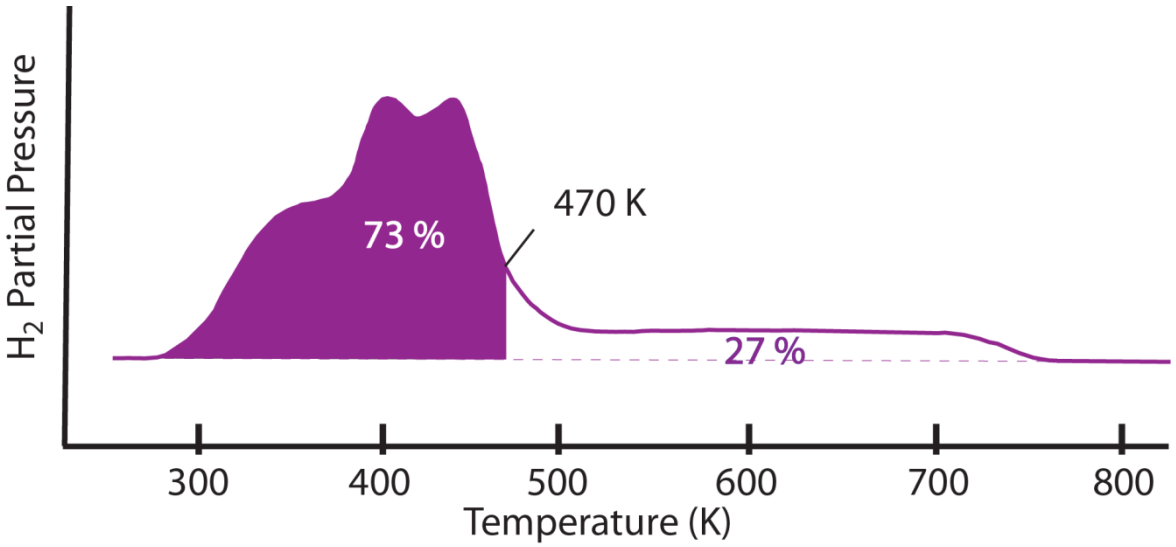

Figure 5.1

Shows hydrogen desorption from ethene on Rh(111) between the temperature range of 300 and 800 K (modified from reference[13])

5.2 Methodology

Studying the graphene growth mechanism by CVD is somewhat difficult, as the precursors, graphene, and all the intermediates between are present at once. This makes the system rather complex, and it is difficult to determine the stages involved, and the order in which they occur. The observation of CVD growth, is also not accessible on our

STM. So in order to study the mechanism, temperature programmed growth (TPG) was used. This involves depositing the feedstock, in this case ethene, at an initial temperature, then observing the surface after subsequent anneals. This allows all the sequential steps involved in the transformation of ethene to graphene to be observed separately.

For this, the rhodium surface was cleaned, as described in section 3.2.1, before ethene (99.995% purity) was exposed to the rhodium surface at room temperature (RT), for 100 seconds at a pressure of 7×10^{-8} mbar. This resulted in the formation of ethylidyne on the surface, which was observed by low temperature (~80 K) STM. The sample was then annealed sequentially to increasing temperature, with each stage observed by STM up to 970 K, where graphene was formed.

The HREELS measurements were carried out in a separate system to the STM but the sample preparation was the same. The measurements were carried out in the specular direction with an incidence and exit angle of 45°. The primary beam energy is 5 eV and the elastic peak resolution is about 50 cm^{-1}.

5.3 Results

5.3.1 Overview

In this section the whole data set will be briefly reviewed, before a detailed analysis and discussion of each stage is carried out in the subsequent sections. Figure 5.2 shows typical STM images of ethene on Rh(111) at RT and after subsequent annealing to 370 K, 470 K, 520 K, 570 K, and 670 K. At RT the ethene is observed as ethylidyne as expected at this temperature. After annealing to 370 K the ethylidyne transforms into three new surface species, of various size and electronic height. These then evolve into chains by 470 K. These chains are uniform in width and run along the main substrate directions; $[\bar{1}01]$, $[1\bar{1}0]$, and $[01\bar{1}]$. Most of the chains do not run along just one of the orientations of the substrate but have bends of 120°. After heating to 520 K these chains now appear more kinked, and after a further anneal to 570 K bright protrusions appear at the end of

the chains. These protrusions look similar to $7C_6$ (mentioned in section 5.1.2) which is seen separated from the chain at 670 K.

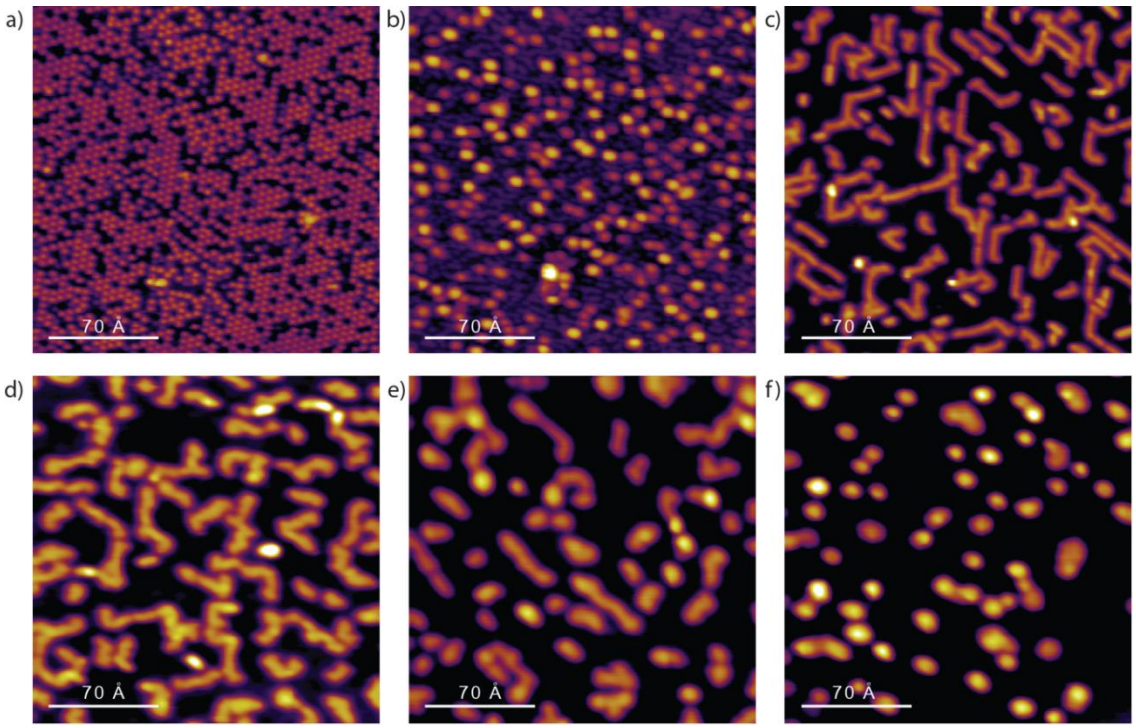

Figure 5.2

Low temperature STM images of the species present on the Rh(111) surface after ethene deposition and subsequent flash-annealing. (a) The (2×2) superstructure of ethylidyne present after RT deposition. The following images were after flash-annealing to: (b) 370 K; (c) 470 K; (d) 520 K; (e) 570 K; and (f) 670 K. All the images have the same topographic contrast and were acquired with a voltage of 0.1-1.1 V and a current of 0.1 nA.

5.3.2 Ethylidyne

Figure 5.3 shows representative STM images of ethene adsorbed on the Rh(111) at room temperature. The surface is covered in identically sized round protrusions ordered in a hexagonal arrangement. This is the well-known ethylidyne, discussed in section 5.1.2, arranged in the expected (2×2) configuration. The adsorption of ethene as ethylidyne, between the temperatures of 190 and 320 K, has been well studied, mainly by the group of Somorjai.[13] [18] This transformation was first postulated in 1978 when looking at ethene and ethyne on Pt(111) via LEED.[19] It is adsorbed in the hcp hollow sites of the Rh(111), where it is bonded strongly, resulting in a slight buckling and relaxation of the surface.[20]

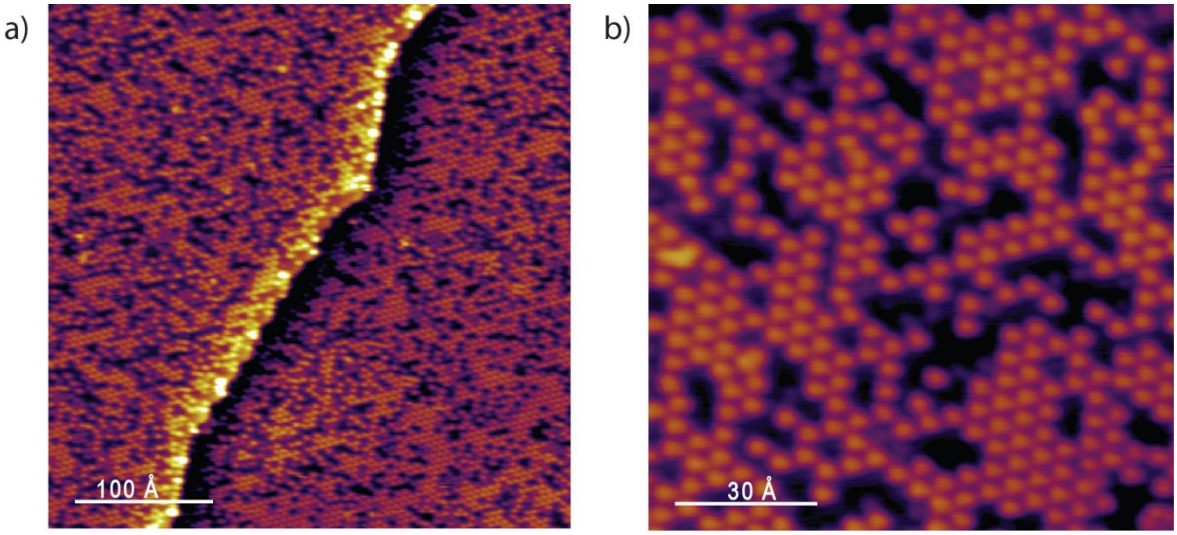

Figure 5.3

STM images of the rhodium surface after RT deposition of ethene in the form of ethylidyne. Images were acquired with a current of 0.1 nA and voltages of 1.1 V for (a) and 0.3 V for (b).

In order to further verify the assignments made in this chapter, HREELS was carried out on the system at the various anneal temperatures observed by STM. The early stages of ethene decomposition were studied by the group of Somorjai, using vibrational spectroscopy, in the early 1980s.[14] Despite this, no structural identification of the intermediate species, at temperatures above 330 K, have been reported to date. Figure 5.4 shows the HREEL spectra for the ethene upon deposition at RT, where several energy loss peaks can be observed. At 425 cm^{-1} is the Rh-C stretch. There are also two weak peaks at 955 and 1100 cm^{-1} due to a weak C-C bend and a symmetric C-C stretch, respectively. The main peak is at 1325 cm^{-1} with a smaller peak at 1405 cm^{-1} and these are the symmetric and asymmetric methyl deformations (umbrella modes). The final peak is at 2885 cm^{-1} and is from an sp^3 hybridised C-H stretch. This spectrum is consistent to those reported previously[21] [13] and well matched to the adsorption of ethene in the form of ethylidyne.

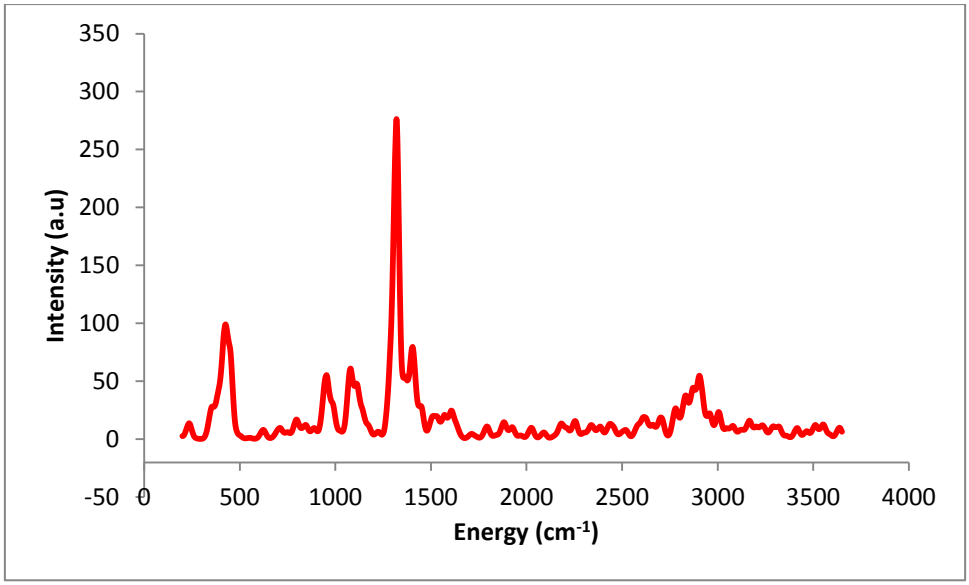

Figure 5.4

HREEL spectrum of ethene upon RT deposition on Rh(111)

5.3.3 One-dimensional polyaromatic hydrocarbons

After annealing to 370 K a variety of surface species are present on the surface. These species are involved in the formation of the chains seen at 470 K, with the identity of the species more easily understood if the nature of the chains is first known. So, in this section the chains observed at 470 K will be discussed, and the stage at 370 K will be examined in section 5.3.4.

The decomposition of ethene has been previously studied at 470 K, using a variety of techniques,[21] [14] [22] but the spectra were too complicated to make a definitive assignment. For the first time, we have managed to directly view the system at this temperature using STM. This has allowed us to observe the chains (see fig 5.5a and b for STM images) and identify them as one-dimensional polyaromatic hydrocarbons (1D-PAHs), with a model shown in figure 5.5c. This assignment is based on the appearance of the chains, and is consistent with the findings from previous studies using other techniques. In figure 5.5d the chain has good resolution, and a longitudinal periodicity of ~2.5 Å can be observed. This is consistent with the width of edge-connected benzene units. The width of the chains is also consistent with that of a benzene molecule (this time the distance between carbon atoms opposite each other in the ring). It is also

comparable, in width and electronic height, to tetracene, which is effectively a four unit long 1D-PAH (figure 5.5e).

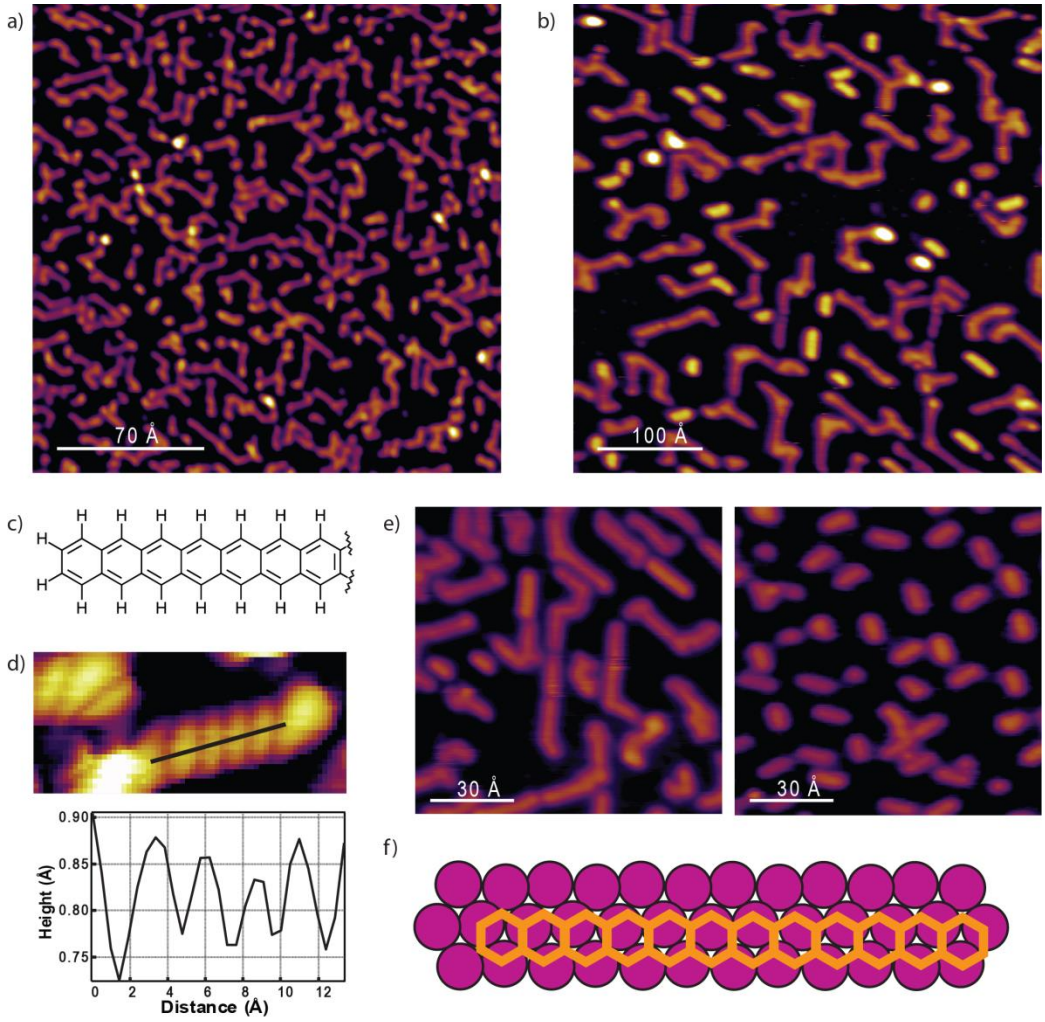

Figure 5.5

(a-b) show STM images of the 1D-PAHs which are seen on the rhodium surface after deposition of ethene and subsequent anneal to 470 K. Images were acquired with a current of 0.1 nA and voltages of 0.13 V for (a) and 0.26 V for (b). (c) depicts a model of the proposed 1D-PAHs. (d) is an STM image of one of the chains where the longitudinal periodicity can be observed with the line profile below showing it to be ~2.5 Å. (e) has 2 STM images with the same topographic contrast to compare the width of the 1D-PAHs (left) to the tetracene (right). Both images were acquired with a voltage of 1.1 V and a current of 0.1 nA. (f) is a model showing the variety of favourable bridge-type and hollow-type sites the 1D-PAHs could pass over for the graphene moiré periodicity of ~3 nm.

The next evidence for the 1D-PAHs, comes from the stoichiometry, which was calculated from previous TPD studies of ethene on Rh(111).[9] [13] These showed that after heating to ~470 K only 21-27% of the original hydrogen content remained, meaning that for roughly every two carbon atoms there is just one hydrogen atom. For our proposed 1D-PAHs, assuming they are fully hydrogenated, the central part of the chains would have a unit

cell of C_4H_2. If we include the atoms at the ends of the chains we have a structure of $C_{4n+2}H_{2n+4}$ where n is the number of rings (see figure 5.6). For chains with more than five carbon rings there will be 25-32% of the original hydrogen content remaining. This is slightly higher than the hydrogen content from the TPD results but the theoretical value assumes that the chains are fully hydrogenated. However, looking at the STM images of the chains, it can be seen that some chains, or portions of chains, appear brighter indicating that some further dehydrogenation may have occurred. The electronic height of these brighter portions is not as high as the fully dehydrogenated clusters (~2 Å) but is noticeably higher than the height of the other chains and the tetracene (~1 Å) (refer to section 5.1.2). This suggests that partial dehydrogenation has taken place.

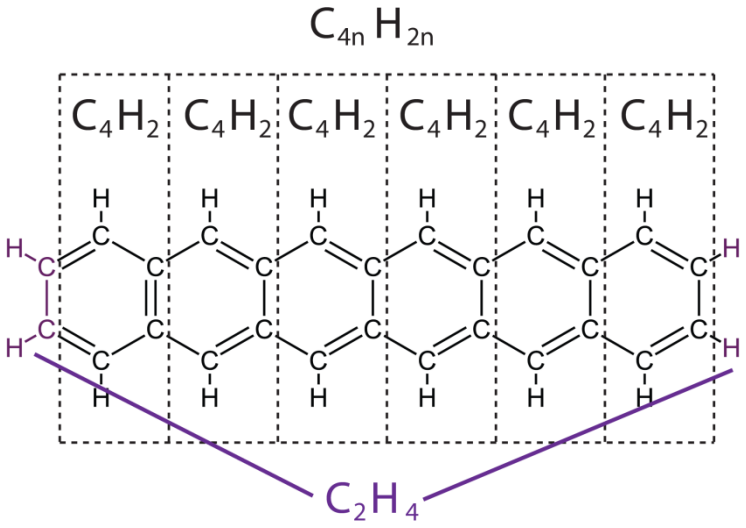

Figure 5.6

Diagram explaining how the chemical formula for the 1D-PAHs are derived.

Other previous studies also support the idea of 1D-PAHs. The broadening and weakening of the v(C-C) peak in HREELS[23] that coincides with the loss in hydrogen suggests that the intermediates are a result of polymerisation and that the C-C bonds are lying parallel to the metal substrate. X-ray photoelectron spectroscopy (XPS) data[22] reveals a narrow C1s peak. This suggests that the carbon atoms in these intermediates are in a more similar environment than that seen at RT where the ethylidyne is in a vertical orientation. This all coincides with 1D-PAHs, which have all the carbon atoms in an aromatic environment and lying flat on the surface.

In the chains, there is no continuous straight segment that is longer than 3 nm. In all cases, the chain either stops or forms a 120° kink. This 3 nm distance is the same as the length of the graphene moiré periodicity on Rh(111).[24] This moiré periodicity is comprised of twelve graphene rings on eleven substrate atoms. It is not possible from the STM images to see if a specific site is responsible for the kinking. It is obvious that there is an interaction between the chains and the surface due to the maximum length being related to the moiré periodicity of the graphene. The kinks probably stabilise the chain which has a lot of stress in it due to the different interactions at different sites causing rippling. Further evidence of the interaction comes from the fact that the 1D-PAHs follow the high symmetry directions of the rhodium.

From a previous study of graphene on Rh(111), it is known that the bridge site is the most favourable with a strong interaction between the graphene and the surface at this site.[24] There is also an attractive interaction at the hollow sites but the top site was found to have a repulsive interaction. For smaller aromatic systems, such as benzene,[23] $7C_6$,[15] coronene,[15] anthracene,[25] and naphthalene,[25] the bridge site and/or the hollow site were found to be the most favourable. It is likely, therefore, that the 1D-PAHs occur on both the bridge and hollow sites, with the unfavourable top sites avoided. Indeed, if the ring at the beginning of the chain starts off on a hollow site, then the following rings will pass over a plethora of bridge-type and hollow-type sites before returning to a similar hollow site as at the beginning. A model of this is shown in figure 5.5f which depicts 12 aromatic rings in a chain over the surface atoms.

HREELS data around this temperature is consistent with the presence of 1D aromatic chains. Despite previous vibrational spectroscopy studies, no structural identification of the intermediate species at temperatures above 330 K have been reported to date. This is not surprising when considering that the microscopically simple 1D-PAHs, have a variety of C/Rh adsorption registries, due to the 7-8% difference in the lattice parameter of Rh(111) (2.69 Å) compared to the periodicity of the edge-connected C_6 rings (~2.5 Å). This results in variation in the local coordination environment along the length of the chain, which causes difficulty in interpreting the HREEL spectrum.

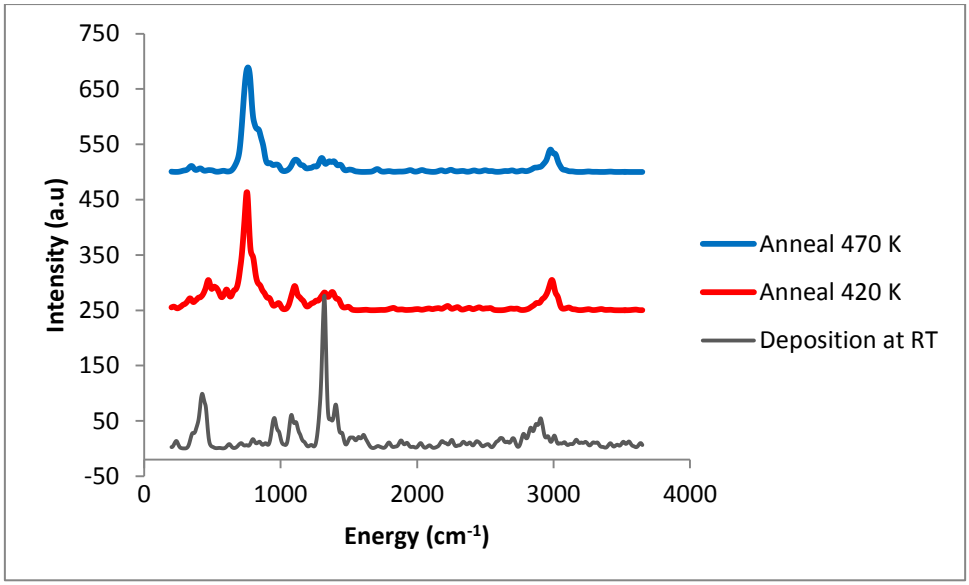

Figure 5.7

HREEL spectrums of ethene after RT deposition on Rh(111) and subsequent anneals to 420 and 470 K.

The HREEL spectrum after flash annealing to 420 K (red curve in figure 5.7), shows a large change, compared to RT. There are two main changes, with the first being the appearance of a large peak at 755 cm^{-1} which develops two distinct shoulders at 795 and 845 cm^{-1}; these are attributed to three distinct C-H out-of-plane bending modes belonging to aromatic structures.[26] The second, is a dramatic decrease in the two peaks relating to the CH_3 umbrella mode, with the symmetric component decreasing much faster than the asymmetric one. There is also a slight shift of the Rh-C stretch to ~470 cm^{-1} and the C-C bend at ~950 cm^{-1} decreases in intensity. There is an increase in the aromatic component of the C-H stretch at 2995 cm^{-1}, with just a small shoulder for the aliphatic stretch at 2885 cm^{-1}. These changes are all consistent with the vast majority of ethylidyne being converted into aromatic structures.

After flash annealing to 470 K (blue curve in figure 5.7), there is a complete quenching of the Rh—C stretch. The rest of the spectrum is very similar to that seen at 420 K but with slightly decreased intensity of the peaks. The peak representing the C-H out-of-plane modes is still resolved in a triplet with maximum at about 760 cm^{-1} and two shoulders at 800 and 840 cm^{-1}. There is a slight decrease in the C-C bending and stretching vibrations, as well as the C-H stretch.

5.3.4 Formation of 1D-PAHs

Section 5.3.3 concluded that at 470 K 1D-PAHs exist on the Rh(111) surface, in this section the formation of these chains will be examined. At the stage preceding the chains, at 370 K, three species are seen on the surface by STM (see figure 5.8). The first species is small with a low electronic height and is assigned to hydrogen. The other two species are larger in appearance. There is a lower one with a similar electronic height to the chains (1.0 Å) and a higher one with an electronic height of 1.4 Å. These species are intermediates involved in the formation of the 1D-PAHs.

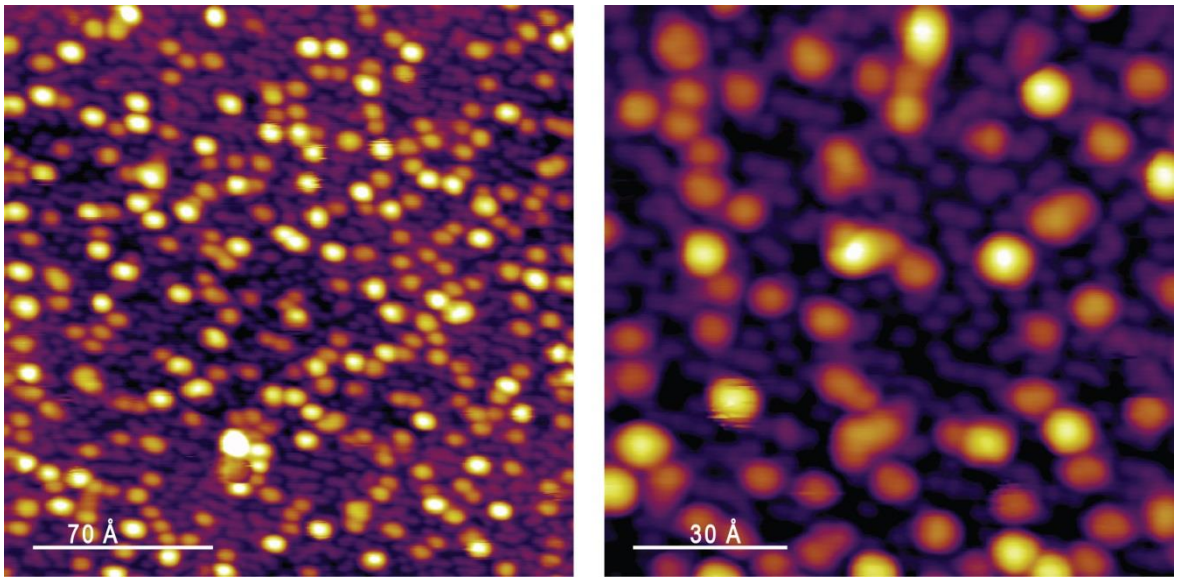

Figure 5.8

STM images of the intermediates involved in the formation 1D-PAHs which are seen on the rhodium surface after deposition of ethene and subsequent anneal to 370 K. Both STM images were acquired with a current of 0.1 nA and a voltage of 0.12 V.

Collaborators at TUM examined the chain formation using high temperature STM. For this a Rh(111) sample was held at 420 K while it was exposed to ethene, at a pressure between 2×10^{-9} and 1×10^{-8} mbar. A series of STM images were then taken in quick succession, to give a video of chain formation. A selection of images from this video are shown in figure 5.9. The video shows the growing 1D-PAHs, along with streaks that appear randomly in the images. These streaks are an indication of the presence of mobile species that are imaged incompletely due to their surface diffusivity being high, compared to the time scale of the acquisition of the STM image. Since the streaks are the

only observed species aside from the chains, then they are most likely involved in the growth of the chains by some sort of addition reaction. The height of these streaks is measured as 1.4 Å, the same as the larger species observed in the LT-STM images. This implies that this species is the mobile intermediate involved in the growth of the chains.

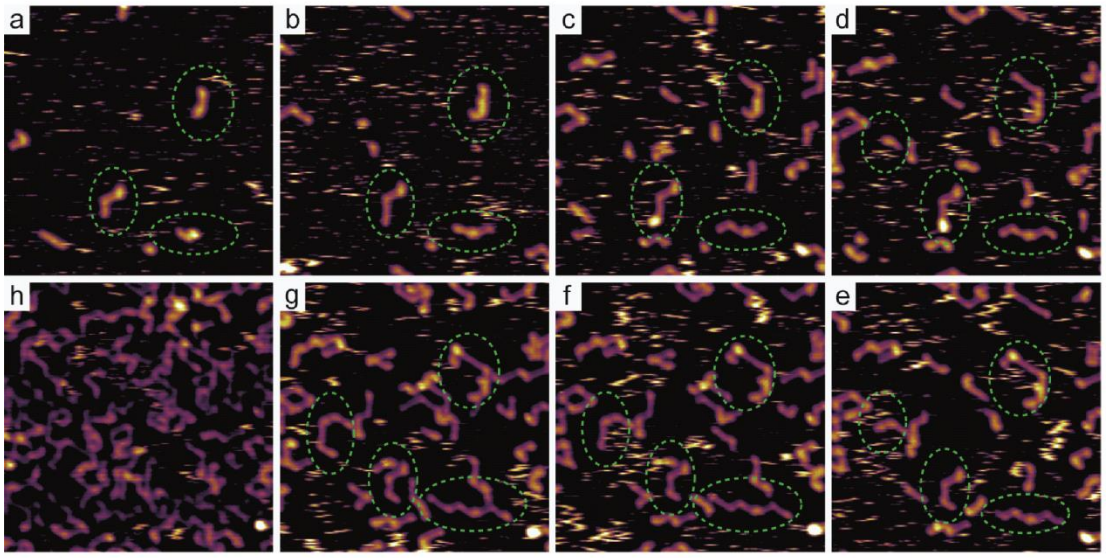

Figure 5.9

Shows a series of sequential STM images depicting the growth of 1D-PAHs from ethene on Rh(111). The ethene was dosed throughout scanning at a pressure between 2×10^{-9} and 1×10^{-8} mbar. All images are 30 × 30 nm^2 and were acquired with a voltage of -1.0 V and a current of 0.1 nA. The time steps between images were: (a-b) 15 mins; (b-c) 8 mins; (c-d) 2 mins; (d-e) 16 mins; (e-f) 31 mins; (f-g) 9 mins; and (g-h) 148 mins.

In these images the chains can be seen to grow in length and new chains form until most of the surface is covered. At the beginning of the chain formation, when the chains are quite short, they have some mobility on the surface, but become more stabilised as the chain grows. The growth of the chains occurs only at the ends of the chain with no branching observed. The only evidence of break-up at the end of chains occurs shortly after growth at that end of the chain. With no break-up observed for more established chains. There is no evidence seen of chains coalescing together, indicating a repulsive interaction and/or steric hindrance between chains. Indeed the formation of the 120° kinks often occurs to avoid two growing chains colliding. Once the 120° kinks are formed the chains become immobile and the chain growth is slowed. This suggests that the kinks are the site of strongest bonding to the surface.

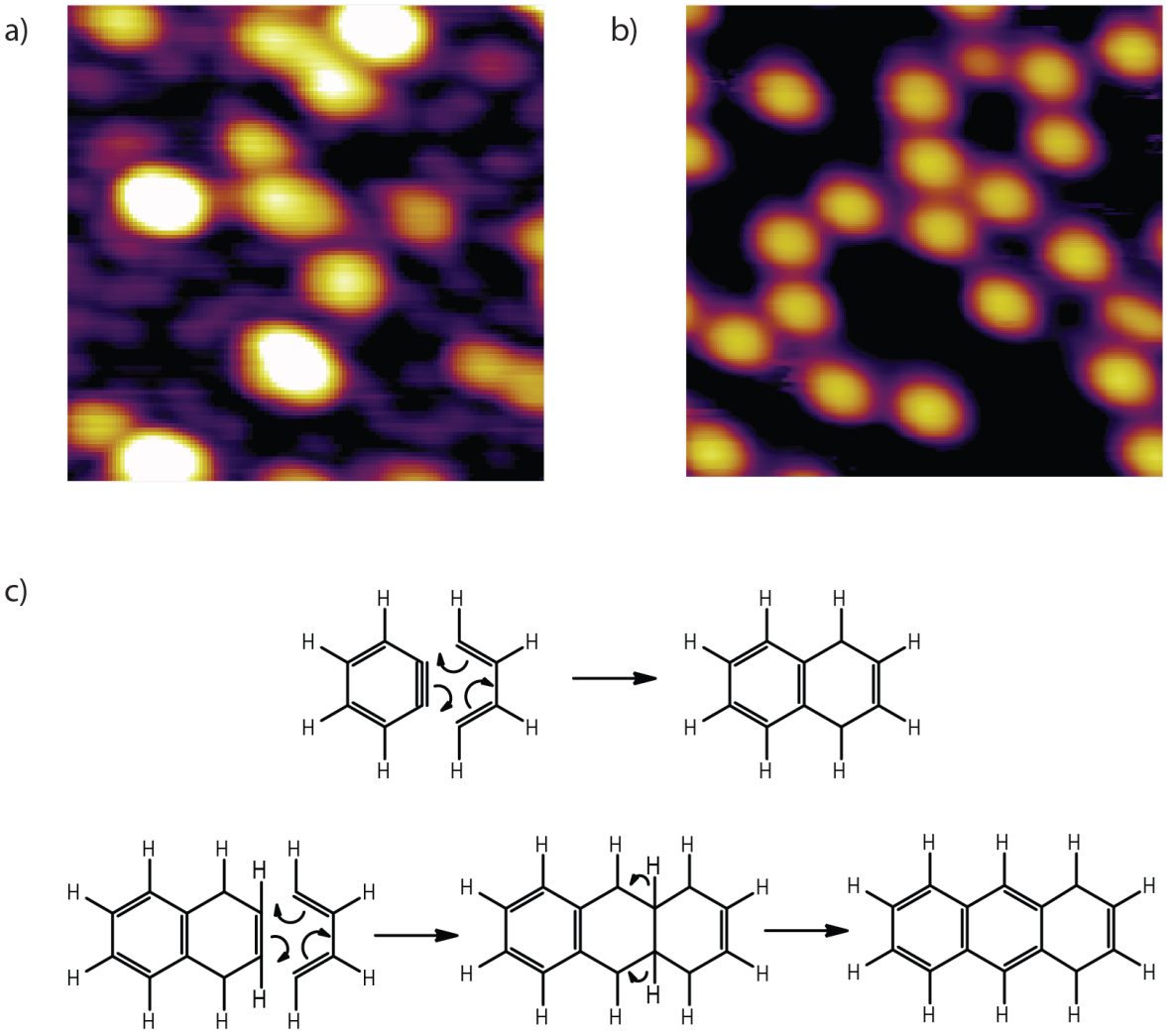

Figure 5.10

(a) shows an STM image of the ethene on the Rh(111) surface after annealing to 370 K. The medium sized species can be seen to be comparable in size to the benzene shown in (b). Both images have the same topographic contrast and have a size of 50 x 50 Å. The image parameters for (a) are 0.1 nA and 0.1 V, and for (b) are 0.1 nA and 0.4 V. (c) shows the proposed model for chain formation involving a Diels-Alder type addition of the C_4 metallocycle to a possible hydrogen deficient benzene-type molecule.

Returning to the LT STM images, the two larger species can be assigned to a benzene-type species and C_4 metallocycle. These species would have a roughly 1:1 ratio of carbon to hydrogen, which is consistent with the TPD at this temperature. To corroborate the assignment of a benzene-type species, benzene was exposed to the clean rhodium surface at RT. This is shown in figure 5.10b, and when compared to the ethene at 370 K (figure 5.10a) a similar topographic appearance is observed for the lower of the two larger species present. This is assigned to a benzene-type species, rather than benzene, as

benzene is too unreactive towards further polymerisation, as shown by Ormerod *et al.* on palladium.[27] It is likely that this C_6 species is hydrogen deficient or not fully aromatic.

The cyclotrimerisation of ethyne (C_2H_2) to benzene has been well studied on a variety of metal surfaces.[28] [29] Lambert and Ormerod proposed the reaction to proceed via C_2 coupling to give a C_4 metallocycle, followed by the addition of a third C_2 to give benzene.[30] This C_4 metallocycle was identified as the surface coordinated μ-but-2-en-1,4-diylidene. Investigation using NEXAFS revealed the molecular plane to be tilted by 35° with respect to the surface.[31] This tilt angle, along with a tip-induced lifting, has been shown by DFT calculations at GTech to result in the higher appearance of this C_4H_4 species, compared to the benzene. The proposed mechanism for the 1D-PAHs growth is shown in figure 5.10c. This involves cyclotrimerisation to form a benzene-type species (chain seed), followed by sequential surface-assisted Diels-Alder-type cycloadditions of C_4H_4. It is expected that aromatisation occurs due to loss of hydrogen at the point where the two rings join. The break up at the end of some of the chains, seen in the video, is likely some reverse Diels-Alder type reactions that occur before aromatisation is complete.

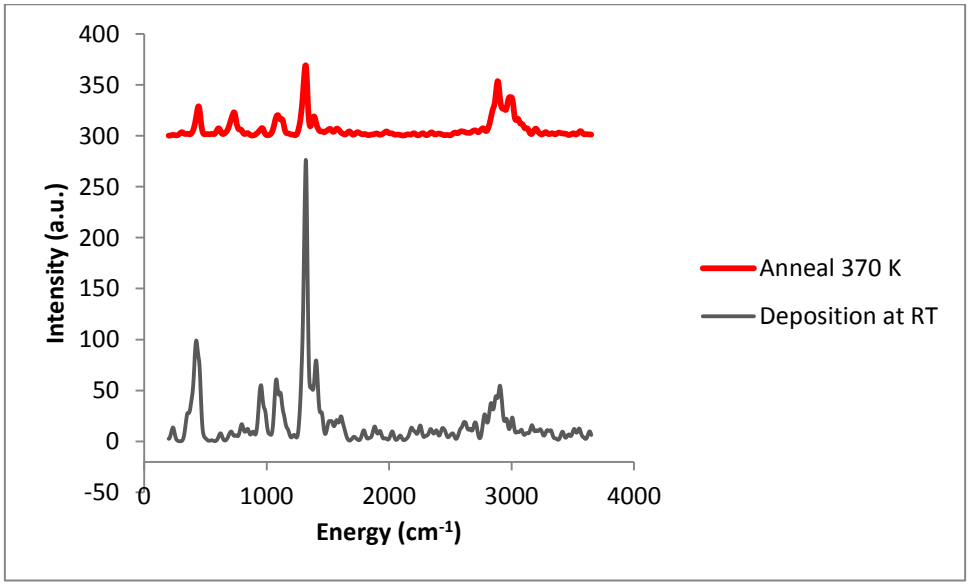

Figure 5.11

HREEL spectrums of ethene after RT deposition on Rh(111) and subsequent anneal to 370 K.

At this temperature we also see the first change in the HREEL spectra (red curve in figure 5.11), which is consistent with the formation of these intermediates. The first change is a decrease in intensity of the Rh-C stretch and a shift to ~445 cm^{-1}. There is also the first appearance of a peak at 735 cm^{-1}, with a weak shoulder at 785 cm^{-1} which is attributed to an edge C-H out-of-plane mode, belonging to aromatic structures.[26] The peaks relating to the C-C bend, C-C stretch, and the umbrella modes, all decrease in intensity. Finally, a doublet first occurs in the C-H stretching region with maxima at 2880 (aliphatic) and 2995 cm^{-1} (aromatic). This is all indicative of the commencement of a conversion of ethylidyne into aromatic structures with the presence of a weaker and shifted Rh-C stretch being attributed to the C_4 metallocycles.

5.3.5 Kinking of the 1D-PAHs

Upon heating the 1D-PAHs to 520 K, the chains are less straight and have a thicker appearance (see figure 5.12). It is expected, as justified below, that the thickening is a result of kinks occurring in the chains, as shown in figure 5.13a-d. The kinking of these chains can be explained using Clar's rule for aromaticity.[32] Clar's rule states that the degree of aromaticity, in polyaromatic hydrocarbons (PAH), depends on the resonance structure with the highest number of disjoint aromatic π-sextets present. In a straight chained PAH, such as anthracene, only one π-sextet exists, this π-sextet can be positioned anywhere along the chain but it is not possible to position more than one π-sextet. In the case of phenanthrene, made up of three aromatic rings, like anthracene but with a kink present, it is possible for two π-sextets to be present (one at each end of the chain). Since anthracene can only have one π-sextet, and phenanthrene can have two, then phenanthrene has a greater degree of aromaticity. This greater degree of aromaticity, results in a higher degree of stability of the molecule in the gas phase. This greater degree of aromaticity also reduces the reactivity on the surface, as is observed for the decreased rate of chain growth, seen previously, after the introduction of a kink.

At 470 K the growth of 1D-PAHs is kinetically driven and it is only upon annealing to 520 K that the chains are provided with enough energy to transform to the thermodynamically favoured kinked chain. These kinked chains, like the 1D-PAHs, are aligned along the three main symmetry directions of the rhodium substrate. This transformation to kinked chains occurs without a loss in chain density, ruling out coalescence of the 1D-PAHs. An

apparent shortening of the chains by around 25% occurs, which is consistent with the introduction of kinks. The structural rearrangement of the chain, to form a kink, can occur via the breaking of a single C-C bond leaving the rest of the carbon backbone intact (figure 5.13e).

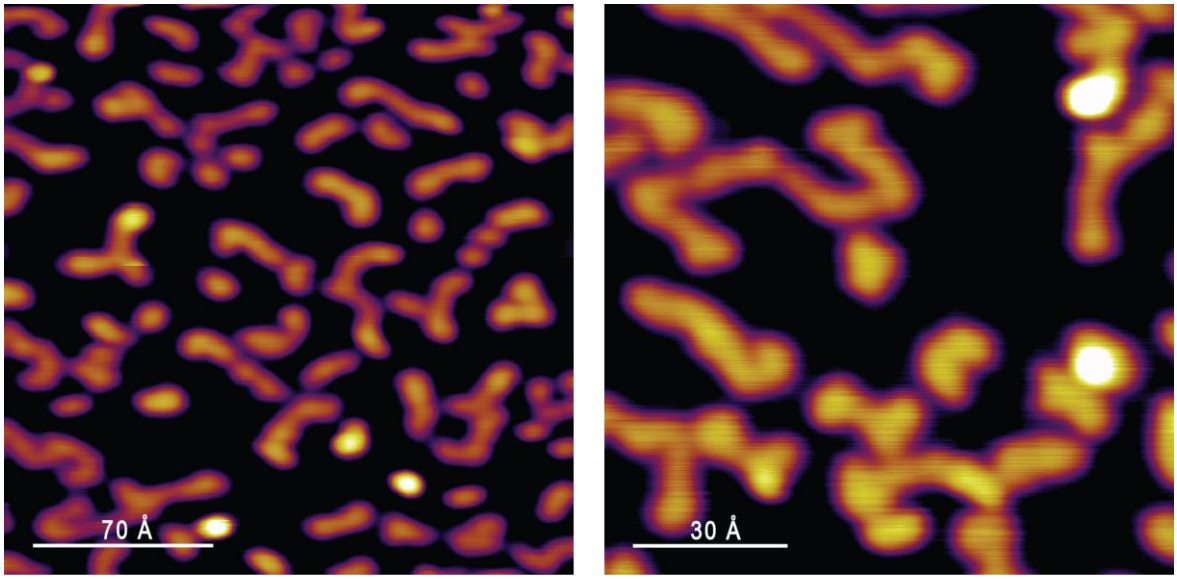

Figure 5.12

STM images of the kinked chains present on the rhodium surface after deposition of ethene and subsequent anneal to 520 K. Images were acquired with a current of 0.1 nA and voltages of 0.67 V for the image on the left and 0.15 V for the image on the right.

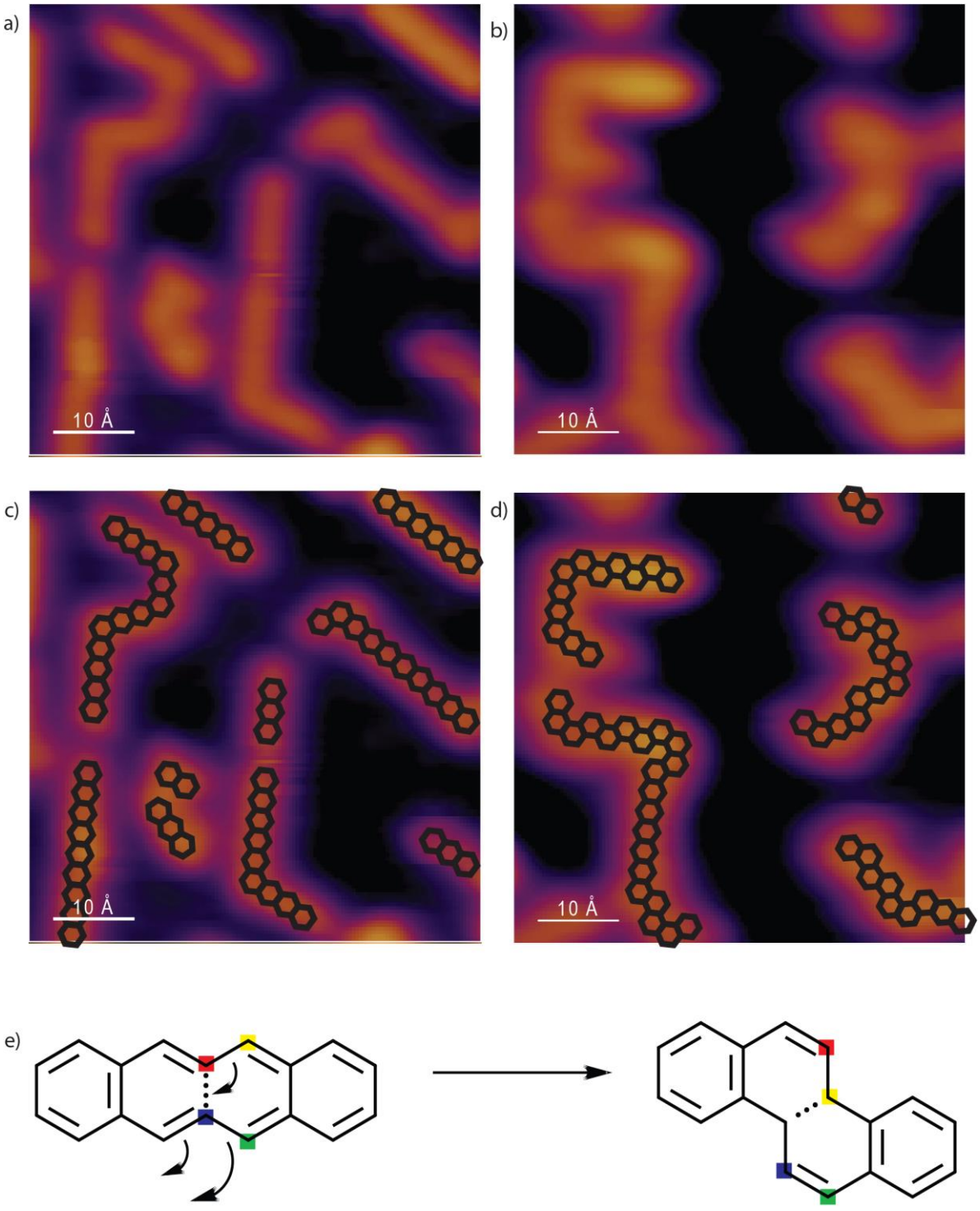

Figure 5.13

(a) is an STM image of the 1D-PAHs seen after annealing ethene on Rh(111) to 470 K and (b) is an STM image of the thicker chains seen after annealing to 520 K. (c) and (d) are the same images with models showing the kinking producing the thicker appearance of the chains after annealing. All the images have the same topographic contrast and were acquired with a voltage of 1.1 V and a current of 0.1 nA. (e) shows a model demonstrating how the kinking occurs with the breaking of just 1 C-C bond.

The HREEL spectrum upon flash annealing to this temperature is shown in the red curve in figure 5.14. A further broadening and intensity decrease of the C-H out-of-plane bending mode is observed. There is also a significant decrease in the peak relating to the C-H stretch. The region between 1000 and 1500 cm^{-1} shows a complex pattern which is related to various C-H and C-C in plane stretches of aromatic compounds.[33] Hydrogenated graphene (graphane) structures can be reasonably excluded. [34] These changes represent a decrease in the total number of peripheral hydrogens, which implies a higher degree of aromaticity (i.e. a widening of the aromatic species and dehydrogenation), consistent with kinking and widening of the chains.

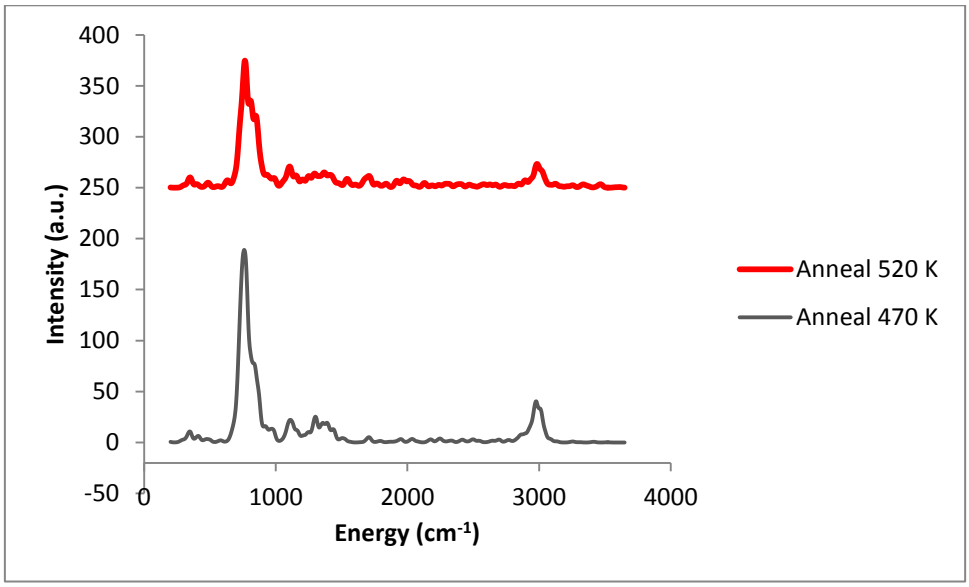

Figure 5.14

HREEL spectrums of the subsequent anneals to 470 and 520 K, of ethene after RT deposition on Rh(111).

5.3.6 $7C_6$ formation

$7C_6$, the precursor to graphene, was first identified in 2011 by Wang *et al*.[15] In this paper, to try and understand why graphene growth occurs via $7C_6$ clusters, a variety of NC_6 clusters were investigated, where N is the number of C6 rings. Figure 5.15 shows a graph of these results. The graph shows total formation energy vs N (top axis) and, on the bottom axis, the ratio between the number of peripheral carbon atoms (N_P) and the total number of carbon atoms in the cluster (N_T). In red is the total formation energy of the clusters on the Rh(111) surface, which can be seen to decrease as the cluster size increases. According to the graph, $7C_6$ is the first cluster where aggregation of carbon into

a stable cluster is energetically favourable. This is because smaller clusters will compete with break-up rates.[35]This demonstrates why $7C_6$ is seen on the surface before graphene formation, but does not explain the absence of larger clusters that are even more energetically favourable. A kinetic argument, which can be added to this thermodynamical one, is the formation mechanism of the $7C_6$ clusters (presented below).

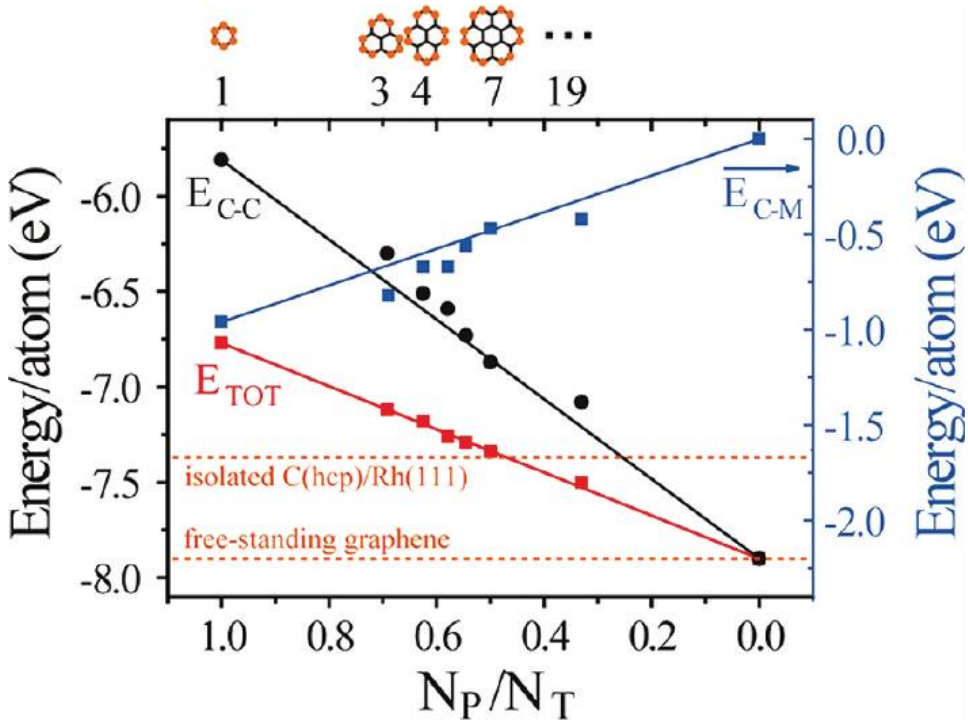

Figure 5.15

Graph showing DFT computed formation energies for NC_6 clusters adsorbed on Rh(111). Taken from reference.[15]

At 570 K, some of the ends of the chains are wider and are round in appearance (see figure 5.16). This is a curling up of the chain end, shown in figure 5.17a. This curling up is due to increased propensity of kinking, and it is by curling up that $7C_6$ is formed. Some of the ends of the chains are the same height as the rest of the chain. Others have a brighter contrast and this is thought to be due to dehydrogenation. The removal of the peripheral hydrogens is accompanied by the formation of peripheral bonding with the underlying Rh substrate. This forces the chain termination to adopt a dome-shaped configuration which results in an increased apparent height. Further high temperature STM studies were carried out by our collaborators at TUM, this time at 563 K (see figure 5.18). It can be

seen that for some chains, these round terminations light-up and then separate from the rest of the chain and in other cases; it separates first then lights-up. This shows that at this temperature, coronene-type clusters of varying hydrogen content are separated from the rest of the chain. Any remaining hydrogen content is then lost to give the previously reported $7C_6$ clusters. The remainder of the chain then either curls-up or merges with other chains to form further $7C_6$ clusters.

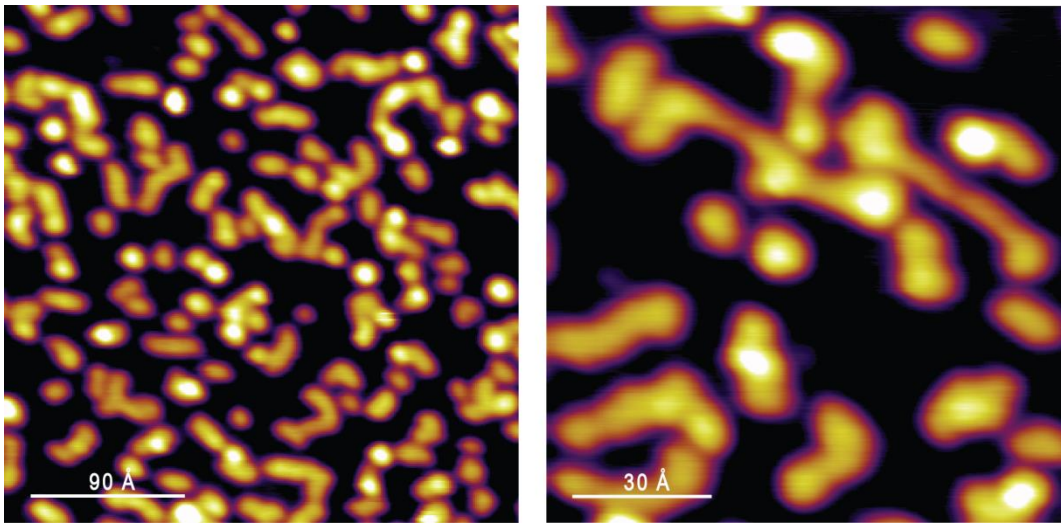

Figure 5.16

STM images showing the widening of the chain ends which occurs after the deposition of ethene on the rhodium surface and subsequent anneal to 570 K. Images were acquired with a current of 0.1 nA and voltages of 0.83 V for the image on the left and 0.12 V for the image on the right.

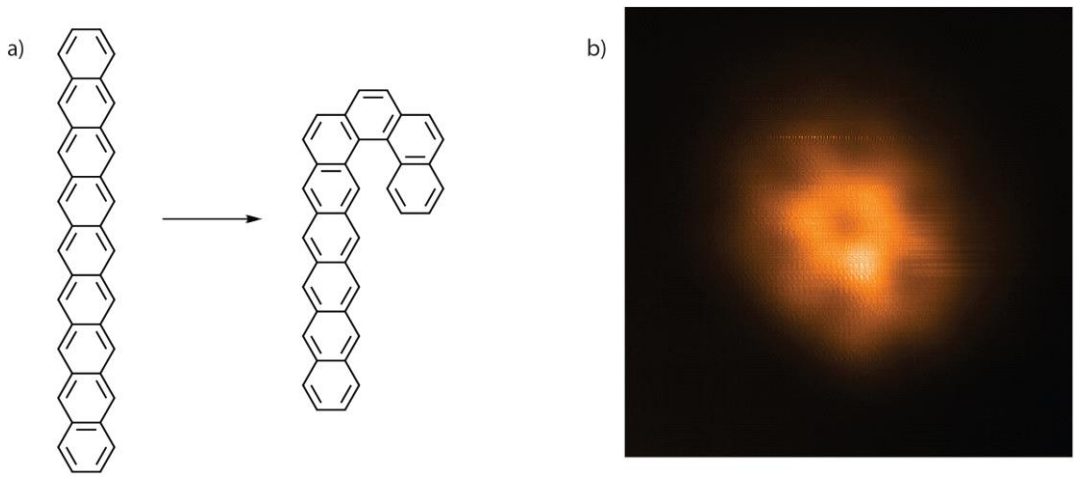

Figure 5.17

(a) shows a model of a chain curling up to produce the bright bumps at the end of the chains at 570 K. (b) is a constant height image of a $7C_6$ cluster. The image size is 20 x 20 $Å^2$, and was acquired with a current of 0.05 nA and a voltage of -0.1 V.

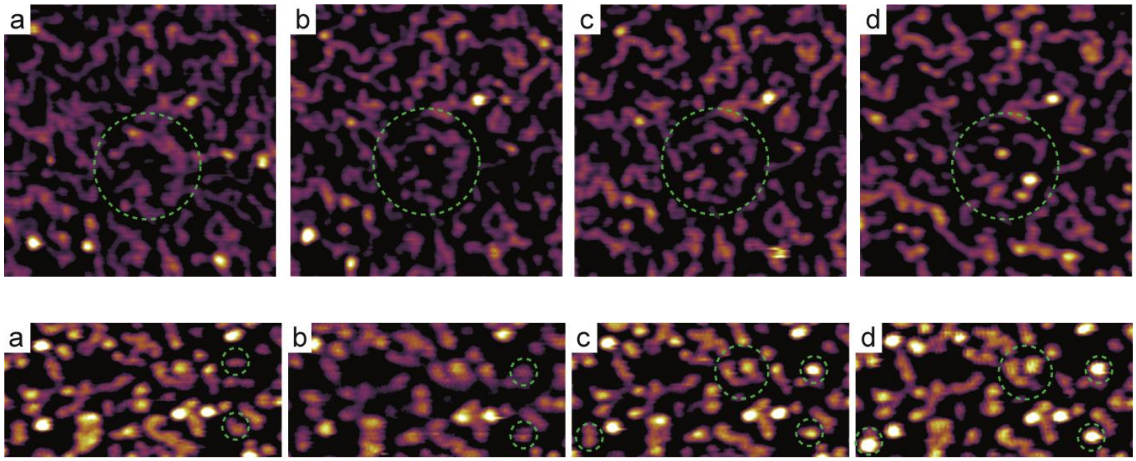

Figure 5.18

High temperature STM images of the curling up of the chain ends to form $7C_6$ carbon clusters. Upper panel shows images acquired between 490 K and 530 K. The marked area shows: (a-c) kinking and curling-up; (d) $7C_6$ precursors form upon dehydrogenation of the curled-up ends. The images are all 270 Å x 270 Å and were acquired with a current of 50 pA and a voltage of 0.5 V. Time steps: 131 min (a-b), 26 min (b-c), 109 min (c-d). Lower panel shows images acquired at 560 K. In the marked areas, the formation and detachment of $7C_6$ units from curled-up chain ends can be observed. The images are 120 Å x 250 Å and were acquired with a current of 50 pA and a voltage of 1.0 V. Time steps: 3 min (a-b), 23 min (b-c), 34 min (c-d).

Collaborators at GTech carried out DFT calculations to help understand the process by which the coronene-like clusters are released. It was found that it was likely induced by hydrogen that is released during the kinking and restructuring of the chains. Figure 5.19 shows one possible pathway, which was obtained from steered first-principles simulations. It starts with a curled up chain with a coronene-type termination. For detachment to occur, the bridging C-C bonds between the coronene-type termination and the rest of the chain need to be weakened. The calculations reveal that this occurs via hydrogenation of these carbon atoms to give an sp^3 character. This effectively lifts these atoms from the surface, above the plane of the rest of the chain, which lowers the detachment barrier. After this the detachment occurs through successive breaking of the two C-C bonds linking the cluster to the rest of the chain. This all takes place with activation energies that are compatible with the experimental conditions.

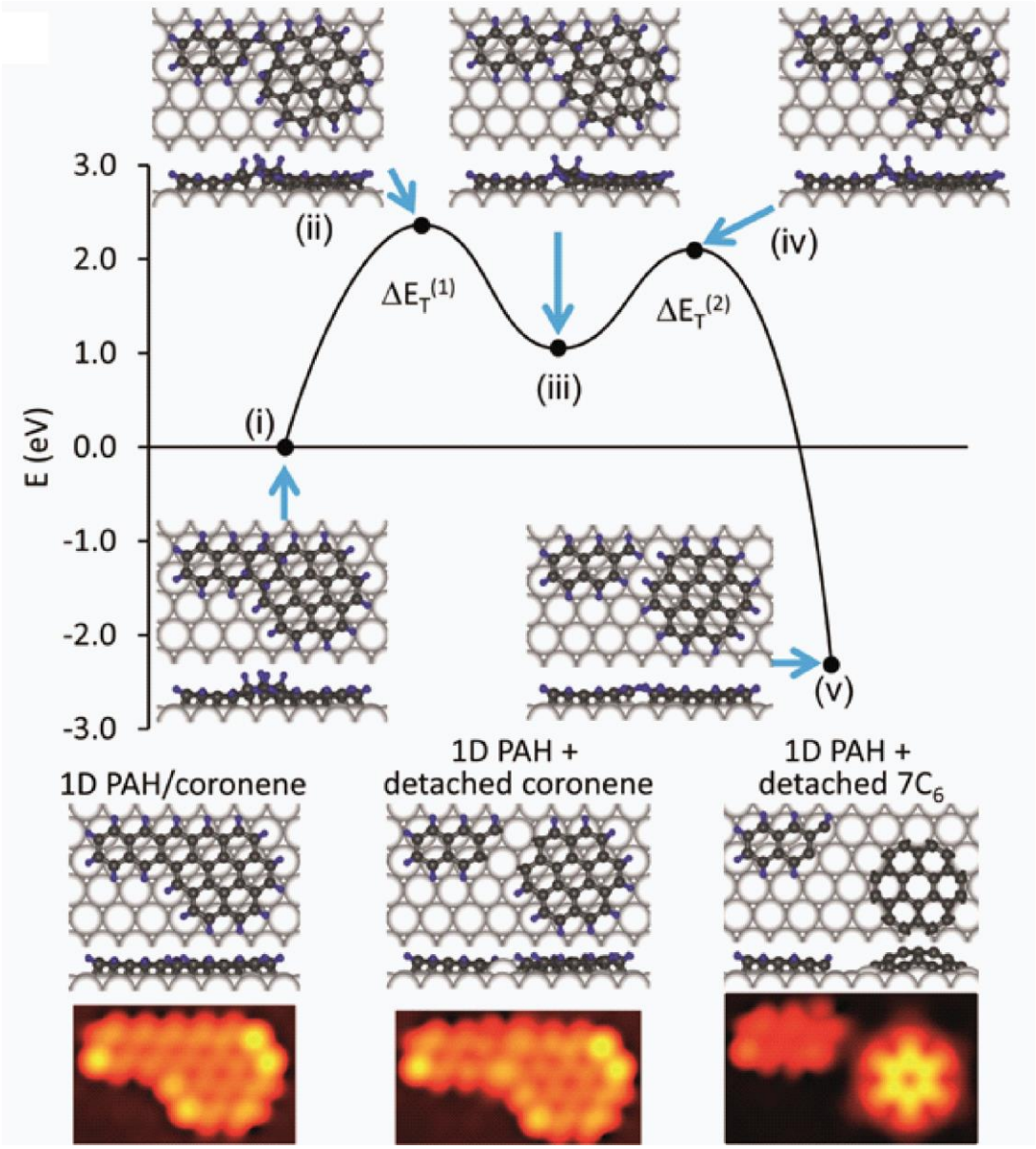

Figure 5.19 Shows first-principles DFT simulations of the pathway for cluster detachment from the 1D-PAHs after curling-up of the chain ends. The five successive steps are shown alongside the reaction coordinate. At the bottom of the figure are simulated STM images, illustrating the increase in apparent height in the middle of the dome shaped cluster that forms.

Figure 5.17b shows a high resolution image of a $7C_6$ cluster on Rh(111). The image was acquired using constant height mode of the STM. The imaging of complex molecules in constant height mode can produce higher resolution images. This is because oscillations of the tip due to the feedback loop are avoided.[36] By moving the tip close to the cluster while scanning the resolution is improved further by entering the Pauli repulsion regime. [37] Due to the dome shape of the cluster, the central part of the cluster is seen clearest

and the peripheral atoms are unseen. Even though all the atoms are not seen, six rings can clearly be seen around the central one. The symmetry of the cluster suggests that all the rings are the same size and not alternating C_5 and C_6 rings as suggested by Yuan *et al.*[38] In this study Yuan's predictions are purely thermodynamics; as they are from a global energy minimisation scheme via DFT. Whereas, the curling up mechanism described above for the formation of $7C_6$ is purely driven by kinetics.

The HREEL spectra with further flash annealing to 570 K (red curve in figure 5.20) and above (blue and green curves), reveals a general decrease in all peaks. There is a further broadening of the C-H out-of-plane bending mode and a complete loss of the C-H stretch is seen after annealing to 770 K (spectra not shown). The C-H out-of-plane bending mode is not recorded after annealing to 923 K (spectra not shown). This is consistent with increasing dehydrogenation and condensation into larger structures (i.e. clusters and eventually graphene).

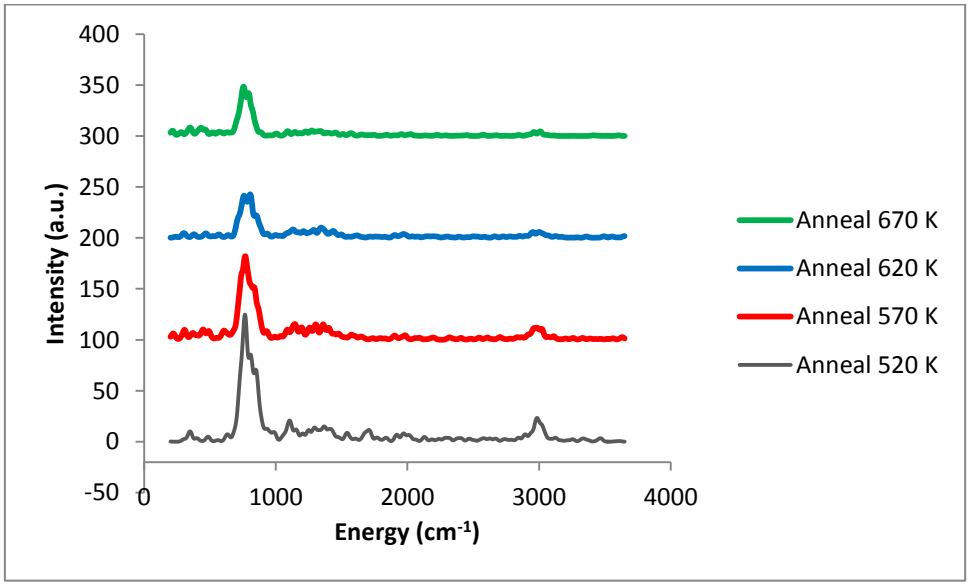

Figure 5.20

HREEL spectrums of the subsequent anneals to 520, 570, 620, and 670 K of ethene after RT deposition on Rh(111).

5.4 Discussion

The growth mechanism for the formation of graphene from ethene has been determined with the complete pathway shown in figure 5.21. Its determination has been done through a mixture of STM and HREELS experiments, with DFT support. The kinetics involved in the growth are unlike any previously reported hydrocarbon mechanism. One might naively assume that graphene growth proceeds through a series of coupling reactions. In fact after coupling, decomposition occurs which yields size-selective carbon clusters, that then go on to condense and form graphene. The whole mechanism is dictated by a delicate balance of competing strengths, existing between carbon, hydrogen, and the rhodium surface atoms, resulting in a well-defined sequence of thermally activated reactions. As indicated by the TPD spectrum acquired by the group of Somorjai,[21] and further confirmed by our HREELS investigation, two regimes exist in the thermal evolution of ethene to graphene. The first regime is the transformation from aliphatic to aromatic, through the decomposition and condensation of ethene. The second regime is the transition from the 1D-PAHs, to the 2D graphene.

The transformation from aliphatic to aromatic begins upon deposition, at RT, with the cleavage of a C-H bond which is compensated by the formation of a strong C-M bond. This converts the flat lying ethene, to the well-known upright ethylidyne.[39] As thermal energy is added to the system, more C-H bonds are cleaved and C-C bonds form, in the coupling of C_2 units to form a benzene-type species and the C_4 metallocycle. These then react together in a Diels-Alder type cycloaddition reaction to form 1D-PAHs.

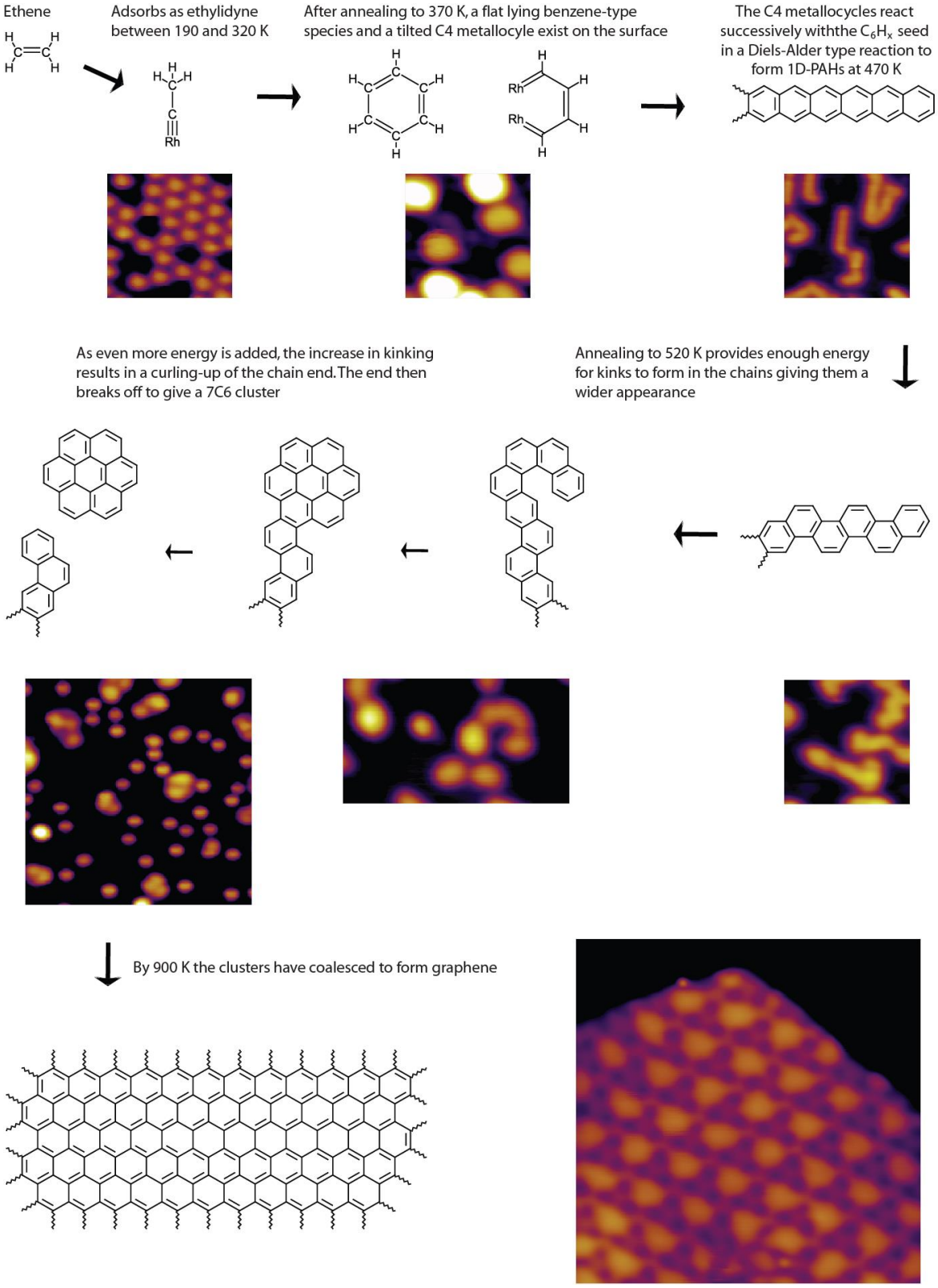

Figure 5.21

The complete pathway for the conversion of ethene to graphene, shown using models and STM images.

The second regime, beginning around 450 K, involves a slow release of hydrogen up to 700 K. This regime mainly involves isomerisation, with the breaking of C-C bonds and the formation of new ones being critical in the transformation from the 1D to the 2D. This initially results in kinking of the chains, which increase aromaticity, and hence their stability on the surface. As more energy is added to the system, further kinking results in the curling-up of the chain ends. This curling-up results in coronene-like chain terminations. Further thermal energy leads to the detachment of these round chain terminations. In some cases dehydrogenation occurs first, and in others afterwards. In both cases the cleaving of the peripheral hydrogens from the coronene moiety is compensated, by the formation of C-M bonds at the periphery, which force it to adopt a dome-shaped configuration. The remainder of the chain then curls up again, or merges with other chains, for the subsequent production of additional $7C_6$ clusters. These clusters have been shown previously to destabilise, with further annealing, and coalesce to form graphene.[15]

The use of STM was critical in the assignment of the intermediate species, as it allowed for their direct observation. Extensive research on this system had been carried out previously, using a variety of traditional spectroscopic techniques,[21] [14] [22] but no structural identification of the intermediates was made. These techniques often resulted in complex spectra that were difficult to interpret. When considering the identification of the 1D-PAHs, the structure is microscopically simple, but has a complex vibration spectrum due to the 7-8% difference in the lattice parameter of the Rh(111) substrate (2.69 Å) compared to the periodicity of the carbon rings in the 1D-PAHs (~2.5 Å). The difference in lattice parameter is enough to result in a variety of C/Rh adsorption registries over the length of the chain, giving a complex spectrum. A technique such as HREELS is not enough to make the assignment of the intermediates alone, but the results are fully consistent with the assignments made using STM.

Figure 5.22 shows the HREEL spectrum for ethene on Rh(111) between the temperatures of 300 and 770 K and figure 5.23 shows the trends for the intensity of selected frequencies vs temperature. The trends show a dramatic decrease in the umbrella mode and the aliphatic C-H stretch at around 373 - 423 K. The C-H out-of-plane bending and aromatic C-H stretch increase in intensity at the same temperature, implying that this is

the temperature where the conversion of ethylidyne to aromatic species occurs. This is consistent with the TPD which shows a first regime where aromatic species are created and a second regime where 1D-PAHs become 2D graphene. At higher temperatures, HREELS shows a progressive decrease of all vibrations. This is attributed to dehydrogenation and associated condensation of aromatic species into larger structures.

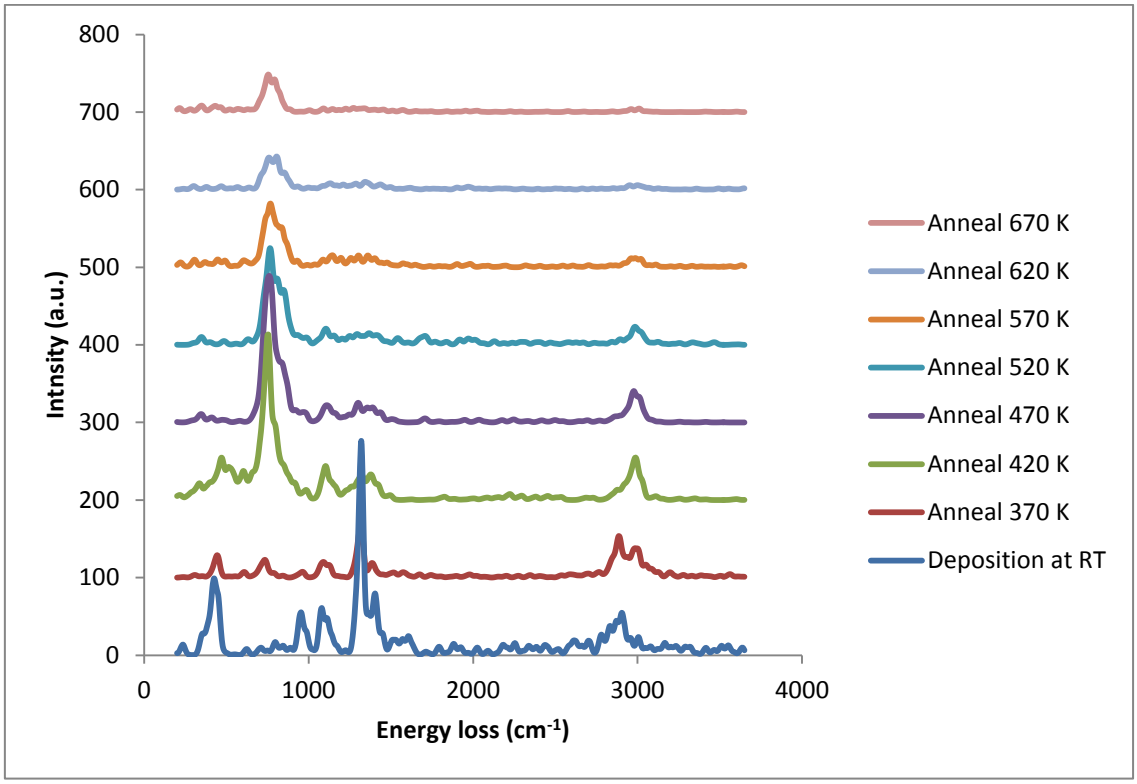

Figure 5.22

Shows all the HREEL spectra of ethene after RT deposition on Rh(111) and subsequent anneals up to 670 K.

As well as HREELS and the TPD of Somorjai, DFT was valuable in the support of the STM results. The DFT adds weight to the speculative assignment of C_4 as a building block for chain formation, by confirming a higher contrast compared to benzene. The DFT also showed that the cluster detachment was a favourable reaction and was compatible with the experimental conditions.

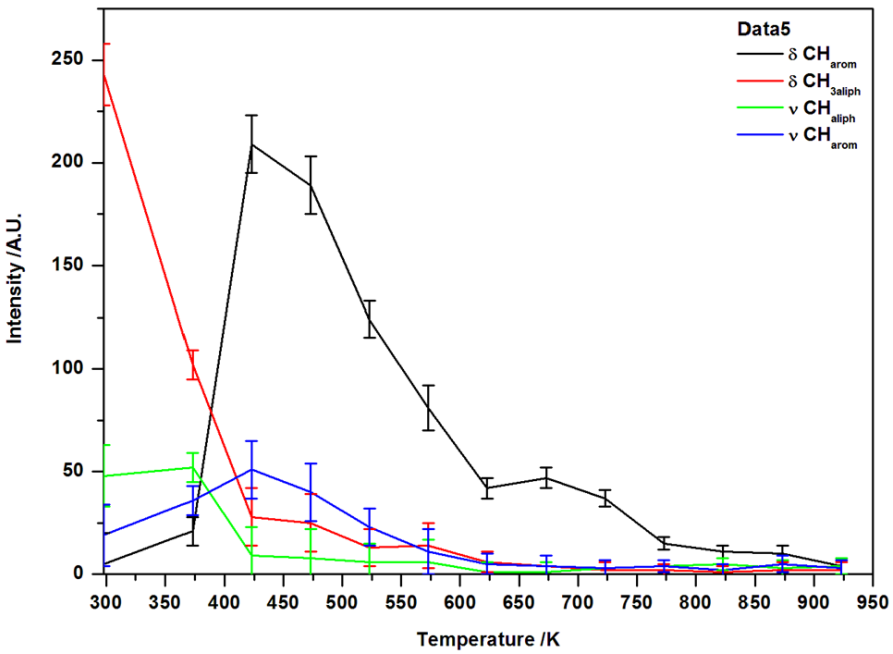

Figure 5.23

Shows intensity trends of selected HREELS frequencies vs temperature.

5.5 Conclusion

In conclusion, the pathway from ethene to graphene has been determined. This was found to occur through the formation of one-dimensional aromatic hydrocarbons, which then decompose to form size-selective carbon clusters. These clusters are the precursors that coalesce on the surface to form graphene. The pathway provides a great deal of information on the balance of C-C, C-H, and C-Rh bond strengths involved in the evolution of ethene to graphene on rhodium. The growth mechanism is expected to proceed similarly on other metal surfaces, making it a valuable source of information. The knowledge can be used in the optimisation of graphene growth conditions, as well as helping with the fabrication of methods to prevent coke formation on metal catalysts.

References

[1] M. J. Allen, V. C. Tung and R. B. Kaner, *Chemical Reviews* **2009**, *110*, 132-145.
[2] J. K. Wassei, M. Mecklenburg, J. A. Torres, J. D. Fowler, B. C. Regan, R. B. Kaner and B. H. Weiller, *Small* **2012**, *8,* 1415.
[3] P. Zhao, A. Kumamoto, S. Kim, X. Chen, B. Hou, S. Chiashi, E. Einarsson, Y. Ikuhara and S. Maruyama, *The Journal of Physical Chemistry C* **2013**, *117,* 10755-10763.
[4] A. M. Baro and H. Ibach, *Journal of Chemical Physics* **1981**, *74*, 4194-4199.
[5] W. T. Tysoe, G. L. Nyberg and R. M. Lambert, *Journal of the Chemical Society, Chemical Communications* **1983**, 623-625.
[6] C. Egawa, S. Naito and K. Tamaru, *Journal of the Chemical Society, Faraday Transactions 1: Physical Chemistry in Condensed Phases* **1986**, *82*, 3197-3204.
[7] T. A. Land, T. Michely, R. J. Behm, J. C. Hemminger and G. Comsa, *Applied Physics A: Materials Science & Processing* **1991**, *53*, 414-417.
[8] T. S. Marinova and K. L. Kostov, *Surface Science* **1987**, *181*, 573-585.
[9] B. E. Bent and G. A. Somorjai, *Advances in Colloid and Interface Science* **1989**, *29*, 223-275.
[10] H. J. Borg, R. M. Vanhardeveld and J. W. H. Niemantsverdriet, *Journal of the Chemical Society-Faraday Transactions* **1995**, *91*, 3679-3684.
[11] M. Li, W. Guo, R. Jiang, L. Zhao, X. Lu, H. Zhu, D. Fu and H. Shan, *The Journal of Physical Chemistry C* **2010**, *114*, 8440-8448.
[12] Z.-X. Chen, H. A. Aleksandrov, D. Basaran and N. Rösch, *The Journal of Physical Chemistry C* **2010**, *114*, 17683-17692.
[13] L. H. Dubois, D. G. Castner and G. A. Somorjai, *Journal of Chemical Physics* **1980**, *72*, 5234-5240.
[14] G. A. Somorjai, *Chemical Society Reviews* **1984**, *13*, 321-349.
[15] B. Wang, X. Ma, M. Caffio, R. Schaub and W.-X. Li, *Nano Letters* **2011**, *11*, 424-430.
[16] P. Lacovig, M. Pozzo, D. Alfè, P. Vilmercati, A. Baraldi and S. Lizzit, *Physical Review Letters* **2009**, *103*, 166101.
[17] Y. Cui, Q. Fu, H. Zhang and X. Bao, *Chemical Communications* **2011**, *47*, 1470-1472.
[18] R. J. Koestner, M. A. Vanhove and G. A. Somorjai, *Surface Science* **1982**, *121*, 321-337.
[19] L. L. Kesmodel, L. H. Dubois and G. A. Somorjai, *Chemical Physics Letters* **1978**, *56*, 267-271.
[20] A. Wander, M. A. Vanhove and G. A. Somorjai, *Physical Review Letters* **1991**, *67*, 626-628.
[21] B. E. Bent and G. A. Somorjai, *Advances in Colloid and Interface Science* **1989**, *29*, 223-275.
[22] R. J. Levis, L. A. Delouise, E. J. White and N. Winograd, *Surface Science* **1990**, *230*, 35-46.
[23] B. E. Koel, J. E. Crowell, B. E. Bent, C. M. Mate and G. A. Somorjai, *The Journal of Physical Chemistry* **1986**, *90*, 2949-2956.
[24] B. Wang, M. Caffio, C. Bromley, H. Früchtl and R. Schaub, *ACS Nano* **2010**, *4*, 5773-5782.
[25] S. L. Yau, Y. G. Kim and K. Itaya, *Journal of Physical Chemistry B* **1997**, *101*, 3547-3553.
[26] A. Candian, P. J. Sarre and A. G. G. M. Tielens, *The astrophysical journal letters* **2014**, *791*, L10.
[27] R. M. Ormerod, R. M. Lambert, D. W. Bennett and W. T. Tysoe, *Surface Science* **1995**, *330*, 1-10.
[28] C. J. Baddeley, R. M. Ormerod, A. W. Stephenson and R. M. Lambert, *Journal of Physical Chemistry* **1995**, *99*, 5146-5151.
[29] J. R. Lomas, C. J. Baddeley, M. S. Tikhov and R. M. Lambert, *Langmuir* **1995**, *11*, 3048-3053.
[30] R. M. Lambert and R. M. Ormerod, *Materials Chemistry and Physics* **1991**, *29*, 105-115.
[31] R. M. Ormerod, R. M. Lambert, H. Hoffmann, F. Zaera, J. M. Yao, D. K. Saldin, L. P. Wang, D. W. Bennett and W. T. Tysoe, *Surface Science* **1993**, *295*, 277-286.
[32] E. Clar, *Polycyclic hydrocarbons*, Academic Press, **1964**.

[33] a) Q. Chen, T. Rada, A. McDowall and N. V. Richardson, *Chemistry of Materials* **2002**, *14*, 743; b) M. Preuss, R. Miotto, F. Bechstedt, T. Rada, N. V. Richardson and W. G. Schmidt, *Physical Review B* **2006**, *74*, 115402.
[34] J. O. Sofo, A. S. Chaudhari and G. D. Barber, *Physical Review B* **2007**, *75*, 153401.
[35] A. Zangwill and D. D. Vvedensky, *Nano Letters* **2011**, *11*, 2092-2095.
[36] F. Moresco, G. Meyer, H. Tang, C. Joachim and K. H. Rieder, *Journal of Electron Spectroscopy and Related Phenomena* **2003**, *129*, 149-155.
[37] C. Weiss, C. Wagner, C. Kleimann, M. Rohlfing, F. S. Tautz and R. Temirov, *Physical Review Letters* **2010**, *105,* 86103.
[38] Q. Yuan, J. Gao, H. Shu, J. Zhao, X. Chen and F. Ding, *Journal of the American Chemical Society* **2011**, *134,* 2970-2975
[39] A. Wander, M. A. Van Hove and G. A. Somorjai, *Physical Review Letters* **1991**, *67*, 626-628.

Chapter 6: Growth mechanism of graphene from different feedstocks on Rh(111)

6.1 Introduction

In chapter 5 the growth mechanism for graphene from ethene was discussed. But what is the mechanism when different feedstocks are used? In this chapter, the mechanism is explored for larger hydrocarbons. Small hydrocarbons such as methane and ethene are the main focus of worldwide research; but knowledge of the mechanism for larger feedstocks would enable a greater understanding of the mechanism for these smaller molecules. The evolution of ethene to graphene discussed in chapter 5 goes via intermediates of increasing size. The first steps involve coupling and cyclotrimerisation reactions to produce a C_4 metallocycle and a C_6 species (similar to benzene but likely H deficient, refer to section 5.3.4). These then react to form 1D-PAHs, with the C_6H_x species acting as the seed and the C_4 units reacting, in successive addition reactions, to produce the aromatic chain. These chains have long, straight segments with 120° kinks. With increasing thermal energy, the chains become more kinked and eventually the ends curl-up. The curling-up of the ends produces a coronene-type chain termination. This then dehydrogenates and breaks off to give $7C_6$ clusters, which eventually coalesce to give graphene in a Smoluchowski-type growth mechanism.

It is known, that graphene can be produced from almost any carbon containing feedstock (including cockroach legs and dog faeces[1]). Despite the end product being independent of feedstock, it is likely the assembly pathway will be dependent of it. On changing the feedstock, a number of questions arise with regards to the pathway. Firstly, if C_4 units are solely responsible for growth, then either (1) larger hydrocarbons must dissociate first, or (2) the coupling mechanism is different, thereby leading to different intermediate morphologies. If (1), then what relationship exists between the size of the hydrocarbon and its break-up. If we begin with 1D PAHs, do these break-up only to reform? If coronene/$7C_6$ is identified as the bottleneck, what happens if coronene is used as the feedstock? Would these decompose to C_4 or would they dehydrogenate directly to $7C_6$. And what about larger hydrocarbon fragments? Were we to utilise carbon rings made up

of 5 or 7 carbon atoms, how do these transform into C_6 graphene. Also what is the effect if other chemical elements, such as oxygen in alcohols, are present in the feedstock? In this chapter some of the above questions will be addressed.

The focus of this work is on employing feedstocks that are structurally similar to the different intermediates identified in the ethene pathway. Emphasis will be put on the identification of the parallels and differences occurring in the coupling reactions, intermediates, and assembly mechanisms that lead to the synthesis of graphene using these more structurally complex, and larger (in carbon content) hydrocarbon feeds. The feedstocks studied were benzene, tetracene, and perylene. These were chosen for various reasons. Benzene was studied as it is the simplest aromatic system, with the main focus being to find out whether it would break up to C_2 and C_4 units, or whether the benzene molecules would polymerise. A benzene-type species is also one of the proposed intermediates in the ethene to graphene pathway, so this should also be able to further confirm this assignment. The tetracene is a simple model of the 1D-PAHs, so it is interesting to explore its stability on the surface and polymerisation mechanism. Perylene is thicker than the 1D-PAHs, so the motivation is in finding out if it breaks down to form the chains or if the mechanism bypasses the chains.

These three molecules investigated are also of interest because they possess π-conjugated systems. These types of systems are important components of organic-electronic and photonic devices.[2] [3] The understanding of their stability and interaction with a support is key, for the improvement and development of such novel functional devices.

6.1.1 Previous work from literature

Benzene is known to adsorb on the Rh(111) surface, and other metal surfaces, with the plane of the molecular ring parallel to the surface.[4] The adsorption site is seen to be dependent on coverage; with higher coverages favouring the hcp hollow site and lower coverages the bridge site.[5] On the metal surface the benzene molecules adopt a (3×3) arrangement, and at higher coverage they become more tilted and rearrange to a c(2√3×3).[6] Both these structures involve the presence of one or two CO molecules per unit cell. In the absence of CO a (√19×√19)R23.4° structure is formed.[7]

In the 1980s the decomposition of benzene was studied on Rh(111) using HREELS, TPD, and LEED.[4] [8] The results suggested the breakdown of benzene to CH and C_2H species at ~400 K. As the temperature increased, these species were expected to polymerise before forming graphite. More recent theoretical work, however, suggests that the C_2H stoichiometry is the result of C-H bond scission giving dehydrobenzene (C_6H_3).[9]

Tetracene has not been studied on a rhodium surface but has on other transition metal surfaces including copper,[10] silver[11] [12] and ruthenium.[13] On these surfaces the tetracene adsorbs in a flat-lying geometry, with its molecular plane parallel to the surface. There is also an interaction between the tetracene and the surface, with the long molecular axis of the tetracene aligned along the high symmetry directions of the substrate. There are examples of local ordering of the tetracene on the surface at higher coverages. On some surfaces, gentle annealing results in a change in the molecular arrangements observed. Very little work has been done with annealing the tetracene to higher temperatures. The only surface where the high temperature annealing was carried out was Cu(110), and in this case it was concluded that tetracene desorbed and/or decomposed at temperatures above 600 K.[10]

Like tetracene, perylene has been studied on several metal surfaces, but not rhodium. It is adsorbed in a flat-lying geometry with its plane parallel to the surface.[14] [15] The orientation of the perylene is influenced by the high symmetry directions of the surface, indicating an interaction between the two. On different transition metal surfaces, different structures can be formed, but order tends to increase with coverage.[14] [15] [16] In particular, perylene molecules are seen to align in chains, especially along the rows of (110) surfaces. Like tetracene, very few experiments have involved more than just a gentle anneal. The perylene was heated to 600 K on Cu(110) and found to desorb.[17] Multilayers desorbed at a lower temperature, indicating the interaction with the surface is stronger than the intermolecular interaction. A surface such as Rh(111) has a stronger interaction with hydrocarbons, so there is a greater chance of decomposition to graphene over desorption.

6.2 Methodology

The Rh(111) crystal was prepared as described in section 3.2.1. The benzene was deposited at room temperature, by exposing the sample to a background pressure of 1×10^{-8} mbar of vapour for 1 minute. The benzene was reagent grade (purity >99%) which was further purified using pump-freeze-thaw cycles. After deposition the sample was quickly cooled and transferred to the STM. The sample was then sequentially annealed for 30 seconds to 370, 420, 450, 470, 500, 570, and 670 K with each stage imaged by STM at LN_2.

The tetracene and perylene were deposited using molecular evaporators. Before deposition the tetracene was degassed at 325 K and the perylene at 345 K. During deposition the tetracene was heated to 350 K, which corresponded to a dosing pressure of 1.5×10^{-9} mbar, for 1 minute with the sample at 160 K. The perylene was heated to 390 K for 1 minute, giving a dosing pressure of 2×10^{-9} mbar with the sample at 180 K. After deposition the samples were quickly cooled before transfer to the STM. Both samples were heated sequentially up to 870 K in ~50 K increments, with each stage observed using STM.

6.3 Results

6.3.1 Benzene

Figure 6.1 shows the benzene after deposition at room temperature. The images show a number of protrusions of identical aspect randomly dispersed on the surface. It is these protrusions that are the benzene molecules. The benzene molecules have an electronic height of ~1 Å, with a full width at half maximum (fwhm) diameter of ~7 Å. This can be seen in figure 6.2, where there is a profile plot of the benzene, alongside a variety of other species. The height of 1 Å is consistent with planar and fully hydrogenated benzene molecules which are expected. At this temperature the benzene is fairly disordered on the surface. However, there are instances of benzene molecules clustered together, hinting at an attractive interaction between the molecules. This attractive interaction is likely restricted by the limited mobility of the benzene upon deposition. With minimal diffusivity at RT an ordered arrangement of molecules cannot be achieved.

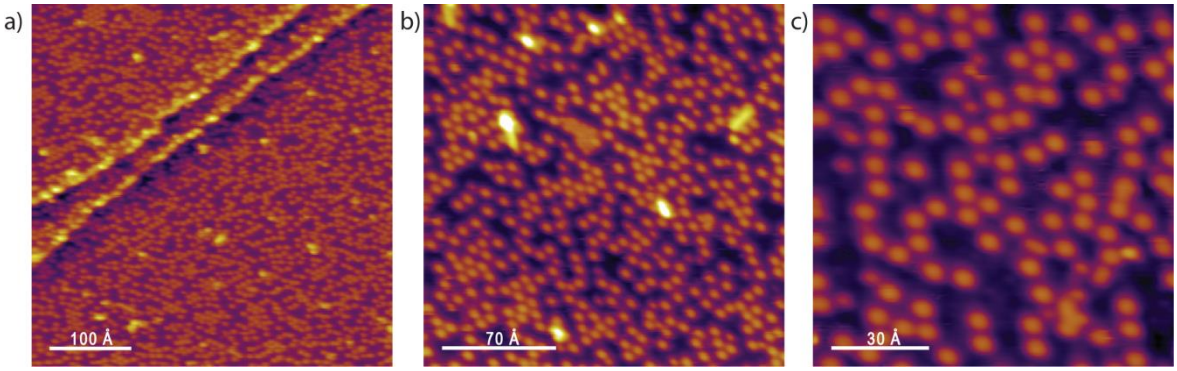

Figure 6.1

STM images of benzene after deposition on Rh(111) at room temperature. Images were acquired with a current of 0.1 nA and voltages of (a) 1.04 V, (b) 0.75 V, and (c) 0.45 V.

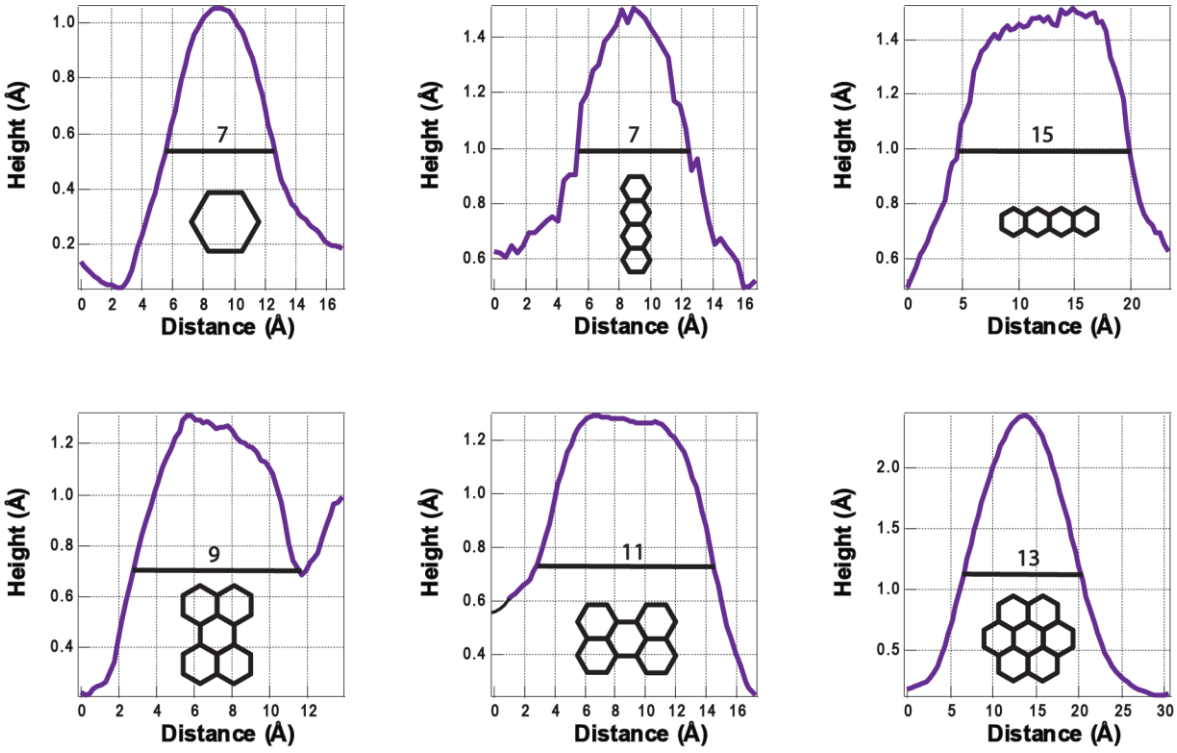

Figure 6.2

Profile plots showing the height and width of benzene, tetracene, perylene and 7C_6 on Rh(111).

Upon annealing to 370 K the individual benzene molecules appear the same but they are now ordered in a hexagonal arrangement (see figure 6.3). At this temperature the benzene molecules possess enough thermal energy that diffusivity is increased enough for order to be achieved. It has been well documented that benzene forms an ordered

(3x3) structure on Rh(111),[18] [19] but this structure involves the presence of two CO molecules per unit cell. This amount of CO is not seen to be present on the surface so likely the CO free (√19×√19)R23.4° structure is formed.[7] This arrangement is similar in appearance to the (3×3) but the unit cell is slightly smaller (interatomic distance of 6.77 Å instead of 8.09 Å). The (3×3) is aligned to the high symmetry directions of the crystal but the (√19×√19)R23.4° has a rotation of ~6°. A model showing the similarity between the two structures is shown in figure 6.4. In the (√19×√19)R23.4° configuration, it adsorbs in an off bridge-site which can be seen in the right-hand model in figure 6.4.[7] For this (√19×√19)R23.4° configuration, it is the only positioning where all atoms in the unit cell are adsorbed in the same site. For example, if the outer benzene molecules of the unit cell were adsorbed in the hcp-site then one of the inner molecules would be adsorbed in a top-site and the other in an fcc-site.

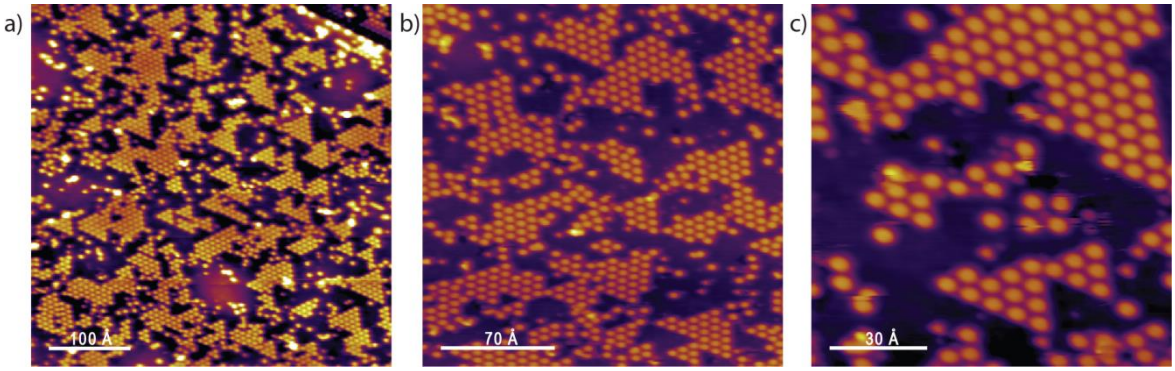

Figure 6.3

STM images of benzene on Rh(111) after annealing to 370 K. Images were acquired with a current of 0.1 nA and for (a) a voltage of 1.08 V and for (b) and (c) a voltage of 0.75 V.

Since the (3×3) and the (√19×√19)R23.4° configurations are so similar, it is difficult to distinguish between them using STM, particularly with the levels of thermal drift seen in some of the images. Figure 6.5 shows an STM image where the benzene molecules have a uniform hexagonal arrangement suggesting little compression of the image has occurred. For this image a periodicity of just above 8 Å exists, which is comparable to the (3×3) arrangement. However, due to the high level of vacuum present in the system and the cleanliness of the bare surface it is unlikely that the high levels of CO normally associated with the (3×3) are present. In the absence of atomic resolution on the rhodium substrate

or analysis from other techniques, an assignment of configuration cannot be definitively made. Perhaps the CO free (√19×√19)R23.4° structure observed previously is only present at high coverages and that a (3×3) exists for lower coverages, such as that seen here.

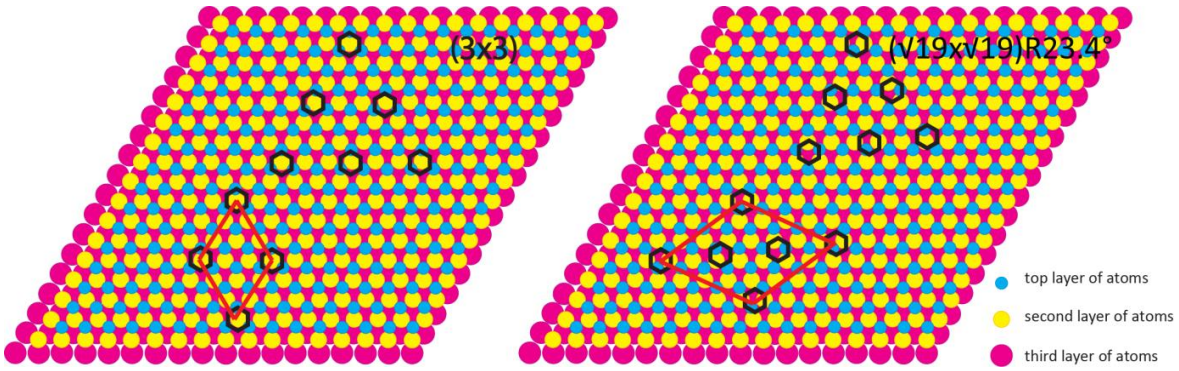

Figure 6.4

Model comparing the (3×3) and the (√19×√19)R23.4° on a (111) surface.

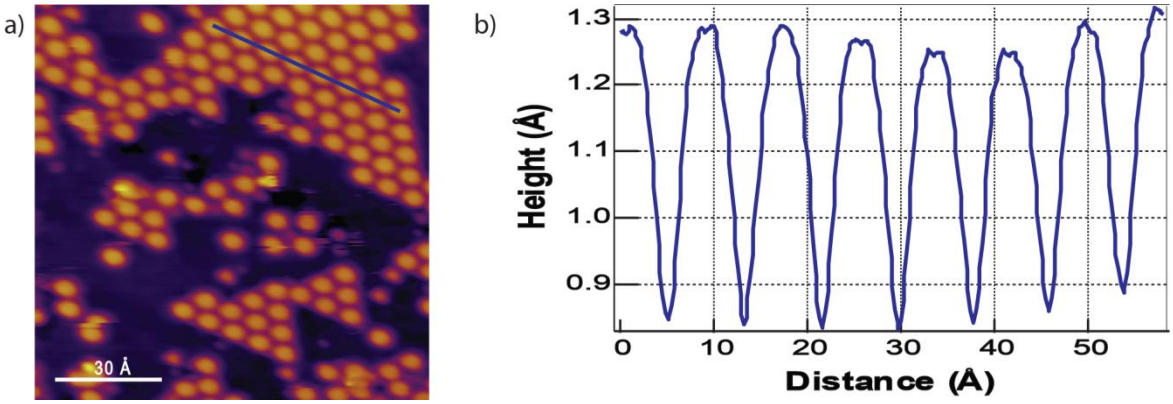

Figure 6.5

(a) shows an STM image of the benzene molecules with a uniform hexagonal arrangement which suggests limited thermal drift. (b) is the line profile over the benzene molecules indicated in (a), showing a periodicity of just over 8 Å which is comparable to a (3×3) arrangement.

The benzene islands seem to show a preference for just three of the six symmetry directions, giving the islands the appearance of upward facing triangles. For a (√19×√19)R23.4° structure, with the benzene adsorbed in the expected off-bridge site, there is no distinction between the upward and downward facing triangles that would rationalise this preference (see figure 6.6). However, a (3×3) orientation would explain the triangular shaped islands. If, for example, the benzene molecules were adsorbed in

the expected hcp site, then the carbon atoms on the periphery of the island are either directly above an atom or over a hollow site depending on the orientation of the edge of the island. This can also be seen in figure 6.6.

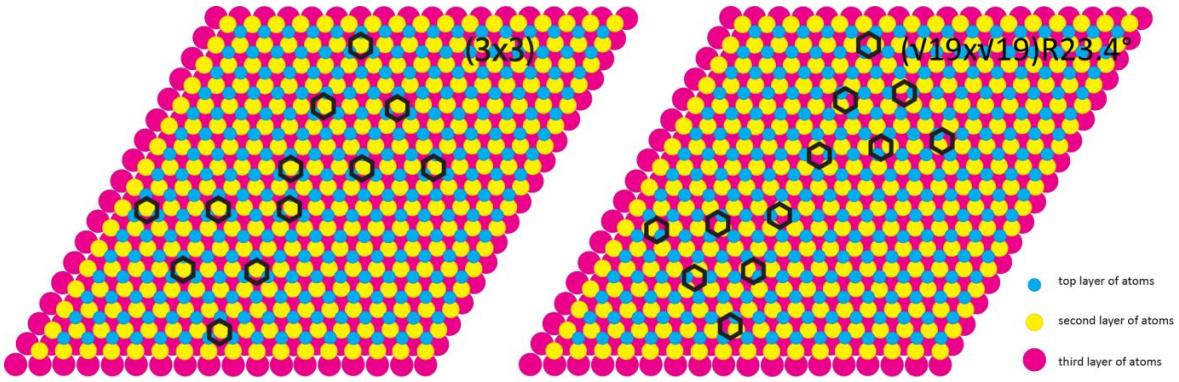

Figure 6.6

Model showing how the interaction with the surface is different at the periphery of a triangular (3×3) island depending which way up it is. No such difference is observed with triangular islands of (√19×√19)R23.4°.

Figure 6.7 shows the surface after annealing to between 420 and 470 K. The sample is no longer ordered and four surface species appear to be present. One of these species appears similar to the benzene observed previously. Hence, it is undecomposed benzene and/or similar C_6 species, with possibly less hydrogen. There is a second surface species of similar width but with a greater electronic height (~1.4 Å). This is similar to that seen at the first stages of ethene decomposition and is assigned to C_4H_x, for the reasons described in section 5.3.3. The third species is smaller but is also seen in the early stages of ethene decomposition and is assigned to H. The fourth species' are short chains, most likely 1D-PAHs which are an important intermediate in ethene decomposition to graphene.

This demonstrates a decomposition of the benzene, through reverse cyclotrimerisation to C_4 and C_2 species (which is then followed by cyclotrimerisation back to a benzene-type species). There is no visual evidence of C_2 species on the surface, but it is however likely that the cooling for STM acquisition would cause coupling to form C_4 and cyclotrimerisation to form C_6H_x, or that the C_2 species is too short lived to be observed. The presence of hydrogen also confirms the loss of hydrogen from the intermediates that occurs during chain formation.

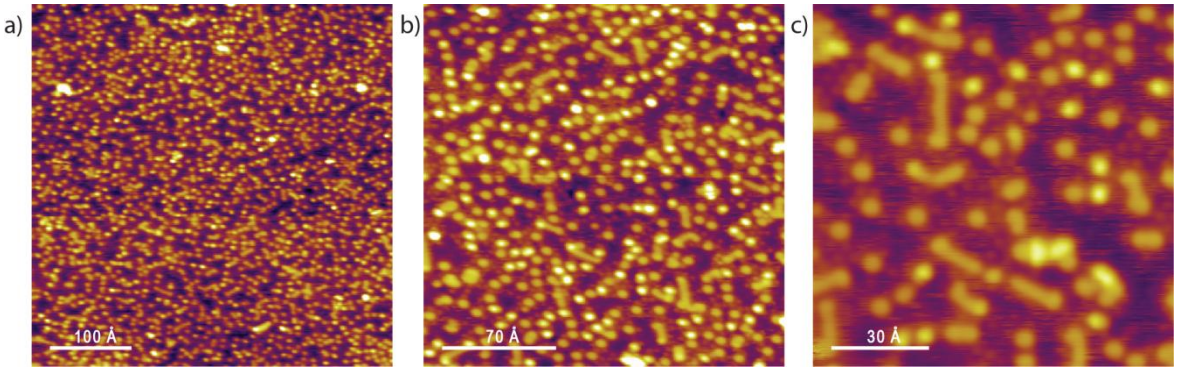

Figure 6.7

STM images of benzene on Rh(111) after annealing to between 420 and 470 K. Images were acquired with a current of 0.1 nA and a voltage of 0.2 V for (a), 0.32 V for (b), and 0.52 V for (c).

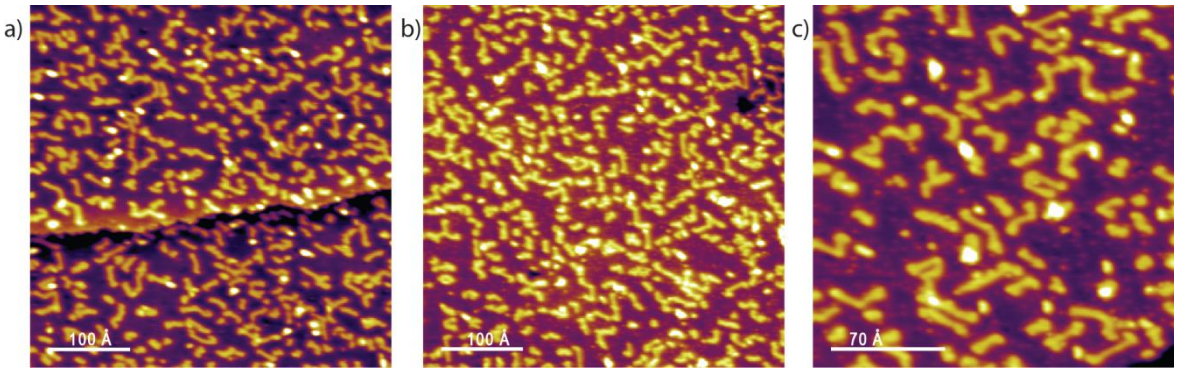

Figure 6.8

STM images of benzene on Rh(111) after annealing to 500 K. Images were acquired with a current of 0.1 nA and a voltage of 1.04 V for (a), and 0.46 V for (b) and (c).

At 500 K, the smaller species are no longer present and only chains exist on the surface (see figure 6.8). These chains are slightly thicker than the short chains seen previously and are quite "wiggly" in appearance. These chains are reminiscent of the chains seen from ethene decomposition at 530 K. These chains are hence ascribed to kinked 1D-PAHs. As the system is annealed further, bright protrusions are observed at the end of the chains as highlighted by the red circles in figure 6.9. These bright protrusions are the result of the chains curling-up at the end to form $7C_6$ clusters, like for ethene and described in section 5.3.6. Also in the images in figure 6.9 are round protrusions with a width of ~13 Å (fwhm) and a height in the region of 2 Å. These are the $7C_6$ clusters formed from the curling up of the chains, with the variations in height due to different

degrees of dehydrogenation (with the highest fully dehydrogenated and adopting a dome shaped configuration). These $7C_6$ clusters are the previously reported intermediates in the formation of epitaxial graphene.[20] [21]

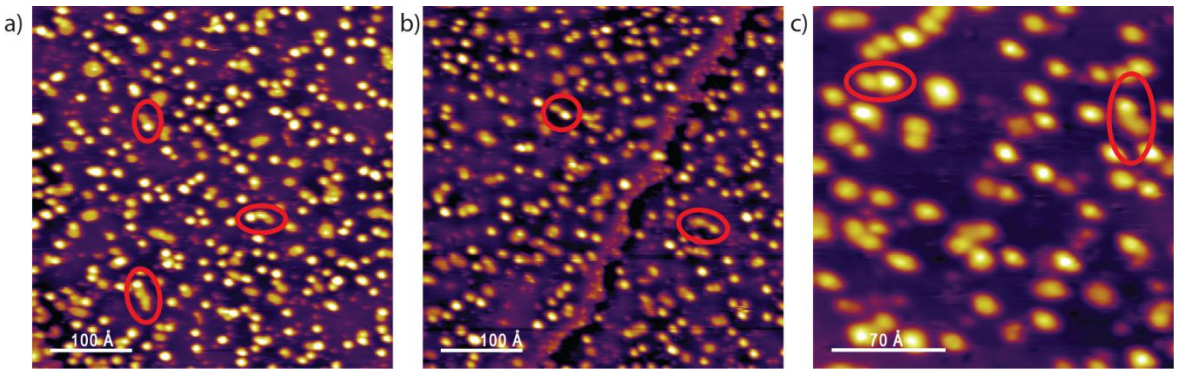

Figure 6.9

STM images of benzene on Rh(111) after annealing to 670 K. The red circles highlight examples of the bright protrusions as the ends of the chains. Images were acquired with a current of 0.1 nA and a voltage of 1.04 V for (a) and (b), and 0.43 V for (c).

The benzene follows the same route to graphene as the ethene does, further validating the significance of the pathway. Since benzene is too unreactive towards polymerisation the process begins with the decomposition of benzene molecules to C_4 (and C_2). Some of these then reform a new C_6 species which act as the seed for chain formation. The C_4 joins successively to this seed, in an addition type reaction to form the 1D-PAHs. The pathway continues in the same manner as for ethene, resulting in the production of graphene at ~900 K.

6.3.2 Tetracene

The tetracene after deposition on Rh(111) at 160 K is shown in figure 6.10. Upon deposition, the tetracene molecules appear as short chains, with a similar appearance to that seen previously on other metal surfaces.[10] [13] They have a height of 1 Å with a width of ~7 Å (fwhm) and a length of 15 Å (fwhm). The width of the chains is consistent with the diameter of the benzene seen previously (see the profile plots in figure 6.2). The molecules appear to be randomly dispersed on the surface, with some instances of molecules in close proximity but without clustering. This is likely due to a lack of diffusivity on the surface. The tetracene lies along the high symmetry directions of the surface, and along with the lack of diffusivity, this suggests a strong interaction with the

surface. There is no change in appearance till 570 K, demonstrating the stability of tetracene on a metal surface.

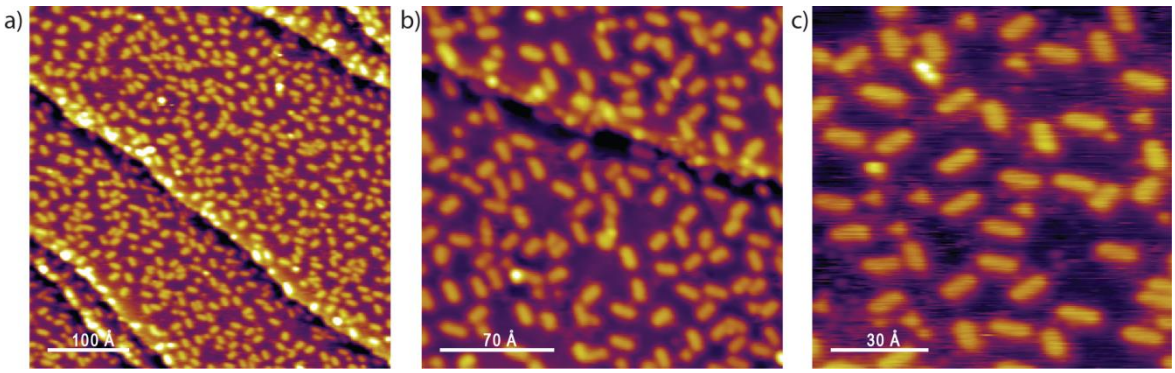

Figure 6.10

STM images of tetracene on Rh(111) after deposition. Images were acquired with a current of 0.1 nA for (a) and (b) and 0.2 nA for (c), and a voltage of 0.36 V for (a), 1.04 V for (b), and 0.52 V for (c).

Upon closer inspection of higher magnification STM images (see Fig 6.11), it was noted that some tetracene molecules have a long thin appearance and others a relatively short and wide one. DFT calculation carried out at the University of St Andrews, by José Garrido Torres (within our research group), show that this is due to the adsorption site of the tetracene. The calculations show that the favoured adsorption site for the individual aromatic rings in tetracene is a bridge-site. Incidentally, this is also the site with the strongest interaction with the rhodium surface for the full graphene monolayer.[22] There are two favoured ways that tetracene can have its rings over the bridge sites: with the molecule going over the top of substrate atoms; or by running along the trough between two rows of atoms. Going over the top of the atoms gives the appearance of shorter and wider molecules, as seen from simulated DFT images (Fig 6.11 b and c). Going over the trough between rows of atoms gives the longer and narrower appearance to the molecules (see figure 6.11d and e). In total, nine configurations were calculated by DFT, which converged to four orientations of local minima. The two other possible configurations were 1 eV higher in total energy (see the plot in figure 6.11f).

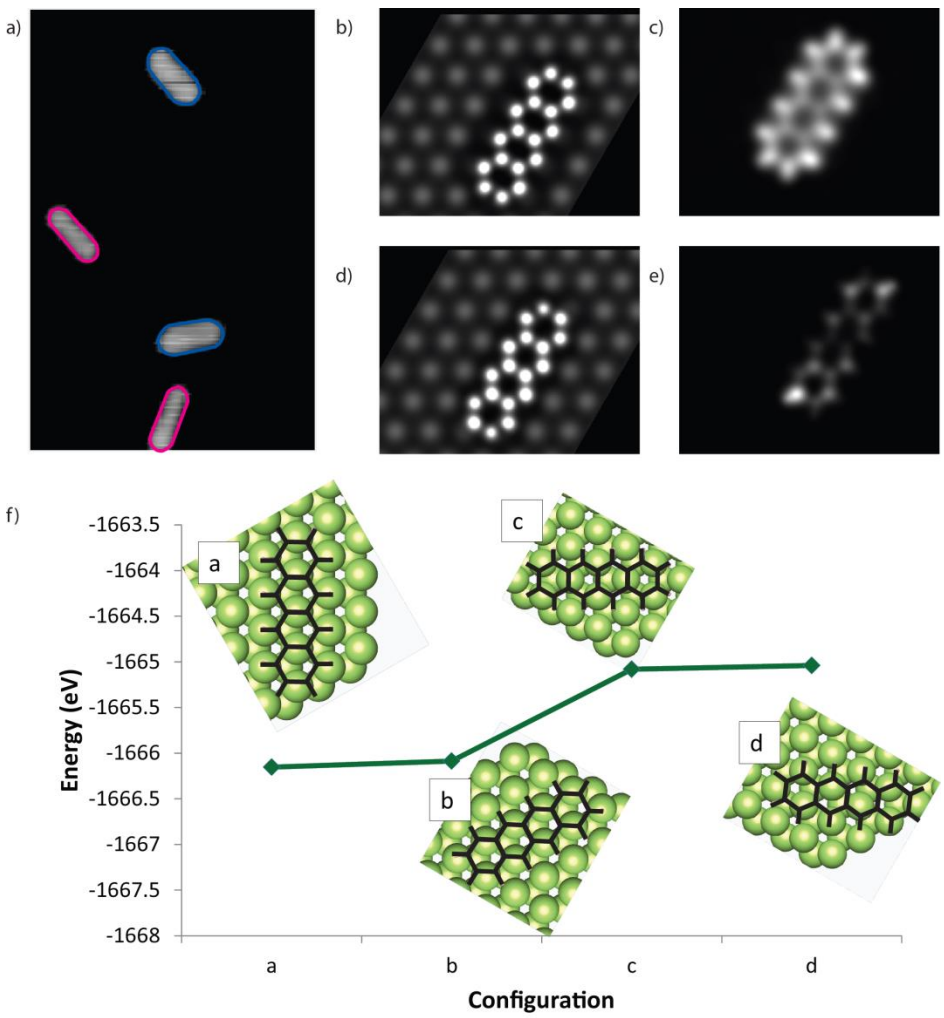

Figure 6.11

(a) shows an STM image with tetracene molecules adsorbed in two different sites which gives a different appearance to them. (b) and (c) are simulated STM images of tetracene adsorbed along a row of rhodium atoms and (d) and (e) are simulated STM images of tetracene adsorbed in the trough between two rows of rhodium atoms. (f) is an energy plot showing the total energy for tetracene adsorbed in the four local minima as calculated by DFT.

Figure 6.12 shows the first change which is observed for the tetracene, occurring at 570 K. This change is just slight, with evidence of some tetracene molecules aligning lengthways and others starting to couple together. The coupling together appears to be the attachment of two tetracene molecules end-to-end. The alignment lengthways does not seem to lead to any coupling with adjacent molecules but is a consequence of the increased thermal diffusivity of the molecules with the attractive molecule-molecule interaction.

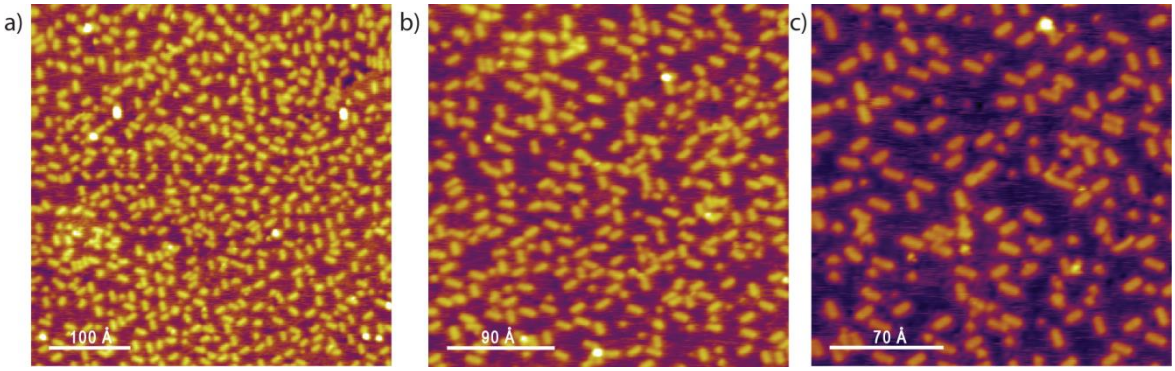

Figure 6.12

STM images of tetracene on Rh(111) after annealing to 570 K. Images were acquired with a current of 0.1 nA and a voltage of 1.08 V.

Whereas benzene, which can be viewed as a 1D-PAH of one unit, decomposes through reverse cyclotrimerisation, tetracene does not. Hence, fragmentation is dependent on the length of the chain, with the critical point lying somewhere between benzene and tetracene (likely naphthalene or anthracene). Since decomposition does not occur, then in this instance the coupling mechanism must be different. Indeed recent STM images, acquired in constant height mode, which allows for higher resolution (for the reasons discussed in section 5.3.6), reveal a different coupling mechanism. These images, shown in figure 6.13, indicate that the coupling occurs to give chains composed of discrete numbers of tetracene molecules, adjoined by what appears to be a C_4 bridge. This would mean that the tetracene molecules polymerise without the addition of C atoms, and without affecting the carbon backbone. Most likely, dehydrogenation would occur at the end of the molecule, which would allow the formation of new C-C bonds between the molecules creating a C_4 ring.

Figure 6.14, shows the first major change which is observed at 620 K, where there is no longer any sign of the tetracene. After this anneal, a drastic change has occurred and there is the presence of round protrusions, with a width of ~13 Å and a height of ~2 Å that can be assigned to $7C_6$ clusters. Alongside these clusters are several chains with a thicker appearance than the tetracene, and reminiscent of the kinked 1D-PAHs seen for ethene and benzene at 530 K. Compared to the ethene and benzene, however, this is very sudden and seems to miss the stage where only kinked 1D-PAHs are present on the

surface. One might expect that tetracene would convert to chrysene (the "kinked" form of tetracene) as it should be more stable due to a greater number of sextets (which is discussed in more detail in section 5.3.5). It is possible that this stage is missed due to an error on the reading from the thermocouple. As mentioned in section 3.2.1, an error of ±50 K exists which could result in the sample being heated to a higher temperature than intended and hence missing the stage where only kinked 1D-PAHs are present. It could be, however, that the mechanism is slightly different for the tetracene. The tetracene is effectively a 1D-PAH already, and it is more stable on the surface compared to the ethene and benzene, with no signs of decomposition to C_2 species. The coupling of just two tetracene molecules via, what is likely, a C_4 ring occurs at a relatively high temperature. With a little more energy, the coupled tetracene molecules could begin to kink and curl up before further polymerisation occurs. With shorter chains there is a higher probability in kinking resulting in curling up of the chain ends, so the curling up would occur at a faster rate. Figure 6.15 shows a tentative mechanism for two linked tetracene molecules to form $7C_6$. This mechanism has yet to be probed by DFT in a similar manner as was done by GTech, for ethene in section 5.3.6. The mechanism involves a carbon skeleton rearrangement which moves the 4-membered ring, giving five rings on one side. It is these five rings that form the majority of the cluster, along with two carbons from the other three rings, leaving a C_{12} fragment. This fragment could then attach to another fragment or tetracene molecule and form a further cluster. With further annealing more clusters are formed before the formation of graphene islands.

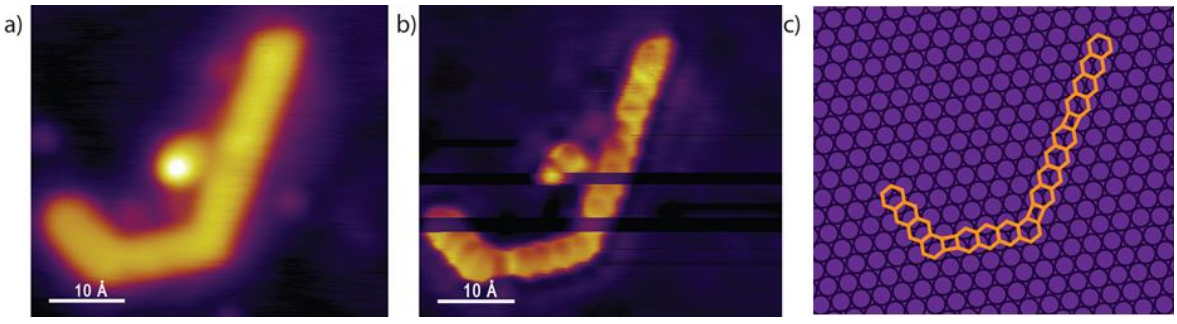

Figure 6.13

Shows STM images of linked tetracene molecules with (a) taken in constant current mode and (b) taken in constant height mode. The constant height image shows evidence of linking through C_4 rings which can be seen more clearly in the model in (c).

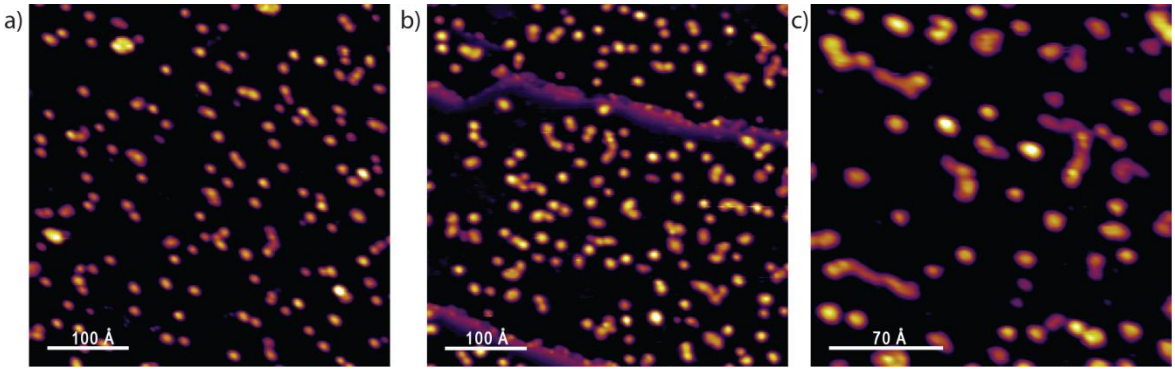

Figure 6.14

STM images of tetracene on Rh(111) after annealing to 620 K. Images were acquired with a current of 0.1 nA and a voltage of 1.08 V for (a) and (b), and a voltage of 0.72 for (c).

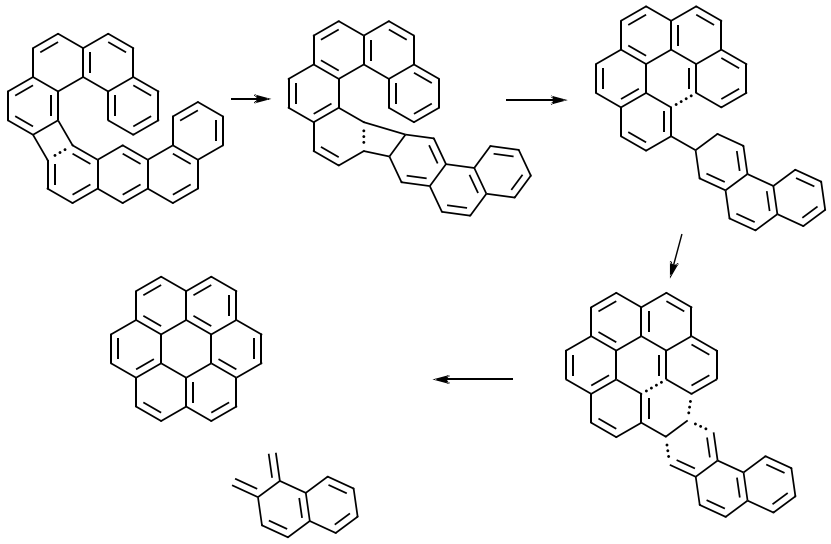

Figure 6.15

A tentative mechanism of how two linked tetracene molecules could curl-up and rearrange to form a $7C_6$ cluster.

Like the benzene, the tetracene follows a similar pathway to graphene as ethene does. Since the tetracene is effectively a short 1D-PAH it starts part way through the pathway. The tetracene couples (mindful of the C4 units within the chains) with another tetracene molecule before kinking and curling up to form $7C_6$. The $7C_6$ clusters then coalesce to form graphene.

6.3.3 Perylene

Figure 6.16 shows perylene after deposition at 180 K on Rh(111). Once deposited on the surface the perylene molecules appear as rectangular protrusions, similar to that seen previously on other surfaces.[14] [23] The molecules have a height of 1 Å with a width of 9 Å (fwhm) and a length of 11 Å (fwhm). Figure 6.2 shows a profile plot of the perylene alongside a variety of other species. Similar to benzene and tetracene, no ordering of the perylene molecules is observed at RT due to low mobility.

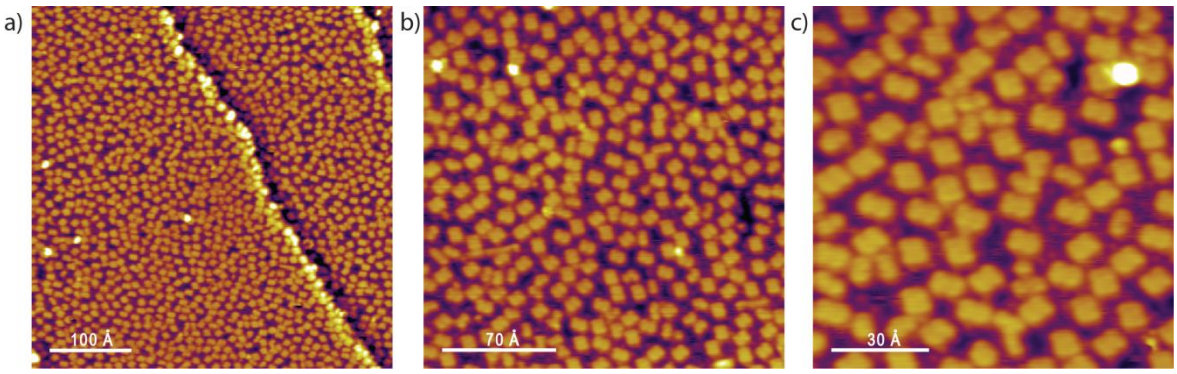

Figure 6.16

STM images of perylene on Rh(111) after deposition. Images were acquired with a current of 0.1 nA and a voltage of 0.65 V for (a) and 1.02 V for (b) and (c).

The perylene molecules are aligned along the high symmetry directions of the rhodium surface, indicating a strong interaction with the surface. The perylene molecules undergo no morphological change on the surface, up to a temperature of 470 K. Not all the molecules appear on the surface intact with signs of fragmentation, but these fragments do not increase in density with heating. This shows that the molecules are quite stable.

Benzene and tetracene are species similar to that seen in the pathway from ethene to graphene, but perylene is not. Perylene has a thicker structure than the 1D-PAHs and is just a few carbon atoms short of coronene or $7C_6$ (20 compared to 24 atoms). The weakest bonds in perylene are the ones on the central ring, which is less aromatic than the rest of the molecule.[24] So if it were to decompose, this would be the most likely position, giving two naphthalene-like species. However, decomposition does not happen, but the formation of chains occurs. At 520 K some of the perylene molecules start to align in chains, as shown in figure 6.17. The chains do not appear to be aligned end-to-end but rather they are angled or in a zig-zag type formation. It is expected that chains start to

form at this temperature due to partial dehydrogenation of the molecules, as well as an increased mobility on the surface.

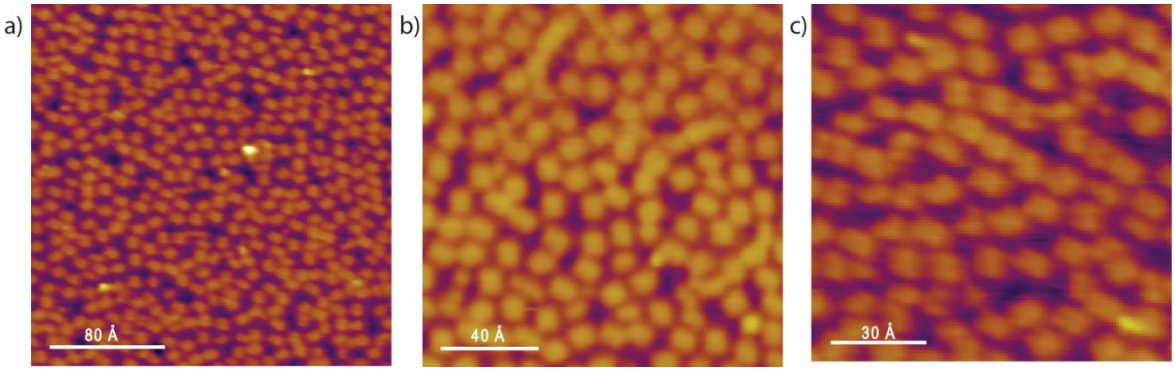

Figure 6.17

STM images of perylene on Rh(111) after annealing to 520 K. Images were acquired with a current of 0.1 nA and a voltage 0.20 V for (a) and 1.06 V for (b) and (c).

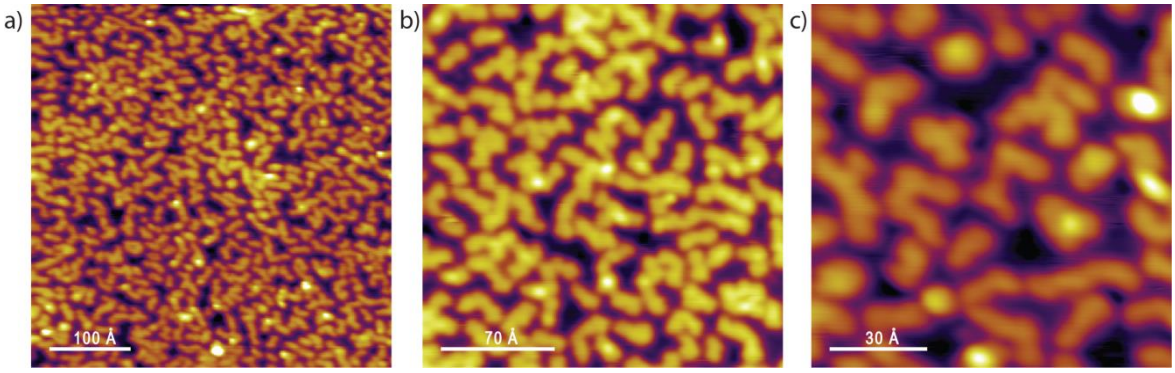

Figure 6.18

STM images of perylene on Rh(111) after annealing to 570 K. Images were acquired with a current of 0.1 nA and a voltage of 1.08 V for (a) and (b), and a voltage of 0.28 for (c).

By 570 K the surface is covered in chains (see figure 6.18). The mechanism by which this occurs is unclear, but the chains are indistinguishable from the chains produced from other feedstocks at this temperature. And like the other chains, these go on to curl-up and produce $7C_6$ at temperatures in the region of 670 K (see figure 6.19).

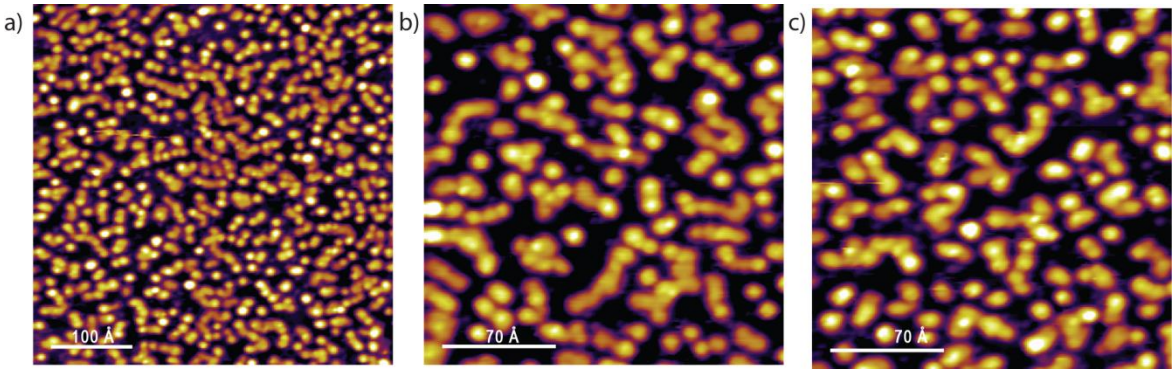

Figure 6.19

STM images of perylene on Rh(111) after annealing to 670 K. Images were acquired with a current of 0.1 nA and a voltage of 1.13 V.

6.4 Discussion

All the species studied follow the same route to graphene, with larger hydrocarbons joining further down the ethene pathway. A scheme showing the complete pathway, with the point at which the different hydrocarbons join is shown in figure 6.20. The scheme shows that the 1D-PAHs are important intermediates in the formation of $7C_6$ clusters, which are, in-turn, key to the formation of graphene. For ethene, the mechanism begins with coupling and cyclotrimerisation to form C_4 and C_6 species. This occurs at 370 K. Just above this temperature, at 420 K, benzene undergoes reverse cyclotrimerisation to C_2 and C_4 species, followed by cyclotrimerisation back to a benzene type species. This gives a surface morphology comparable to the ethene at this temperature.

The next step in the pathway occurs around 470 K, with both the ethene and benzene forming 1D-PAHs. The benzene-type species acts as the chain seed, and the C_4 molecules couple to this successively, to form the chain. At this stage, tetracene joins the pathway. Tetracene is effectively a short 1D-PAH that unlike benzene does not undergo decomposition. The tetracene is very stable on the surface, and with the absence of smaller species such as C_4 the chains can only grow with the coupling of tetracene molecules. The coupling appears to proceed via direct C-C bond formation between the carbon atoms at the end of the molecules, resulting in the formation of a C_4 ring. This coupling occurs at 570 K, which is the same temperature that the 1D-PAHs start to kink and bend.

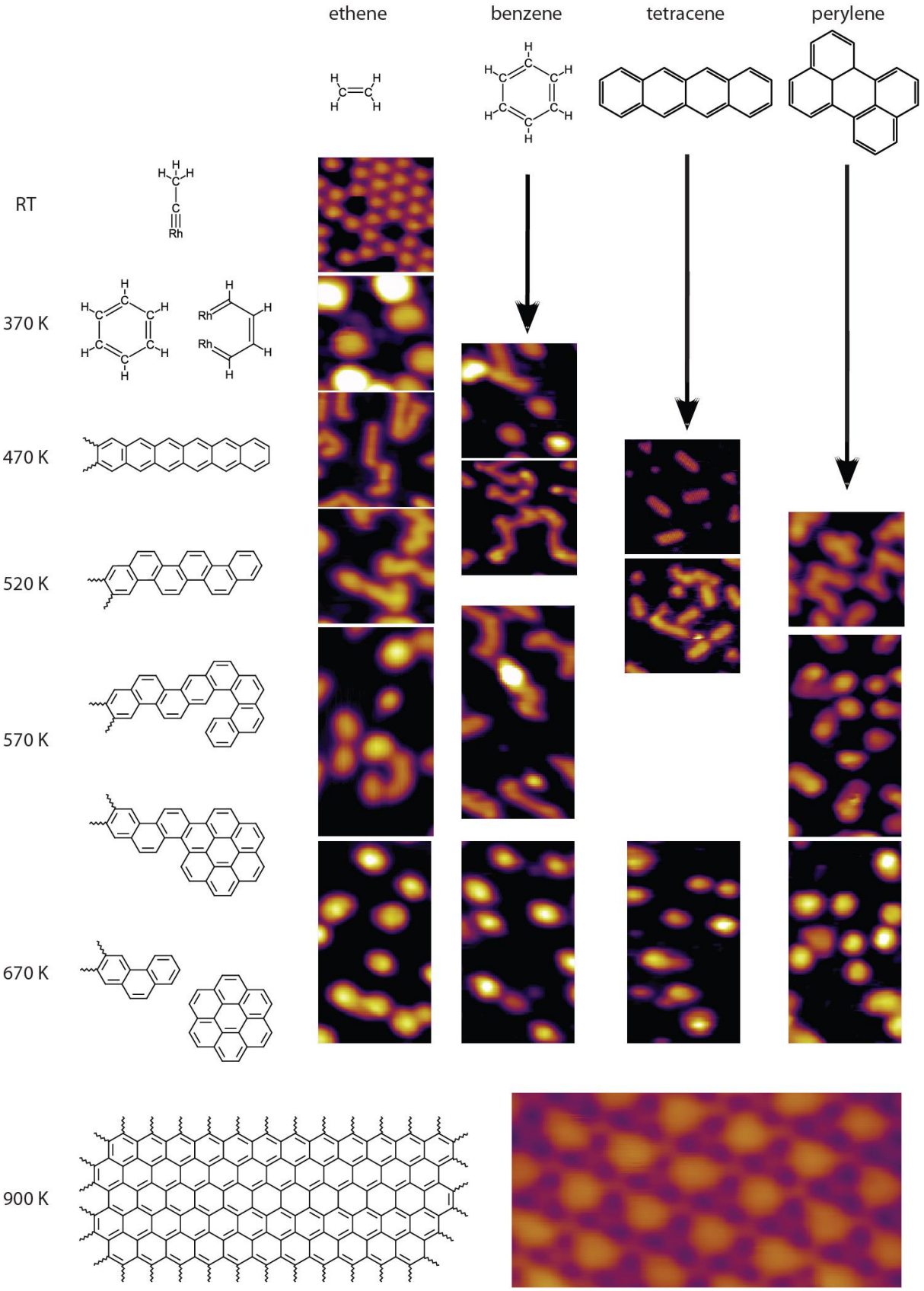

Figure 6.20 The complete pathway to graphene from the different feedstocks studied.

The kinking and the bending results in a coronene-like termination at the chain end. Due to the short length of the coupled tetracenes, this happens quickly, compared to the longer chains produced through the benzene and C_4 addition reaction. This coronene-like termination breaks off, either before or after dehydrogenation, to give $7C_6$ clusters. With enough energy these clusters can then coalesce to form graphene, with extended flakes observed by 900 K.

The perylene is not very similar to the intermediates seen in the ethene pathway to graphene. It is thicker than the 1D-PAHs and just a few carbon atoms short of coronene and the $7C_6$ clusters. It does, however, still produce chains and $7C_6$ clusters, demonstrating the importance of these intermediates in the pathway.

One issue that has not been raised so far is that of coverage dependence. Different coverages of the feedstocks have not been examined, and the coverage used has not been consistent across the feedstocks. It is unlikely that coverage would affect the mechanism of the pathway but reaction rate could be altered. It is expected that initially higher coverages will increase the reaction rate due to the close proximity of molecules for coupling. However, the rate may be decreased for higher coverages at the higher temperatures, due to steric hindrance limiting the ability of the chains to curl-up.

It is difficult to compare coverages across different hydrocarbons. This is because full coverage of a larger molecule would result in a higher number of carbon atoms on the surface, than for full coverage of smaller molecules. This is due to the requirement of a greater number of smaller molecules to fill the same area, and hence more space between them. For ethene, benzene, and tetracene, the surface was covered with between 500 and 600 carbon atoms per 100 Å × 100 Å area but this resulted in different coverages. The ethene had a coverage of ~85% of a monolayer, whereas the benzene had a coverage of ~55% of a monolayer, and tetracene ~25%. There was a higher number of C atoms deposited via perylene (~1150 atoms per 100 Å × 100 Å area) due to the difficulty in controlling the dosing pressure of sublimed molecules.

6.5 Conclusion

In conclusion, the route to graphene is the same for a variety of hydrocarbons with feedstocks with equivalent morphologies to the intermediates, destabilising at the same temperatures. The 1D-PAHs are found to be important in the formation of the $7C_6$ clusters, with these, in-turn crucial in the formation of graphene.

It is well documented that graphene can also be produced from feedstocks with other chemical elements present, such as pyridine or alcohols. Recently, Michael-John Treanor (within our group at the University of St. Andrews) has been studying the pathway of pyridine to graphene. STM images showing some of the different stages are shown in figure 6.21. The early stages of growth proceed differently to the ethene pathway (which is yet to be understood) but again at the later stages it reverts back. After room temperature deposition the pyridine appears on the surface intact as round protrusions of identical size. After annealing to 420 K the surface is covered solely in identical short chains with a bone-shaped appearance, which have yet to be identified. At 520 K the kinked chains present in the ethene pathway are observed, which then go on to form $7C_6$ clusters and eventually graphene. This return to the ethene pathway likely occurs after the loss of nitrogen from the surface. With the return to the ethene pathway even for feedstocks such a pyridine, the role of $7C_6$ as a generic bottleneck in the formation of graphene is further confirmed.

All the hydrocarbons studied, comprise of fewer than the 24 carbon atoms present in $7C_6$. It would be interesting to see the effect of using a feedstock similar to $7C_6$, such as coronene which is hydrogenated $7C_6$. This could simply dehydrogenate to $7C_6$, given enough thermal energy but it is also possible that the coronene could decompose. It could be that the creation of chains, through decomposition, is vital in the formation of $7C_6$ clusters. And what about precursors such as hexabenzocoronene, which are larger than the $7C_6$ clusters? Can these coalesce to form graphene? Or would they be so rigid that decomposition is necessary to produce the smaller $7C_6$ which is suitably mobile to coalesce to graphene?

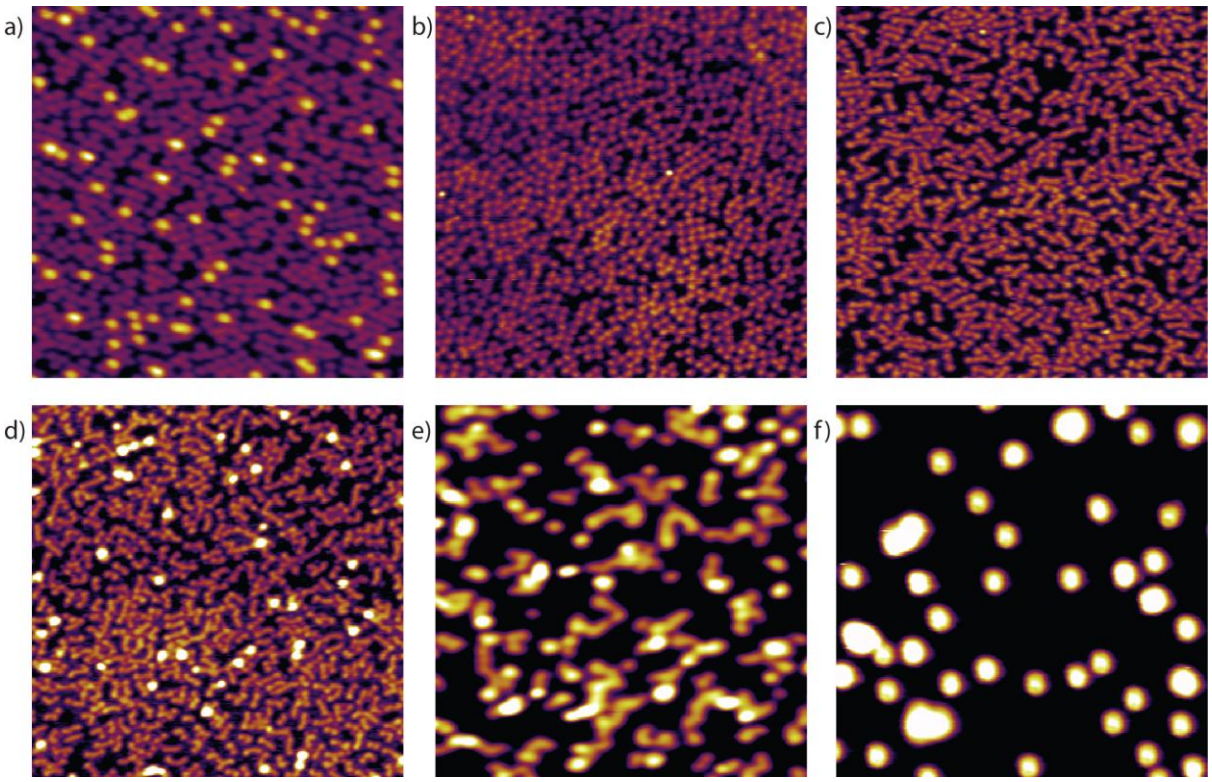

Figure 6.21

STM images of the species present on the Rh(111) surface after pyridine deposition and subsequent flash-annealing. (a) Pyridine after RT deposition. The following images were after flash-annealing to: (b) 370 K; (c) 420 K; (d) 520 K; (e) 570 K; and (f) 770 K. All the images have the same topographic contrast and a size of 220 Å × 220 Å. The images were acquired with a voltage of 0.1-1.1 V and a current of 0.1 nA.

Another feedstock that would be interesting is one with an odd number of carbon atoms, such as cyclopentadiene. It is likely that this would break down into a C_2 and C_3 unit. The C_3 could then couple with another C_3 molecule to produce the benzene-type species that could then continue along the usual pathway. However, it is also possible that a different pathway is taken with the first step being another reaction, such as a ring opening or a dimerization.

The relevance of this pathway is definitely significant but, as discussed above, further experiments will be required to discover the full extent. It is, however, a good starting point and provides novel information on the reaction kinetics of hydrocarbons on a metal surface, and of the mechanism by which graphene is formed.

References

[1] G. Ruan, Z. Sun, Z. Peng and J. M. Tour, *ACS Nano* **2011**, *5*, 7601-7607.
[2] A. Facchetti, *Chemistry of Materials* **2011**, *23*, 733-758.
[3] Q. Meng, H. Dong, W. Hu and D. Zhu, *Journal of Materials Chemistry* **2011**, *21*, 11708-11721.
[4] B. E. Koel, J. E. Crowell, C. M. Mate and G. A. Somorjai, *The Journal of Physical Chemistry* **1984**, *88*, 1988-1996.
[5] K. M. Bratlie, M. O. Montano, L. D. Flores, M. Paajanen and G. A. Somorjai, *Journal of the American Chemical Society* **2006**, *128*, 12810-12816.
[6] Y. G. Kim, J. E. Soto, X. L. Chen, Y. S. Park and M. P. Soriaga, *Journal of Electroanalytical Chemistry* **2003**, *554*, 167-174.
[7] M. Neuber, F. Schneider, C. Zubragel and M. Neumann, *Journal of Physical Chemistry* **1995**, *99*, 9160-9168.
[8] B. E. Koel, J. E. Crowell, B. E. Bent, C. M. Mate and G. A. Somorjai, *The Journal of Physical Chemistry* **1986**, *90*, 2949-2956.
[9] W. Gao, W. T. Zheng and Q. Jiang, *Journal of Chemical Physics* **2008**, *129,* 164705.
[10] Q. Chen, A. J. McDowall and N. V. Richardson, *Langmuir* **2003**, *19*, 10164-10171.
[11] H. Huang, F. Song, B. Lu, H. J. Zhang, W. D. Dou, H. Y. Li, P. M. He, S. N. Bao, Q. Chen and W. Z. Zhou, *Journal of Physics-Condensed Matter* **2008**, 20, 315010.
[12] S. Soubatch, I. Kroeger, C. Kumpf and F. S. Tautz, *Physical Review B* **2011**, *84,* 195440.
[13] H. Huang, F. Song, H. J. Zhang, W. D. Dou, H. Y. Li, P. M. He, S. N. Bao, Q. Chen and W. Z. Zhou, *Journal of Physics-Condensed Matter* **2007**, *19,* 296202.
[14] Q. Chen, A. J. McDowall and N. V. Richardson, *Chemistry of Materials* **2003**, *15*, 4113-4117.
[15] H. Y. Mao, H. Huang, Q. Chen, N. V. Richardson, Y. Wu, J. H. Zhang, H. Y. Li, P. M. He and S. N. Bao, *Journal of Chemical Physics* **2004**, *121*, 6972-6977.
[16] D. Wang, L. J. Wan, Q. M. Xu, C. Wang and C. L. Bai, *Surface Science* **2001**, *478*, L320-L326.
[17] Q. Chen, T. Rada, A. McDowall and N. V. Richardson, *Chemistry of Materials* **2002**, *14*, 743-749.
[18] R. F. Lin, G. S. Blackman, M. A. Van Hove and G. A. Somorjai, *Acta Crystallographica Section B* **1987**, *43*, 368-376.
[19] R. F. Lin, R. J. Koestner, M. A. Van Hove and G. A. Somorjai, *Surface Science* **1983**, *134*, 161-183.
[20] B. Wang, X. Ma, M. Caffio, R. Schaub and W.-X. Li, *Nano Letters* **2011**, *11*, 424-430.
[21] Y. Cui, Q. Fu, H. Zhang and X. Bao, *Chemical Communications* **2011**, *47*, 1470-1472.
[22] B. Wang, M. Caffio, C. Bromley, H. Früchtl and R. Schaub, *ACS Nano* **2010**, *4*, 5773-5782.
[23] K. Manandhar and B. A. Parkinson, *Journal of Physical Chemistry C* **2010**, *114*, 15394-15402.
[24] A. Ranganathan and G. U. Kulkarni, *Proceedings of the Indian Academy of Sciences-Chemical Sciences* **2003**, *115*, 637-647.

Chapter 7: Conclusion

One of the most promising methods for mass production of graphene with flakes of macroscopic lateral dimensions is the CVD growth on a transition metal surface. In this thesis the relationship between graphene and the transition metal support has been investigated, and the growth mechanism determined. This was done predominantly through the use of STM, with contributional support from HREELS, LEED, and DFT. These techniques proved effective in revealing the structural characteristics of graphene and its growth intermediates.

In Chapter 4, graphene was investigated on copper which is one of the most important metal substrates used for growth. Its importance stems from its low cost, relative to other metals substrates, and its low carbon solubility. Due to the well-known weak relationship between graphene and copper, growth in a UHV environment was found to be difficult. The use of thermal cycles in the presence of ethene enabled the production of large, high quality graphene flakes. Despite the weak relationship between graphene and copper foil, two preferred orientations were discovered using LEED. It was revealed that the predominantly (100) oriented copper foil was restructured to (n10) facets after the growth of graphene. Structural feedback was found to exist, with the graphene growth inducing and stabilising faceting of the copper surface, and the facets in-turn playing an important role in the graphene growth mechanism. The preferred orientations are most likely determined during nucleation and early stage growth, where it is expected that the interaction is stronger. Studies on the Cu(110) model system provided the most compelling evidence, and reason, for the existence of the two preferred orientations. LEED on this system revealed a rotation of ±5° of the graphene on the Cu(110), and the presence of coincident LEED peaks. The LEED peaks from one of the graphene orientations overlapped with the $(1\bar{1})$ and the $(\bar{1}1)$ peaks of the copper and the LEED peaks from the other graphene orientation overlapped with the (11) and $(\bar{1}\bar{1})$ peaks. This demonstrated a common surface periodicity between the copper and graphene and is an example of mismatch epitaxy. Despite the difference in symmetry between graphene (hexagonal) and the Cu(110) (rectangular), the orientation of the graphene is defined by

that of the Cu(110) substrate. This example of graphene growth on a single crystal substrate demonstrates how no-trivial graphene orientations can be favoured on low-symmetry surfaces, and reveals the importance of mismatch epitaxy for graphene growth on copper foil.

STM revealed a number of moiré patterns that exist for graphene on the Cu(110). One of the more common moiré patterns observed was analysed and overlayed with model lattices and found to have the graphene rotated by 5°, which is one of the preferred orientations observed via LEED. The overlayed lattices revealed large regions of alignment and misalignment. This is due to the graphene and copper having a similar surface periodicity, as shown by the LEED. This gives large regions where the two lattices are coincident before they gradually drift out of alignment. It is expected that different strengths of interactions exist for these regions, resulting in a rippled effect. The small rotational misalignment that results in this moiré pattern probably exists due to the large size of these regions, which enable the graphene to be pinned in this orientation before the regions of weaker interaction are grown.

Chapter 5 focused on the growth mechanism for the formation of graphene from ethene. This was carried out on the Rh(111) surface but is expected to proceed similarly on other transition metals. The thermal evolution of ethene to graphene consists of two regimes. The first regime is the transformation from aliphatic to aromatic hydrocarbon intermediates, through the decomposition and condensation of ethene. This results in the formation of 1D-PAHs. The second regime is the transition from these 1D-PAHs, to the 2D graphene. Some-what counterintuitively, this occurs through a second decomposition process. The 1D-PAHs previously produced, break-down to form size-selective carbon clusters. These carbon clusters comprise of seven fused carbon rings, in the form of dehydrogenated coronene. It is these clusters which are the precursors to graphene condensation.

Chapter 6, expanded on this work by examining the effect of different hydrocarbon feedstocks. The feedstocks studied were benzene, tetracene and perylene. Benzene and tetracene are similar to some of the intermediates on the ethene to graphene pathway. They were found to destabilise at the same temperatures, as the intermediates with

equivalent morphology. From that point on they would proceed along the same pathway as ethene. Perylene is different to the intermediates seen in the ethene pathway, yet it still forms chains and clusters on the route to graphene. This validates the importance of chains in the formation of $7C_6$ clusters, with the clusters in-turn being crucial in the formation of graphene.

In summary, the epitaxial relationship between graphene and its metal support has been studied, and its growth mechanism determined. Based on what has been achieved so far there are several directions the work could go. Firstly, the full extent of the graphene growth mechanism could be explored using different metal substrates and hydrocarbon feedstocks. Further exploration would enable the full significance of the pathway discussed in this thesis to become apparent. In particular, feedstocks larger than the $7C_6$ clusters and ones with odd numbers of carbon atoms such as cyclopentadiene could be investigated. Previous work has shown larger clusters to be more stable than $7C_6$ on the surface[1] yet it is $7C_6$ that dominates the surface immediately before the formation of graphene. This has been shown to be due to the formation mechanism which involves the curling up of chains and subsequent breaking off of the $7C_6$ cluster. If this is in fact the case and $7C_6$ is just the kinetic product rather than the thermodynamic one, then maybe even more stable, larger dehydrogenated clusters will be formed. It is perhaps possible that dehydrogenation cannot occur without the decomposition of the feedstock. They could also be too strongly bound to the surface to coalesce to form graphene and decomposition is necessary to produce the smaller $7C_6$, which is suitably mobile at the growth temperatures to coalesce to form graphene.

Using a feedstock such as cyclopentadiene would be interesting as, unlike the precursors studied in this thesis, it has an odd number of carbon atoms. It is likely that this would break down into a C2 and C3 unit. The C3 could then couple with another C3 molecule to produce the benzene-type species that could then continue along the usual pathway. However, it is also possible that a different pathway is taken with the first step being another reaction, such as a ring opening or a dimerization.

A second direction in which the research could develop is to use the knowledge of the pathway to produce functionalised graphene by using doped intermediates. For example,

if $7C_6$ clusters could be synthesised which have been predoped, then perhaps these could be used to produce doped graphene with the dopants uniformly dispersed. However, due to the weakness of the C-N bond, compared to a C-C bond, decomposition could occur and possibly even the loss of nitrogen from the surface.

A third direction that the research could proceed in is by exploring the pathway for other graphene like materials such as sheets of hexagonal boron nitride (h-BN). Despite the similar structure to graphene, h-BN is a dielectric with a wide band gap.[2] It is, however, a material of great interest and can be grown like graphene using CVD, with the feedstock being borazine. Borazine is isostructural with benzene but it is more reactive due to the electronegativity of boron (~2) compared to nitrogen (~3). It is known that when heating liquid borazine in a flask polyborazylene is produced.[3] Polyborazylene is a polymer of borazine, which has undergone partial dehydrogenation and polymerised through coupling in a para-fashion by the formation of N-B bonds. If a similar polymerisation occurred on a surface, it could be imagined that the h-BN sheet could be formed through cross-linking of these chains. The formation could, however, proceed through any number of possible pathways (including a similar one to that of graphene) that could only be determined through investigation.

References

[1] B. Wang, X. Ma, M. Caffio, R. Schaub and W.-X. Li, *Nano Letters* **2011**, *11*, 424-430.
[2] Z. Liu, L. Ma, G. Shi, W. Zhou, Y. Gong, S. Lei, X. Yang, J. Zhang, J. Yu, K. P. Hackenberg, A. Babakhani, J.-C. Idrobo, R. Vajtai, J. Lou and P. M. Ajayan, *Nature Nanotechnology* **2013**, *8*, 119-124.
[3] P. J. Fazen, J. S. Beck, A. T. Lynch, E. E. Remsen and L. G. Sneddon, *Chemistry of Materials* **1990**, *2*, 96-97.

List of publications

Directly related to current thesis

1. Weak mismatch epitaxy and structural feedback in graphene growth on copper foil

   N. Wilson, A. Marsden, M. Saghir, C. Bromley, R. Schaub, G. Costantini, T. White, C. Partridge, A. Barinov, P. Dudin, A. Sanchez, J. Mudd, M. Walker, and G. Bell, *Nano Research* **2013**, *6*, 99-112.

2. Ethene to graphene: surface catalysed chemical pathways, intermediates, and assembly

   Bo Wang,* Michael König,* Catherine J. Bromley,* Bokwon Yoon, Marco Caffio, Federico Grillo, Neville V. Richardson, Friedrich Esch, Ulrich Heiz, Uzi Landman, and Renald Schaub. Submitted to Science.

   *Authors contributed equally

3. A generic surface catalysed chemical pathway to graphene from different feedstocks

   Catherine J. Bromley, Michael-John Treanor, Michael König, Federico Grillo, Neville V. Richardson, Friedrich Esch, Ulrich Heiz, and Renald Schaub. In preparation.

4. Probing for weak intermolecular van der Waals interactions in the case of benzene on Rh(111) by STM

   Catherine J. Bromley, Michael-John Treanor, José A. Garrido Torres, Herbert Früchtl, and Renald Schaub. In preparation.

5. A combined STM and DFT study on the relationship between aromatic hydrocarbon length and surface–assisted decomposition and condensation reactions: the case of benzene, naphthalene, anthracene, and tetracene on a Rh(111) surface

   Michael-John Treanor, Catherine J. Bromley, José A. Garrido Torres, Herbert Früchtl, and Renald Schaub. In preparation.

Other publications

1. The preparation and X-ray structure of heptasulfurimidostearate

   C. J. Bromley, A. M. Z. Slawin, P. G. Waddell and J. D. Woollins, *Inorganic Chemistry Communications* **2009**, *12*, 804-805.

2. Coupling epitaxy, chemical bonding, and work function at the local scale in transition metal-supported graphene

   B. Wang, M. Caffio, C. Bromley, H. Fruchtl and R. Schaub, *ACS Nano* **2010**, *4*, 5773-5782.